NEUTRON SCATTERING STUDIES OF $\mathrm{Yb_2Ti_2O_7}$

NEUTRON SCATTERING STUDIES OF THE QUANTUM SPIN ICE MATERIAL $\mathrm{YB_2TI_2O_7}$

By

KATHRYN AILEEN ROSS, B.SC.

A Thesis

Submitted to the School of Graduate Studies

in Partial Fulfilment of the Requirements

for the Degree

Doctor of Philosophy of Science

McMaster University

Doctor of Philosophy of Science (2012) McMaster University
(Department of Physics and Astronomy) Hamilton, Ontario

TITLE: Neutron Scattering Studies of the Quantum Spin Ice Material $Yb_2Ti_2O_7$

AUTHOR: Kathryn Ross, B.Sc.

SUPERVISOR: Bruce D. Gaulin

NUMBER OF PAGES: xxvii, 178

Abstract

$Yb_2Ti_2O_7$ is one member of a series of magnetic compounds with the pyrochlore lattice structure. For specific types of single-ion anisotropy and exchange interactions, the geometry of the pyrochlore lattice frustrates near-neighbor interactions and coaxes a wide variety of unusual magnetic ground states from such compounds. $Yb_2Ti_2O_7$ is unique among these compounds in that the source of the frustration is not immediately obvious when one considers the combination of single-ion anisotropy (XY-like) and the nature of the exchange interactions (ferromagnetic) present therein. A conventional magnetic transition was indeed initially expected based on the observation of specific heat anomaly near 200mK. However, many studies produced no signs of long-range magnetic order below this temperature. Intriguingly, above the transition, evidence for unusual two-dimensional correlations came in the form of rods of magnetic diffuse neutron scattering. This thesis contains four articles that detail the results of several neutron scattering studies on $Yb_2Ti_2O_7$. The goal of these studies was to determine the nature of the static and dynamic spin correlations throughout the magnetic field vs. temperature phase diagram of $Yb_2Ti_2O_7$.

We first performed a time-of-flight neutron scattering experiment on a single crystal of $Yb_2Ti_2O_7$, which we prepared using the optical floating zone method. This initial study provided a comprehensive survey of the phase diagram, including the previously unexplored response to a magnetic field. We found that the rods of diffuse scattering change qualitatively upon cooling below the temperature of the reported specific heat anomaly, showing signs for

the development of short-range three-dimensional correlations. Additionally, we discovered that a relatively small magnetic field applied along the [110] direction could remove the diffuse scattering entirely, and produce sharp spin wave excitations in the inelastic channel, indicating long range spin correlations.

We further quantified the temperature dependence of the diffuse scattering in zero-field using a triple-axis neutron spectrometer. The crossover from two-dimensional correlations to short-range three-dimensional correlations was found to begin at 400mK and reach completion near the temperature of the specific heat anomaly, ∼200mK. Our measurements of the low temperature specific heat of several single crystal samples, as well as a powder sample, revealed that significant sample-dependence of the magnetic properties exists. The single crystal samples were shown to have broader features in the specific heat at relatively low temperatures compared to the powder samples, pointing to some amount of structural disorder in the single crystals.

To understand the nature of the structural defects in the single crystals, we compared the structure of a crushed single crystal of $Yb_2Ti_2O_7$ to that of a powder sample using neutron powder diffraction. The major conclusion of that work was that the single crystal is non-stoichiometric, containing 2.3% excess ytterbium on the (non-magnetic) titanium sublattice. The introduction of additional magnetic moments into the system is expected to be the cause of the sample-dependence of the specific heat anomaly.

Finally, we fit the spin wave dispersions in the field-polarized state, as measured by time-of-flight inelastic neutron scattering, to an effective spin-

1/2 anisotropic exchange Hamiltonian. The microscopic parameters extracted from these fits place $Yb_2Ti_2O_7$ close to exotic Quantum Spin Liquid phases predicted for the anisotropic spin-1/2 pryochlore model. The exchange parameters also reveal that the source of the frustration in $Yb_2Ti_2O_7$ comes from the "quantum spin ice" nature of its exchange interactions.

Acknowledgements

My experience over the past five years has been shaped, first and foremost, by the generous and kind supervision of Bruce Gaulin. Bruce has tirelessly provided me guidance on questions of technical, scientific, and professional nature. He possesses an impressive tact and professionalism, as well as deep physical intuition. I am lucky to have such a strong role model to try to emulate throughout my own career. I especially want to thank him for being a die-hard source of encouragement, and a friend, though various stages of my degree.

The growth of single crystals is both an art and a science, and in both ways it is daunting without a guiding light of experience. For me, this light has come in the form of expert supervision from Hanna Dabkowska and Antoni Dabkowski, and I thank them dearly for their time and efforts in our crystal growth projects. In the x-ray lab, the technical expertise of Marek Kiela has been essential. His role in us being able to do our work is invaluable. My lab-mates, in particular Katharina Fritsch, Pat Clancy and Jerod Wagman, have made every shared neutron scattering experiment more successful, every practiced presentation clearer, and every day in the lab a fruitful learning experience.

On a personal note, I truly feel that I found my place as part of a real community in the Department of Physics and Astronomy. With so many great friends and colleagues, no thoughts of any nature went unhashed, no cries were bereft of caring shoulders (thank you, Annie), no ecstatic high fives wiffled in lonliness, and very few exquisite patio days were missed. Dear friends, thank you for the infinite supply of great times.

Finally, the support of my family throughout my long education has made me a stronger person.

Co-Authorship

All of the projects discussed in this thesis are collaborative efforts.

The $Yb_2Ti_2O_7$ crystals used in the experiments described in this thesis were prepared by myself and Jacob Ruff, under the supervision of Hanna Dabkowska.

The experiments described in Chapter 2 greatly benefitted from the contributions of the people listed as co-authors on that article. I led the experiment and the crystal growth, with the assistance of Jacob Ruff, who was heavily involved in the preparation and execution of the experiment. We received great technical assistance from Yiming Qiu at the DCS instrument. I received assistance in performing the magnetization measurements from Gregory MacDougall and Paul Dube. I led the writing of the article in Chapter 2, which also had significant contributions from Jacob Ruff and Bruce Gaulin.

The neutron scattering data described in Chapter 3 were the result of beam time at the NIST Center for Neutron Research (NCNR), where the contributions of Jason Gardner and Deepak Singh as well as Julia Scherschligt (in the sample environment team) were important. However, a prior experiment was carried out at the Paul Scherrer Institut (PSI) by myself and Mark Laver, which served as important preliminary work that allowed us to proceed efficiently at the NCNR. The experiment at PSI was made possible by Mark Laver, both organizationally and technically. I wrote the article presented in Chapter 3, with significant input from Bruce Gaulin.

The specific heat data presented in Chapter 3 and Chapter 5 were collected by Jan Kycia's group at the University of Waterloo, with the largest contributors to the project being Jeff Quilliam and Luke Yaraskavitch.

Chapter 4 was the result of a collaboration with a theory group at UC Santa Barbara; Lucile Savary and Leon Balents. The theory group prepared the linear spin wave calculation and performed the theoretical analysis of the exchange parameters that were extracted based on neutron scattering data collected by Bruce Gaulin and myself. That inelastic neutron scattering data was obtained at the NCNR as part of the same experiment that yielded the results of Chapter 2. In addition to executing the experiment, I developed a method to fit the spin wave theory to the data, and wrote the portions of the article relating to the experimental work and fits.

I prepared and executed the neutron powder diffraction experient described in Chapter 5. Thomas Proffen guided me in the use of the NPDF instrument at Los Alamos National Laboratory. Thomas also provided me with significant expert advice in the analysis stages of the work. I wrote all sections of the article, with input from Bruce Gaulin and Hanna Dabkowska.

The additional writing in this thesis is my own, and has benefitted from the comments and corrections offered by Bruce Gaulin.

For my mother and father, who gave me the opportunity and the capacity for wonder

Table of Contents

List of Figures

List of Tables

Chapter 1

Introduction

> *The phenomenon of one set of degrees of freedom (like spins) giving rise to a qualitatively different set (like photons) is known as emergence. This ability of condensed matter systems to mimic spontaneously and collectively different ones - possibly unknown or otherwise unrealizable - is among their most fascinating properties.*
>
> – Moessner and Ramirez [1]

Over the course of this thesis project, our understanding of $Yb_2Ti_2O_7$ has grown from the observation of mysterious behaviour, to having in hand a remarkably accurate microscopic description of its magnetic properties. The detailed study of $Yb_2Ti_2O_7$ has revealed to us unexpected outcomes. One exciting result is the expectation that emergence is important in $Yb_2Ti_2O_7$, a realization that has come from the discovery of its unusual "quantum spin ice" nature. Almost simultaneous to this advancement of the microscopic model, we developed an appreciation for some of the non-idealities that exist in the real samples, which have caused confusion as to the true nature of the magnetic ground state up to this point.

In this chapter I will begin by introducing relevant concepts in solid state magnetism, which will allow the introduction of the anisotropic exchange Hamiltonian that has been so successful in describing $Yb_2Ti_2O_7$. I will then provide context for the study of $Yb_2Ti_2O_7$ by describing results on some of the closely related compounds, the rare-earth titanates. Then I will review the literature on $Yb_2Ti_2O_7$ that set the stage for the work in this thesis. Finally, I will introduce the basics of neutron scattering, which is the main measurement technique used in these studies, as well as optical floating zone crystal growth, which is the method by which our single crystals of $Yb_2Ti_2O_7$ were produced.

1.1 Magnetism in localized electronic systems

A large subfield of condensed matter research focuses on the magnetic properties of materials containing unpaired electrons. In particular, in ionic solids one may find that the valence state of the constituent ions is such that they have a non-zero magnetic moment. In the case of insulators such as $Yb_2Ti_2O_7$, these magnetic moments are localized and they form a magnetic sublattice within the crystal structure. In $Yb_2Ti_2O_7$, the only ions supporting a magnetic moment are Yb^{3+} and they take up the pyrochlore lattice, shown in Figure 1.2. The pyrochlore lattice consists of an array of corner-sharing tetrahedra. This geometry often leads to a phenomenon called *geometric frustration*, which tends to suppress the conventional magnetic behaviour that is described in Section 1.1.1.1, paving the way for a wide variety of exotic magnetic effects (Sections 1.1.1.2 and 1.2).

Magnetism of all types relies on the formation of a magnetic dipole moments, $\vec{\mu}$, which are either associated with the nucleus or with the electrons in an atom. Electronic moments arise from the angular momentum of ions with unpaired electrons. Both spin, $\vec{S}$, and orbital, $\vec{L}$, angular momenta combine to give the total angular momentum vector operator , $\vec{J} = \vec{S} + \vec{L}$. The total angular momentum, $\vec{G} = \hbar\vec{J}$, then has a magnitude given by,

$$G = \sqrt{J(J+1)}\hbar. \tag{1.1}$$

The quantum number J can take the values $J = (L-S), (L-S+1), \ldots (L+S)$. Hund's rules can be applied to a given ion to determine what value of J corresponds to the lowest energy multiplet (see Ref. 2 for example). In the absence of any mechanism to split the degeneracy, there are $2J+1$ degenerate states within that multiplet, corresponding to the possible M_J values. The magnetic moment induced by the angular momentum of the ion is proportional to the total angular momentum vector $\vec{G}$,

$$\vec{\mu} = -g_L \mu_B \vec{G}, \tag{1.2}$$

where $g_L = 1 + \frac{J(J+1)+S(S+1)-L(L+1)}{2J(J+1)}$ is the Landé g-factor, and $\mu_B = \hbar e/2mc$ is the Bohr magneton.

In the case of a free ion, the magnetic moment is then,

$$\mu = g_L \mu_B \sqrt{J(J+1)}. \tag{1.3}$$

For ions located within a crystal environment, the degeneracy of the J multiplet is split by the electric field generated by the other ions in the crystal. The magnetic moment associated with these ions then depends on the manner in which the multiplet is split. The resulting energy levels are called the crystal field levels. The crystal electric field also puts constraints on how the magnetic moment can be oriented with respect to the local point symmetry at the ionic position. This is described by a tensor form for the Landé g-factor (the "g-tensor"). These considerations are discussed in Section 1.1.2 for the specific case of the rare-earth pyrochlores.

The preceding discussion treats the magnetic moment as arising from both spin and orbital angular momentum. This is indeed the most general case. However, in the literature it is common to refer to the magnetic moments simply as "spins", and magnetic Hamiltonians generally refer to the moments in terms of vector spin operators $\vec{S}$. In magnetic materials with transition metal ions, contributions from the orbital momentum is often "quenched", i.e. rendered insignificant, by crystal electric field effects, leaving only the spin angular momentum in the problem. This does not occur in the rare-earth systems, so the operator $\vec{S}$ should be written as $\vec{J}$. However, in what follows this is not done, in order to avoid confusion between the total angular momentum operator $\vec{J}$ and the exchange energy, which is commonly called J. Furthermore, in Section 1.1.2, a case will be made for treating the angular momentum operators in $Yb_2Ti_2O_7$ as pseudo-spin 1/2 operators, which effectively absorbs the orbital effects into the exchange coupling constants.

1.1.1 Interacting magnetic systems

Cooperative behaviour can occur in magnetic sublattices when the interactions between the spins are not negligible. The angular momentum degrees of freedom at each site are influenced by each other through three main interactions:

1. **Exchange interactions:** These arise when the wavefunctions of neighboring ions overlap spatially. The statistics of identical fermions, such as electrons, requires that the overall wavefunction for a two-fermion state must be anti-symmetric when the particles are exchanged with one another. The wavefunction of a two-electron system, for example, is composed of both a spatial and spin part. The product of the two parts must be anti-symmetric with respect to exchange. Thus, depending on the details of the spatial parts of the overlapping wavefunctions, the spin part will be be required to be either symmetric or anti-symmetric. The former case is called ferromagnetic exchange, and the latter, anti-ferromagnetic exchange. In magnetic insulators, exchange interactions can occur because of direct overlap of magnetic wavefunctions (*direct* exchange), or it could be mediated by an intervening, non-magnetic ion, such as O^{2-} (*superexchange*). The exchange interaction can be written as,

   $$J \sum_{\langle i,j \rangle} \vec{S}_i \cdot \vec{S}_j, \tag{1.4}$$

   where J is called the exchange energy constant, which could be positive or negative, corresponding to anti-ferromagnetic or ferromagnetic interactions respectively. The sum in this term is written over all nearest neighbor pairs of ions. This specific form of the exchange interaction term treats each component of the spin operators equally, and is therefore isotropic.

2. **Dipolar interactions:** The magnetic dipole moments interact with each other through the magnetic fields they create. The energy for a magnetic moment $\vec{\mu}$ in a magnetic field is $E = -\vec{\mu} \cdot \vec{B}$, where $\vec{B}$ is the field created by a magnetic dipole,

$$\vec{B} = \frac{3(\vec{\mu} \cdot \hat{r})\hat{r} - \vec{\mu}}{r^3}. \tag{1.5}$$

   The dipolar interaction energy falls off as 1/r^3, implying that including dipolar interactions between only the nearest neighbors is often sufficient for modestly sized magnetic moments. However, this need not be the case for larger moments which can dramatically affect the magnetic ground state of the model (for example, in the classical dipolar spin ices [3]).

3. **Dzyaloshinskii Moriya interactions:** When the magnetic sublattice lacks an inversion center between neighboring ions, as in the case of the pyrochlore lattice, Dzyaloshinskii Moriya (DM) interactions are allowed by symmetry[4]. The DM interaction takes the form of a cross product of neighboring spins:

$$H_{DM} = \sum_{\langle i,j \rangle} \vec{D}_{i,j} \cdot (\vec{S}_i \times \vec{S}_j) \tag{1.6}$$

A simple Hamiltonian including all of the above interactions between nearest neighbors can be written as:

$$H = \sum_{\langle i,j \rangle} J(\vec{S}_i \cdot \vec{S}_j) + \frac{g^2 \mu_B^2}{r^3} \sum_{\langle i,j \rangle} [\vec{S}_i \cdot \vec{S}_j - 3(\vec{S}_i \cdot \hat{r})(\vec{S}_j \cdot \hat{r})] \\ + \sum_{\langle i,j \rangle} \vec{D}_{i,j} \cdot (\vec{S}_i \times \vec{S}_j) - g\mu_B \sum_i \vec{S}_i \cdot \vec{H} \tag{1.7}$$

where J is the (isotropic) exchange coupling, g is the scalar g-factor (which equals 2 for a spin-only single unpaired electron, but more generally is the Landé g-factor given with Eqn. 1.3), r is the distance between the sites i and j, $\hat{r}$ is the unit vector along the direction connecting sites i and j, $\vec{D}_{ij}$ is the Dzyaloshinskii Moriya vector, and $\vec{H}$ is the applied magnetic field. The last term is not an interaction between spins, but describes the effect of a magnetic field on the spins through Zeeman splitting of the angular momentum multiplets.

This Hamiltonian, or subsets of these terms, can be used as a first approximation for understanding magnetic states that arise from spin-spin interactions.

1.1.1.1 Paramagnetism vs. conventional magnetic order

In a material lacking any intersite interactions, the magnetic moments are free to be oriented randomly (to within the constraints imposed by the crystalline electric field, see Section 1.1.2). In all real materials, however, there are always some interactions between the moments. The free energy of the system at a particular temperature T is given by $F = U - TS$, where U is the thermodynamic internal energy, obtained from a probability-weighted average of all eigenvalues from a Hamiltonian such as Eqn. 1.4, and S is the entropy of the microcanonical ensemble. This equation has the usual implications that when the temperature is higher than the relevant energy scales in the system, entropy will dominate and the configuration will remain disordered, or *paramagnetic*.

When $k_B T$ is comparable, or smaller, to the interaction energy, one expects the system to form a state that minimizes the internal energy. In particular, for the simple case of isotropic exchange between spins on a bipartite lattice such as a square lattice, one expects the system to select a global configuration in which they are all parallel or anti-parallel, for J negative or positive, respectively. These two states are called a ferromagnet (FM) and an anti-ferromagnet (AFM), and are illustrated in Figure 1.1 a) and b) . Other, more complicated spin configurations can arise, such as the 120° state for classical AFM Heisenberg spins on a triangular lattice (Fig. 1.1 c). All of these examples are called long-range ordered (LRO) states because the local spin configuration is repeated “infinitely”, i.e. the correlation lengths are the size of the system itself.

Typically, ordered ground states will be reached as the system goes through a thermodynamic phase transition at a given temperature, T_c, which will be on the order of the interaction energy. The phase transition can be charac-

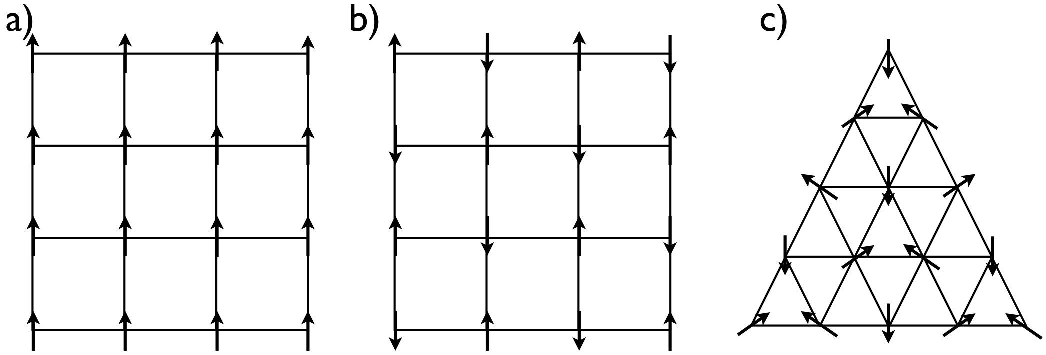

Figure 1.1: Three types of long-range order, illustrated on 2D lattices: a) ferromagnetic collinear order, b) anti-ferromagnetic collinear order, and c) anti-ferromagnetic 120° order on the triangular lattice.

terized as either first or second order. In a first order phase transition, the order parameter (for example, the bulk magnetization of a collinear ferromagnet) changes discontinuously at T_c, while in a second order phase transition, it is the first temperature derivative of the order parameter that changes discontinuously. Both types of transitions produce sharp peaks in the specific heat as a function of temperature. Thus, the presence of a sharp specific heat anomaly is a sign of a phase transition, and in magnetic systems, this usually corresponds to the development of long-range order.

Information on the type of interactions present in the system, and an estimate of the ordering temperature, can be obtained from studying the paramagnetic state. This is accomplished by using a mean-field treatment, which takes into account the internal field created by the magnetic moments as they begin to order. The Curie-Weiss law, which can be obtained from a mean-field treatment, predicts a linear dependence of the inverse magnetic susceptibility on temperature,

$$\frac{1}{\chi} = \frac{T}{C} - \frac{\theta_{CW}}{C}, \tag{1.8}$$

where $C = \frac{N}{3V}\frac{\mu^2}{k_B}$ with μ being the effective moment (Eqn 1.3), and the Curie-Weiss temperature, θ_{CW}, gives an estimate of the ordering temperature. If θ_{CW} is positive, this indicates overall ferromagnetic interactions, while a negative value indicates overall anti-ferromagnetic interactions. If both signs of interactions are present with different energy scales, one may see a non-linear behaviour of the inverse susceptibility. Anisotropies also give rise to non-linearity of the inverse susceptibility [5]. Both effects are present in $Yb_2Ti_2O_7$, but the application of the Curie-Weiss law can still be of use in comparing between different samples of $Yb_2Ti_2O_7$, as was done in Chapter 5.

1.1.1.2 Magnetic and geometric frustration

Occasionally, the interactions between moments in the lattice compete with one another, leading to what is known as “magnetic frustration”. For example, the J_1-J_2 model on the square lattice is frustrated for anti-ferromagnetic J_1 and J_2 (Figure 1.2 a). The relative strength of these two exchange interactions “tunes” the amount of frustration, in the sense that the individual ordered ground states preferred by J_1 and J_2 have energies that are closer or farther from each other depending on the ratio of J_2/J_1. If the two energies are identical, then the system will not be able to select one or the other by energetic means, and will remain disordered even as the temperature is lowered through an energy scale comparable to J_1 and J_2. Thus, for finely tuned problems (in this case, where $J_2/J_1 = 0.5$), one can possibly realize a disordered ground state at $T = 0$ [6].

The above discussion relates to frustration caused by competing interactions. The same concept can be applied in the case of a *single* interaction that is frustrated by the geometry of the lattice. This is called *geometric frustration.* The prototypical example is shown in Figure 1.2 b), a triangular plaquette with AFM interactions between Ising spins. The exchange energy cannot be minimized for all three pairs of spins simultaneously, which creates a degeneracy of the lowest energy configuration. Tiling these triangles to form a repeating lattice, for example in the triangular (edge-sharing) or the kagome (corner-sharing) lattice (Figure 1.2 c) and d)), extends the degeneracy. The degeneracy is said to be macroscopic, since the number of lowest energy configurations scales with the system size (this is also called "extensive" degeneracy). The same idea can be applied in three dimensions, using the tetrahedron as the basic unit with which to tile the lattice. They can be made edge sharing, resulting in a face-centered cubic lattice, or corner sharing, resulting in the pyrochlore lattice (Figure 1.2 e) and f)).

Since geometric frustration does not require any fine tuning, we expect many real materials with triangular or tetrahedral motifs to be geometrically frustrated. The lattices that have corner-sharing plaquettes (i.e. the kagome lattice in 2D or the pyrochlore lattice in 3D) have lower connectivities than their edge-sharing counterparts, allowing a greater degree of internal freedom for each plaquette and hence a more degenerate ground state [1]. Thus, to look

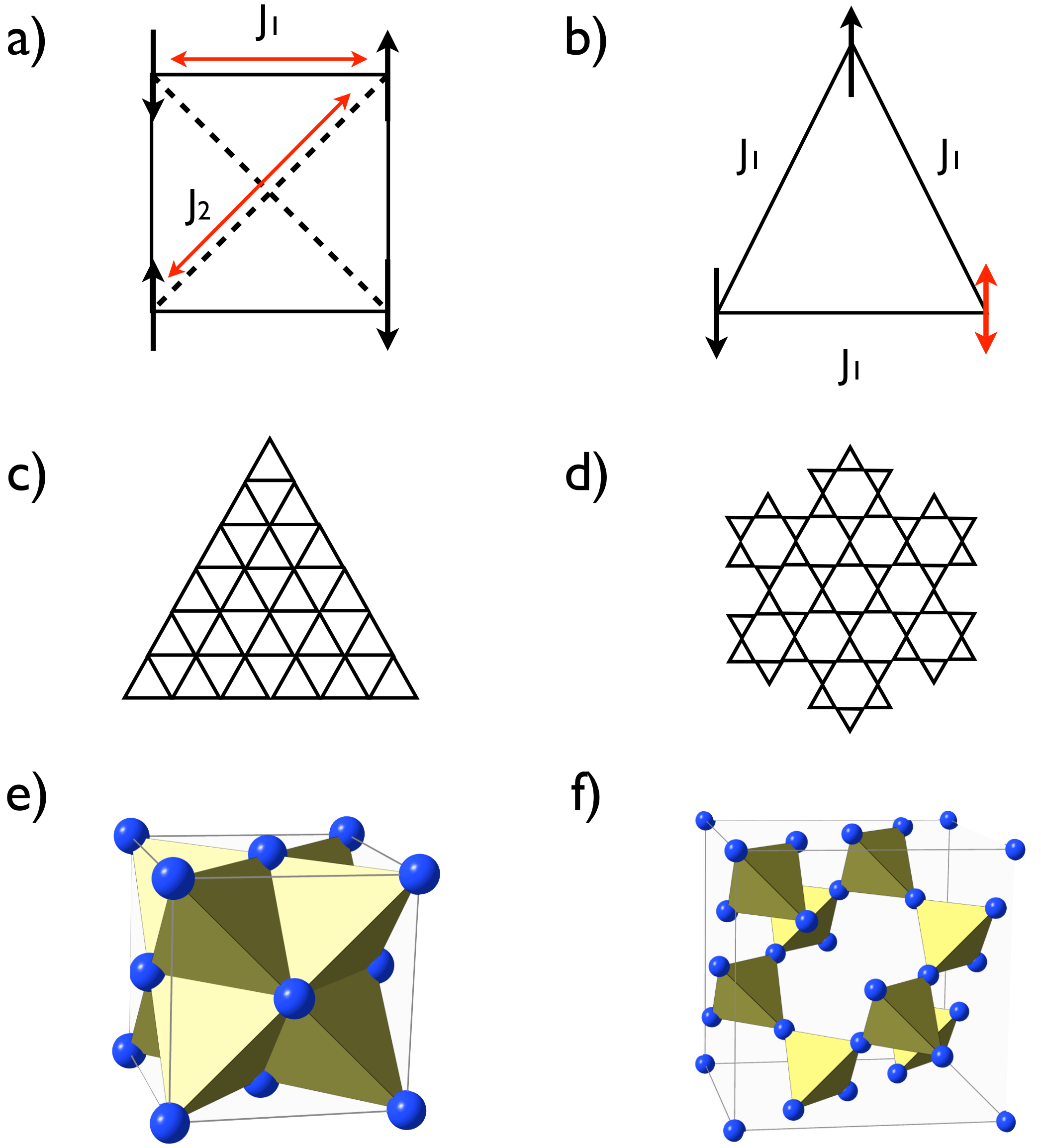

Figure 1.2: a) The frustrated J_1-J_2 model on the square lattice. J_1 is the AFM nearest neighbor exchange, and J_2 is the AFM next nearest neighbor exchange. b) Geometric frustration for AFM Ising spins on a triangular plaquette. The red spin cannot minimize its exchange energy with both of its nearest neighbors. c) Triangular lattice, made of edge-sharing triangles. d) Kagome lattice, made of corner-sharing triangles. e) Face centered cubic lattice, made of edge-sharing tetrahedra. f) The pyrochlore lattice, made of corner-sharing tetrahedra.

for highly frustrated magnetism, one is drawn to the pyrochlore or kagome systems.

A disordered ground state scenario, such as one resulting from “ideal” or robust frustration, violates the third law of thermodynamics because the entropy of such a system does not vanish at zero temperature. Thus, a single ground state must be selected eventually if the system remains in equilibrium (i.e. does not freeze). In real systems, this ground state could be selected by weaker terms in the Hamiltonian that are not accounted for in the simple models, such as long-range dipolar interactions, further neighbor exchange interactions, structural distortions, low energy excitations, etc. Even if a weaker term causes the transition to LRO, the effect of frustration is to suppress the transition to a temperature scale that is low compared to the strength of the exchange. This creates a strongly interacting system without LRO, which can give rise to rich physics. In such a system, the magnetic moments could be strongly correlated and remain dynamic, or they could freeze into static disordered configurations. The type of correlations experienced is different depending on the details fo the weaker terms in the Hamiltonian, leading to a wide variety of low temperature states that can be explored. A fine example of such a diversity of magnetic behaviour is found in the rare-earth titanate series of compounds, which have structures that include a magnetic pyrochlore sublattice. A discussion of some of the observed magnetic states in that series is presented in a recent review on pyrochlore oxides, Ref. 7.

On the pyrochlore lattice, geometric frustration is known to arise in two types of models; i) AFM coupled Heisenberg spins, or ii) FM coupled Ising-like

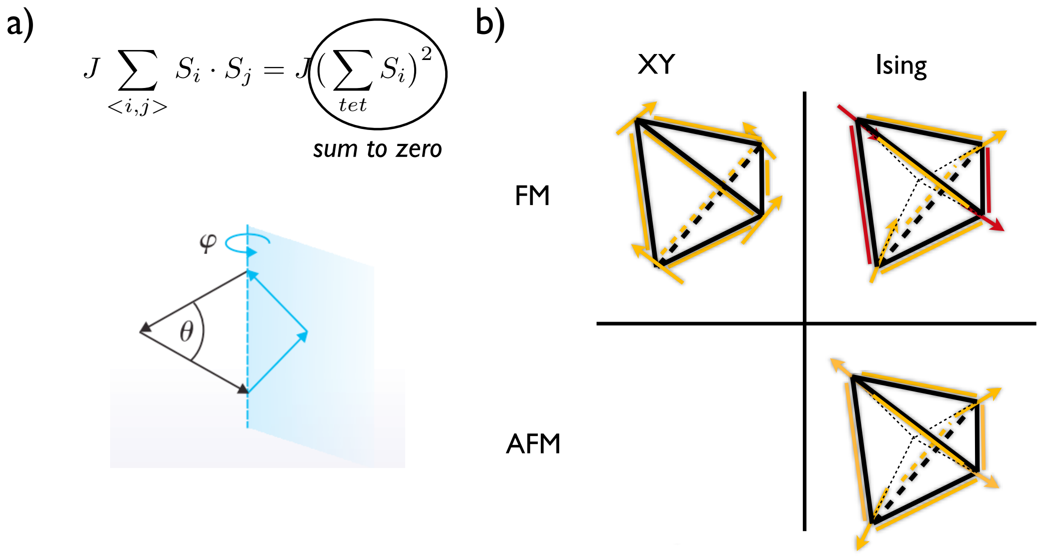

Figure 1.3: a) The AFM nearest neighbor isotropic exchange Hamiltonian on the pyrochlore lattice can be rewritten as the square of the sum of spins on a tetrahedron. This form makes it clear that any spin configuration in which the total moment per tetrahedron adds to zero will be a ground state. This leaves two degrees of freedom in choosing the spin configuration for each tetrahedron, as illustrated here by the angles ϕ and θ (bottom panel reprinted from Ref. [1]). b) Combinations of different types of local single-ion anisotropy (XY or Ising like) with different types of exchange interactions (FM or AFM) on a tetrahedron. Only the Ising-like anisotropy with ferromagnetic exchange leads to a degenerate ground state. The frustrated bonds are shown in red and the local Ising directions are shown by the dotted lines.

spins. Figure 1.3 a) shows the degeneracy that is inherent in the AFM coupled spins on a single tetrahedron. For the AFM Heisenberg model on a pyrochlore lattice, any configuration where the total spin for each tetrahedron sums to zero will be a ground state. This gives two internal degrees of freedom for the spin configurations of each tetrahedron (angles θ and ϕ shown in Figure 1.3 a)), and this results in a macroscopic degeneracy of the ground state[1]. Case ii), FM coupled Ising spins, may seem a more surprising route to frustration.

But it is because in this case, the Ising-like nature of the FM coupled spins is not *global*. Instead, the Ising axis is defined locally for each corner of the tetrahedron - the local $\langle 111 \rangle$ axis. FM coupled spins with this constraint can be mapped onto the AFM *global* Ising model on the pyrochlore lattice, which is indeed frustrated [8]. Case ii) is realized in the classical spin ice pyrochlores $Ho_2Ti_2O_7$ and $Dy_2Ti_2O_7$. The neutron scattering experiments presented in this thesis have shown that $Yb_2Ti_2O_7$ can also be described by such a model, but with the addition of quantum fluctuations (see Chapter 4). The combination of frustration and quantum fluctuations in $Yb_2Ti_2O_7$ makes it a possible candidate for "quantum spin liquid" behaviour, described next.

1.1.1.3 Spin Liquids and Quantum Spin Liquids

An interesting possibility for an alternative ground state that could emerge from a strongly correlated system in the absence of LRO is called a "spin liquid", a term which correctly calls to mind dynamic spin correlations. In a spin liquid, the spins do not freeze into any static configuration, neither long- nor short-range correlated. In one-dimensional models, the spin liquid is known to exist all the way to $T = 0$. In two-dimensions and higher, its exsitence as a true ground state remains a matter of some debate.

In 2D and 3D, it is true that for temperatures above absolute zero the spin liquid can indeed exist as a state where spins are highly correlated but remain dynamic due to thermal fluctuations. This type of *classical* spin liquid is also called a co-operative paramagnet [9]. It is a state that may arise in the temperature regime below the energy scale of the interactions, but above any "perturbatively" induced transition to LRO.

A related state, and one which is more exotic and represents a true *ground* state (i.e. it exists at T=0), is called a "quantum spin liquid" (QSL). One criteria of a QSL is long-range quantum entanglement between localized spins on the lattice [10]. This means, for example, that anti-ferromagnetically coupled spins with s=1/2 can become entangled within singlet states having total S=0. One particular type of QSL, the Resonating Valence Bond (RVB) state [11], is written as a superposition of all possible pairwise entangled states. Thus, any individual singlet-covering of the lattice is not stable, and the system will fluctuate between all possibilities even at T=0, via quantum fluctuations.

The QSL is of interest both for its fundamentally quantum mechanical character, and for the novel emergent qauntum excitations it is known to support. In a particular type of QSL that is relevant to spin-1/2 moments on a pyrochlore lattice, Coulombic physics arises from the U(1) symmetry of the model [12]. The excitations within the Coulombic "universe" made by the QSL ground state are anologues of magnetic monopoles, electric monopoles, and photons. This U(1) QSL is predicted to occur in the phase diagram for spin-1/2 pyrochlores (or effective spin-1/2 pyrochlores like $Yb_2Ti_2O_7$), but it is not the only type of QSL that has been proposed. There is a wealth of literature relating to different types of QSLs and their excitations. See, for example, Ref. 13.

Experimentally, the signatures of any kind of QSL are quite ambiguous. One of the first tests is a lack of magnetic LRO of the ground state, which can be determined by μSR, neutron scattering, and susceptibility studies. Beyond this, one approach is to look for signatures of the unique excitations that arise.

Neutron scattering offers a powerful probe of the QSL. Firstly, neutrons can rule out conventional LRO, and secondly, the emergent excitations give unusual signals in the dynamic structure factor observed using inelastic neutron scattering. Spinon excitations, i.e. two free S=1/2 particles arising from a broken singlet, manifest themselves as a continuum of states observable in the dynamic structure factor. This continuum arises instead of a well-defined, resolution-limited spin wave type excitations with precise energy vs. momentum dispersions. In the case of a spinon excitation, the neutron creates two particles instead of just one, the latter being the the case of a magnon (a single spin flip) from a conventional ordered state. Because there are three particles involved in the scattering process, the momentum transfer of the neutron is not uniquely tied to its energy transfer, and one observes a broad range of scattering over energy and momentum space, with sharp upper and lower bounds (see, for example, the spectra arising from Cs_2CuCl_4 [14]). While such a continuum is not unique to a spin liquid ground state (it could come from two-phonon creation, for example), it is *consistent* with such a state, and is not commonly observed in conventional ground states.

A final point worth mentioning here is that there is a prediction for a U(1) QSL-type ground state on the pyrochlore lattice that *does* have partially ordered moments, the so-called “Coulomb Ferromagnet” [15]. This is possible because a component of the spins may acquire a non-zero magnetization while the remaining components fluctuate and/or form entangled states. Such a state has emergent Coulomb excitations similar to the U(1) QSL.

1.1.2 Spin-Orbit Coupling and Crystal Field Effects

Spin-orbit coupling, the interaction of the spin and orbital angular momenta of an ion, can be appreciable in heavy ions such as the rare earths. It can be conceptually understood using a relativistic argument. Though the orbital momentum, $\vec{L}$, is naturally described as being associated with an electron in an atom, it may also be thought of as a property of positively charged nucleus which "orbits" around the electron from the reference frame of the latter. Then, the magnetic field created by this accelerating charge couples to the spin of the electron, $\vec{S}$, through a usual Zeeman interaction. Thus, the heavier, and hence more positively charged the nucleus is, the stronger the magnetic field felt by the electronic spins will be [16]. Because the energy term that describes spin-orbit coupling, $\vec{L} \cdot \vec{S}$, does not commute with $\vec{L}$ and $\vec{S}$ separately, we must take the full angular momentum, $\vec{J} = \vec{S} + \vec{L}$, as the basic unit of angular momentum when treating rare-earth magnets. This also implies that the angular momentum will take on the spatial dependence of the orbital degrees of freedom, and thus the angular momentum eigenstates will be anisotropic for any ions that have anisotropic orbits (i.e $L > 0$).

For an isolated ion, there is a $(2J{+}1)$-fold degeneracy of the J_z eigenstates. But this degeneracy is lifted via the Stark effect when the ion is placed in the electric field generated by the ionic crystal lattice. The manner in which the J multiplet is split, i.e. the energy eigenvalues and the eigenfuctions of the

Crystal Electric Field (CEF) Hamiltonian, determines important low energy properties of the magnetic ions. Specifically, the ground state of the CEF Hamiltonian will determine the effective magnetic moment and the anisotropy of the moments, both of which are characterized by the g-tensor. The g-tensor plays the same role as the g-factor introduced in Section 1.1, but allows for anisotropic moments. The g-tensor will have the symmetry of the point group associated with the crystallographic site of the magnetic ion. In the pyrochlore lattice, the symmetry of the rare-earth site is trigonal, so that the g-tensor has two unique components; one parallel to the trigonal axis and the other in the plane perpendicular to this. The trigonal axis corresponds to the $\langle 111 \rangle$ directions at the rare-earth site that are directed along the the line towards the centers of the tetrahedra (the dotted lines in Fig. 1.3 b)).

The splitting of the J multiplet will select a particular ground state. In general, the ground state will be a non-degenerate energy level whenever possible. However, for an ion with an odd number of electrons, Kramer's theorem states that there must be at least a two-fold degeneracy of the ground state because it is protected by time-reversal symmetry. Reversing the angular momentum, an effect of time-reversal, must not lead to a lower energy state. Therefore, the ground state must consist of two time-reversed wavefunctions; a "doublet".

In some cases, the energy splitting to the next highest CEF level is very large compared to the other relevant magnetic energy scales in the problem, such as the exchange energy. In this case, we can treat the lowest energy level as being isolated, and the ground state wavefunction can be thought of as the only contribution to the angular momentum. In the case of a well-isolated Kramer's doublet, the angular momentum can be treated as an "effective spin-1/2", because there are two degrees of freedom left in the low-energy manifold. This is very convenient from an experimental perspective when looking for exotic quantum mechanical states; the presence of spin-1/2 type objects emphasizes quantum mechanical effects, but the size of the magnetic moments can be quite a bit larger than a "bare" spin-1/2 (which has a moment of $1\mu_B$, where for example, in $Yb_2Ti_2O_7$, the effective pseudo-spin 1/2 moment is $3.3\mu_B$ [17]). This makes *effective* spin-1/2 systems more amenable to relatively weakly interacting magnetic probes such as neutron scattering.

In addition to the generally anisotropic orbital contribution to the ground state wavefunction, another exchange anisotropy arises in the effective spin-1/2 model. The anisotropy of the g-tensor is absorbed into the exchange interactions. Thus there are two effects which can produce highly anisotropic exchange between effective spins in this type of model.

In the next section, an anisotropic exchange effective spin-1/2 Hamiltonian on the pyrochlore lattice is presented. This Hamiltonian is appropriate to $Yb_2Ti_2O_7$, a point that will be motivated in Section 1.3, and the relevant parameters for $Yb_2Ti_2O_7$ are determined in Chapter 4.

1.1.3 Anisotropic exchange on the pyrochlore lattice

The exchange interactions between spins on different sites can be written as a tensor to allow for the anisotropy discussed in the previous section. Symmetry allows four nearest neighbor exchange couplings (including a Dzyaloshinskii

Moriya interaction) on the pyrochlore lattice. There are then four components of the exchange tensor, which can be labelled J_1 through J_4. The rare-earth sites on a single tetrahedron within the pyrochlore lattice can be enumerated by which corner they occupy, 0 through 3. Considering a tetrahedron centered at the origin, and choosing site 0 to be the the ion at $\hat{r_0} = (111)/\sqrt{3}$, and site 1 to be the ion at $\hat{r_0} = (1\bar{1}\bar{1})/\sqrt{3}$ (see Figure 1.4), the exchange tensor linking the two sites can be written in the form (in global coordinates),

$$\mathbf{J}_{01} = \begin{pmatrix} J_2 & J_4 & J_4 \\ -J_4 & J_1 & J_3 \\ -J_4 & J_3 & J_1 \end{pmatrix}. \tag{1.9}$$

The exchange tensor for other pairs spins on the tetrahedron can be obtain by cubic rotations of this tensor (for details, see Section 4.A).

The exchange tensor for the effective spin-1/2 model already includes the contributions from the g-tensor, as discussed in the previous section. However, when including the Zeeman term in the Hamiltonian, the g-tensor enters explicitly. Then the modified Hamiltonian, written in global crystallographic coordinates, is given by,

$$H = \frac{1}{2}\sum_{ij} J_{ij}^{\mu\nu} S_i^{\mu} S_j^{\nu} - \mu_B H^{\mu} \sum_i g_i^{\mu\nu} S_i^{\nu}, \tag{1.10}$$

where μ and ν enumerate the global x, y, z coordinates, and i and j specify different sublattices on the tetrahedron, e.g. 0 through 3.

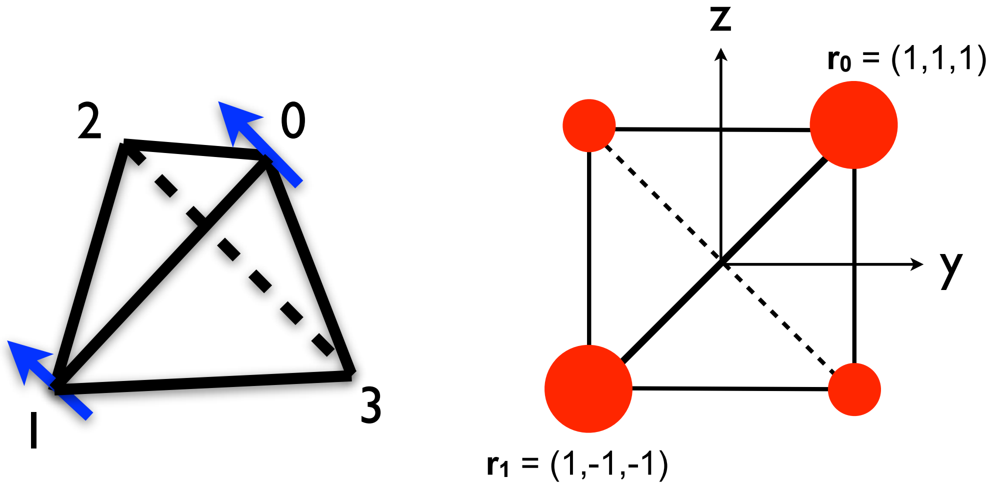

Figure 1.4: Labeling conventions of the four corners of a tetrahedron for the anisotropic exchange tensor, Eqn.1.9. Sites 0 and 1 are located at positions (1,1,1) and (1,-1,-1) if the tetrahedron is placed with its center at the origin (larger circles correspond to atoms that have positive x coordinates, small circles have negative x coordinates).

This effective spin-1/2 Hamiltonian on the pyrochlore lattice has been shown to support at least two exotic phases for specific ranges of J_1 through J_4; a QSL, and a polarized version of a QSL [15]. In Chapter 4, the appropriate values of the J parameters are obtained for $Yb_2Ti_2O_7$, and a discussion of their relevance to such exotic phases is provided.

1.2 $R_2Ti_2O_7$: Rare Earth Titanates

$Yb_2Ti_2O_7$ is part of a series of compounds called the rare-earth titanates. This series provides a diverse set of magnetic states on the pyrochlore lattice. The differences in the magnetic properties of these compounds is due to the inherently delicate balance of energy terms in frustrated systems. In part, the variety comes from differences in single-ion anisotropy (i.e. the g-tensor as described in Section 1.1.2), dipolar interactions, and the type of exchange between the moments. However, these compounds are nearly identical from a structural perspective.

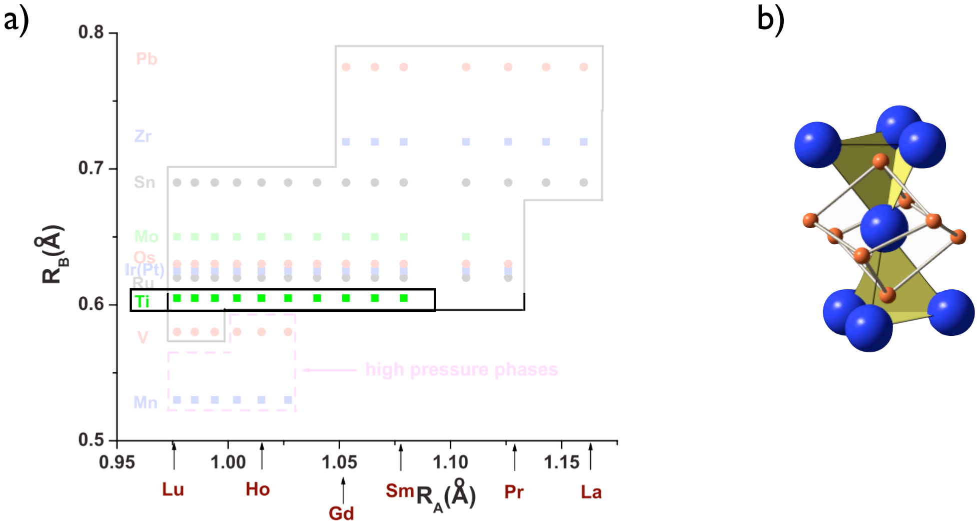

Figure 1.5: a) Stability field for the rare-earth titanates, adapted from Ref. 7. b) The distorted oxygen cube (red circles) environment of the rare-earth ions (blue circles) in the rare-earth titanates.

The general formula for the rare-earth titanates is $R_2Ti_2O_7$, where R stands in for a trivalent rare-earth ion. The stability field (the range of R ions compatible with the formation of a pyrochlore structure) is shown in Figure 1.5 a), which is adapted from Ref. 7. These compounds take up the Fd$\bar{3}$m space group. Both the (magnetic) R^{3+} and (non-magnetic) Ti^{4+} ions form interpenetrating pyrochlore sublattices. The R ion sits inside a distorted cube of oxygen ions, with two of the oxygen positions being in the center of two corner-sharing

R tetrahedra (Fig. 1.5 b)). The bonds from R to these two O^{2-} ions define the local ⟨111⟩ ("Ising") directions for each R position. The other six O^{2-} ions form a buckled hexagon around the R position, and the degree of "buckling" is controlled by the only free parameter in the structure, a position coordinate for one oxygen site. The details of the structure are described fully in Chapter 5.

The rare-earth titanates are ideal candidates for study by neutron scattering because they can be grown in large, high-quality single crystal form using the Optical Floating Zone (OFZ) method. The availability of single crystals is paramount to a full understanding of magnetic dynamics and correlations, which are usually anisotropic. Anisotropic effects are spatially averaged when powder samples are studied, so many of the details remain hidden. Thus, the study of rare-earth titanates provides a distinct advantage over the isostructural rare-earth stannates ($R_2Sn_2O_7$), for example, because the latter cannot be grown as large single crystals due to evaporation of Sn during the high temperature OFZ growths.

There is a wealth of information relating to the properties of several compounds in the rare-earth titanate series. Many details can be found in a recent review by Gardner, Greedan and Gingras [7]. In particular, $Tb_2Ti_2O_7$, $Er_2Ti_2O_7$, $Ho_2Ti_2O_7$, $Dy_2Ti_2O_7$ and $Gd_2Ti_2O_7$ are well-studied. Of these, only $Er_2Ti_2O_7$ and $Gd_2Ti_2O_7$ unambiguously form LRO ground states and are not frustrated, but do display other unique characteristics; $Er_2Ti_2O_7$'s ground state has been shown to be selected by quantum order-by-disorder

[18, 19], and $Gd_2Ti_2O_7$ undergoes a partial ordering transition prior to a final transition into a unique magnetic structure [20].

$Ho_2Ti_2O_7$ and $Dy_2Ti_2O_7$ are known as the classical dipolar spin ices. In both materials, the crystal electric field leaves a well-isolated doublet with strongly anisotropic g-tensors. The moments point along the local $\langle 111 \rangle$ directions (i.e. pointing into and out of the tetrahedra). Furthermore, the combination of the bare exchange interaction, plus the long-range dipolar interaction, forms an effectively ferromagnetic exchange between these moments [3]. The local Ising-like nature combined with ferromagnetic exchange realizes a frustrated model on the pyrochlore lattice, as discussed in Section 1.1.1.2. In such spin ices, each tetrahedron's minimum energy configuration is constructed from two spins pointing in, and two spins pointing out. This choice is 6-fold degenerate for each tetrahedron, and hence a macroscopic degeneracy is produced for the whole pyrochlore lattice. The spin ice ground state manifold of "two-in, two-out" configurations can be excited by thermal energy. The spin-flip excitations in spin ice create "three-in, one-out" type defects, which have been intriguingly shown to be equivalent to deconfined magnetic monopoles in the spin ice "vacuum" [21]. The analogy of magnetic monopoles arises from a mapping of the spins onto mangetic flux lines, with divergences (monopoles) subject to Coulomb interactions as expected for a magnetic charge. This "Coulomb phase" is quite similar to that of the U(1) QSL's mentioned in Section 1.1.1.3, though the latter are more complete Coulomb phases, containing analogues to electric as well as magnetic fields, and additionally supporting emergent gauge photons.

A spin liquid state was discovered as a low temperature phase in $Tb_2Ti_2O_7$. The first neutron scattering experiment exposed that $Tb_2Ti_2O_7$ does not order or freeze down to 30mK; instead, the spins remain short-range correlated and dynamic [22]. This lack of magnetic LRO is a sign of spin liquid type behaviour, either classical (LRO is destabilized by thermal fluctuations) or quantum (LRO is destabilized by *quantum* fluctuations, which arise when the system tunnels between different spin configurations). This is a robust result, yet the reason for the lack of magnetic order in $Tb_2Ti_2O_7$ has been a mystery until recently. $Tb_2Ti_2O_7$'s near neighbor exchange is AFM, which when coupled with Ising-like moments resulting from the CEF ground state, would be expected to produce the "all-in, all-out" ordered spin-configuration [3], which is not observed. The resolution of this problem is possibly related to the relatively small energy gap to the first excited CEF level, which is at $\sim$18K [23] (compare to 680K in $Yb_2Ti_2O_7$[24]). It has been proposed that virtual (quantum) excitations to this level renormalize the exchange interaction such that it becomes *ferromagnetic*, and hence frustrated [25]. In this sense, $Tb_2Ti_2O_7$ could be thought of as a "quantum spin ice". In Chapter 4 it is shown that $Yb_2Ti_2O_7$ can also be described as a quantum spin ice, but the mechanism differs from $Tb_2Ti_2O_7$. In $Yb_2Ti_2O_7$'s case, the spin ice character arises from predominantly ferromagnetic and Ising-like anisotropy of the exchange interactions, but significant quantum fluctuations are induced by the smaller planar exchange terms.

1.3 Previous Studies of $Yb_2Ti_2O_7$

In 1969, Blote *et al* reported on the specific heat of several pyrochlore oxides down to dilution refrigerator temperatures (30mK) [26]. In that study, the specific heat showed two peaks, one of which is broad and centered on 2K, and the other sharp and occuring at 240mK. The lower temperature, sharp peak, was assumed to signal a phase transition to a long-range-ordered state. This conjecture has since been the subject of some debate, as will be reviewed in this section and in Chapters 2 and 3.

Susceptibility measurements by Bramwell *et al* found a positive Curie-Weiss temperature between θ_{CW} = 490mK and 700mK, depending on details of analysis of the inverse susceptibility [17]. Blöte *et al* found θ_{CW}=400mK [26], while Hodges *et al* found θ_{CW}=750mK [27]. These small, but positive, Curie-Weiss temperatures indicate an overall *ferromagnetic* interaction between Yb^{3+} ions in $Yb_2Ti_2O_7$. Some insight into the variation of these numbers can be found in Refs. 17 and 5 which point out the non-linearity of the inverse susceptibility with temperature, creating a strong dependence on the temperature range that is used in the fitting procedure. Bramwell *et al* also report a temperature-dependent effective moment, which falls from ~4 μ_B at room temperature to 3.3 μ_B at 300mK [17]. The values are smaller than the single-ion effective moment of 4.54μ_B, expected for L=3 and S=1/2, which suggests the ions are restricted to CEF levels with reduced moments even at room temperature. That the effective moment is temperature dependent indicates the anisotropic nature of the moments, which can modify the form of the Curie-Weiss law such that $\chi^{-1}(T)$ is non-linear. This is explicitly discussed with respect to $Yb_2Ti_2O_7$ in Ref. 5. Another possibility is that the first excited crystal field level is relatively well-populated at room temperature and becomes de-populated as the system is cooled. However, the CEF scheme is such that the next excited crystal field level is only ~14% occupied at room temperature, leading us to anticipate anisotropy as the important factor in understanding $Yb_2Ti_2O_7$'s magnetic properties.

The CEF scheme in $Yb_2Ti_2O_7$ has been studied by Hodges *et al*, who find that the ground state is a very well-isolated Kramer's doublet, separated by 620K from the ground state [27]. Analysis of the CEF ground state wavefuctions, as well as measurements of the hyperfine interaction via Mossbauer spectroscopy, reveals that the g-tensor is planar in nature, with $g_{||} = 1.79$ and $g_{\perp} = 4.27$. Malkin *et al*, using optical spectroscopy, find similar values (energy gap of 680K, with $g_{||} = 1.836$ and $g_{\perp} = 4.282$) [24].

Because of the large energy gap to the excited CEF levels, the moments are expected to be well-described by an effective S=1/2 model at all temperatures below ~ 600K. These moments are also ferromagnetically coupled and constrained by planar, or local XY-like anisotropy. This is in sharp contrast to the dipolar spin ices, which are ferromagnetically coupled with local *Ising*-like anisotropy. The latter case leads to geometric frustration and the development of spin ice physics, while $Yb_2Ti_2O_7$ appears at first glance to be unfrustrated due to the continuous degree of freedom afforded by the XY symmetry of the moments. The continuous degree of freedom should allow a compromise to be made such that the moments can order within their local easy-planes and maximize their components along the global $\langle 100 \rangle$ direction (see Figure 1.3 b)).

The above evidence strongs suggests that the sharp anomaly in the specific heat, reported first at $T = 214$mK [26], signals a phase transition to such an unfrustrated, ordered state. However, various reports in the literature have found evidence for a disordered, dynamic ground state below this anomaly. Hodges *et al* studied a polycrystalline ("powder") sample using μSR, and found a first-order drop in the spin-fluctuation rate at $T = 240$mK [28]. The moments were found to continue to fluctuate at a frequency of 10MHz below this transition. Furthermore, their powder neutron diffraction experiment revealed a buildup of short-range FM correlations but lacked evidence for magnetic Bragg peaks, which would indicate long-range magnetic order below 240mK. Gardner *et al* studied a powder sample using a spin-polarized neutron beam, and found some increase of intensity at the (111) Bragg position below $T = 240$mK. They also found that the beam was not depolarized upon scattering from the sample, which indicates that a LRO FM structure of the type expected from the simple arguments presented above does not form [29]. Specifically, the lack of beam depolarization seemed to rule out the magnetic structure proposed by Yasui *et al* [30], in a study that for many years was the only one to find direct evidence for an ordered magnetic ground state in $\mathrm{Yb_2Ti_2O_7}$ below 240mK. In that study, neutron diffraction from a single crystal sample revealed the development of magnetic Bragg peaks at nuclear-allowed positions below 240mK, which the authors determined to be consistent with a simple collinear FM state described by moments oriented along a global [100] direction. This study also found a long time-scale of relaxation on the order of 2 hours below the transition. Hence, there has been some controversy in the literature regarding the true nature of the magnetic ground state in $Yb_2Ti_2O_7$.

In addition to controversy about the ground state, there was also an early report on unusual diffuse magnetic neutron scattering from a single crystal of $Yb_2Ti_2O_7$ [31]. This diffraction study, performed at millikelvin temperatures with no applied magnetic field, showed that *rods* of diffuse scattering pattern the HHL plane along equivalent $\langle 111 \rangle$ directions. These features appeared to exist at all temperatures, even below the transition temperature. The rods of scattering are unusual because they imply two-dimensional spin correlations, as will be described in Section 1.4. Since $Yb_2Ti_2O_7$ has cubic symmetry, the origin of such two-dimensionality is not obvious.

Chapters 2 and 3 of this thesis describe additional studies of these diffuse magnetic features. In those chapters we confirm the existence of rods, and show that they have subtle temperature dependence corresponding to a dimensional crossover that does not lead to a long-range magnetically ordered state. In Chapter 3 it is also shown that the discrepancy in the literature revolving around $Yb_2Ti_2O_7$'s ground state may be a consequence of the sample dependence revealed by specific heat studies. Chapter 5 addresses the source of the sample dependence and suggests a path towards resolving the issue.

Chapter 2 first reveals that the application of a magnetic field along $\langle 110 \rangle$ induces a long-range ordered state. This allows one to study the spin wave excitations using inelastic neutron scattering. In Chapter 4, the spin wave excitations from the field-induced LRO state are modeled using the anisotropic exchange Hamiltonian, Eqn. 1.10, and the four symmetry-allowed exchange terms are extracted. The success of that model has now extended beyond the remarkable agreement with the excitations in the field-induced state, to successfully describe the temperature- and field-dependence of measured thermodynamic quantities such as the magnetization and specific heat [32]. It has revealed that the exchange interactions in $Yb_2Ti_2O_7$ take on a spin ice character with quantum fluctuations, despite the planar anisotropy of the moments.

Though the work described in Chapter 4 definitively quantifies the exchange couplings for the first time, the expectation for anisotropic exchange in $Yb_2Ti_2O_7$ is not new. An anisotropic exchange model is well-motivated by several other studies. In thermodynamic studies, it is difficult to gain access to this anisotropy because it is averaged over the four sets of local coordinates for each tetrahedron. Neutron scattering, as a microscopic probe, is ideal for accessing this information. A polarized neutron scattering experiment was analyzed to determine the local susceptibility (i.e. the susceptibility in the local coordinates of each ion) in several of the rare-earth titanates [33]. That study was the first to reveal that the exchange interaction is dominant and ferromagnetic along the local $\langle 111 \rangle$ directions, which has been confirmed by the results of Chapter 4 here. Onoda *et al* developed an effective spin-1/2 model with anisotropic superexchange for $Yb_2Ti_2O_7$ [34], which is equivalent in form to the one used later in Chapter 4.

Thompson *et al* used the same model and extracted exchange parameters for $Yb_2Ti_2O_7$ by fitting to the pattern of diffuse magnetic scattering in the 2D correlated paramagnetic state [35]. Although these parameters do not agree with those found in Chapter 4, and they also do not reproduce thermodynamic properties of $Yb_2Ti_2O_7$ as shown by Ref. 32, the study was interesting in that it showed that it is possible to produce rods of scattering from the full cubic symmetry of the pyrochlore lattice with anisotropic exchange. This point is further made by Chang *et al*, who performed polarized neutron diffraction experiments to study the rods of scattering, and extracted yet another set of inequivalent exchange parameters (which do not reproduce the spin wave excitations or the thermodynamic measurements) [36]. Thus, it appears that there are a range of parameters in this model that can produce rods of scattering.

1.4 Neutron scattering

1.4.1 General considerations

Neutrons interact weakly with matter. As uncharged particles, they do not experience a Coulomb interaction, so they have the ability to penetrate deeply into the bulk of the material. Neutrons do interact with the nuclei of atoms via the strong force, but this requires close contact between the neutrons and the nuclei, on the order of femtometers. The interaction potential between the neutron and the nucleus can be thought of as a delta-function at the nucleus, with a large amount of empty space between each nucleus, making any given interaction quite rare. Because of this, when neutrons interact with a sample, they typically undergo only a single scattering event, and hence the change in their kinetic properties can easily be interpreted. Furthermore, the scattering potential is weak enough that Born's first approximation can be used; the incident neutron field penetrating the sample is not appreciably modified by the nuclear potentials or scattered wavelets, so that each nucleus sees the same incident wavefunction.

Similar arguments apply to neutrons that scatter from magnetic centers. Neutrons have a magnetic dipole moment, $\vec{\mu}_n = \gamma \mu_N \vec{\sigma}_N$, where γ is the gyromagnetic ratio (equal to 1.93), μ_N is the nuclear magneton, and $\vec{\sigma}_N$ is the pauli spin operator for a spin 1/2 particle. Thus, a neutron can interact with magnetic fields created by dipole moments in the crystal, such as those formed by unpaired electrons. The strength of magnetic scattering for materials with unpaired electrons can be comparable to the nuclear scattering. This makes neutrons useful as a microscopic probe of magnetism in materials.

Using the techniques outlined in Section 1.4.3, one can measure the change in the neutron's momentum and energy after it scatters from the sample. This leads us to an understanding of the distribution of momentum and energy scales in the system, allowing us to directly measure the static and/or dynamic correlations between atoms (nuclear scattering) or spins (magnetic scattering).

The cross section of interaction between neutrons and matter is well-described by Fermi's Golden Rule, an expression based on first-order perturbation theory in quantum mechanics:

$$\frac{d^2\sigma}{d\Omega dE'} = \frac{k'}{k}(\frac{m}{2\pi\hbar^2})^2 |\langle k'\sigma'\lambda'|V|k\sigma_0\lambda_0\rangle|^2 \cdot \delta(E_{\lambda_0} - E_{\lambda'} + \hbar\omega) \tag{1.11}$$

On the left hand side, σ is the cross section, $d\Omega$ is a solid angle element into which the neutrons are scattered, and dE' is the final energy of the neutron. On the right hand side, k and k' are the initial and final wavenumbers of the neutron, $|k\sigma_0\lambda_0\rangle$ and $|k'\sigma'\lambda'\rangle$ are the initial and final composite wavefuctions of the neutron (with wavenumber k and spin σ) and the crystal, the latter simply labelled by λ. V is the interaction potential, which has contributions from magnetic and nuclear scattering centers. E_{λ_0} and $E_{\lambda'}$ are the initial and final energy of the crystal, while $\hbar\omega$ is the energy transfer of the neutron; the delta function expresses that energy is conserved in the collision between the neutron and the crystal.

Because the neutron's wavefunction before and after scattering is that of a plane wave with wavevector $\vec{k}$, i.e. $\psi \propto e^{i\vec{k}\cdot\vec{r}}$, the term

$$\langle k'\sigma'\lambda'|V|k\sigma_0\lambda_0\rangle = \int V(\vec{r})e^{(\vec{k}-\vec{k}')\cdot\vec{r}}d\vec{r} \tag{1.12}$$

shows that the wave nature of the neutron causes the scattered intensity to be the spatial Fourier transform of the full crystal potential function. In particular the scattering vector, $\vec{Q} = \vec{k}' - \vec{k}$, can be interpreted as a point in the reciprocal space.

Further manipulation of Eqn. 1.11 reveals that the energy dependence of the inelastic cross section (arising from events in which the neutron exchanges some energy with the crystal) is a Fourier transform of the time dependence of the pairwise correlations [37].

Thus, all features observed in neutron scattering experiments which measure the above cross section have the following general mappings to the system:

- Features that are broad in reciprocal space correspond to short-range correlations in real space, and vice versa. Broad features in a scattering pattern are called "diffuse". The spatial correlation length is given by,

  $$\xi = a/\Gamma, \tag{1.13}$$

  where Γ is the Half Width at Half Maximum (HWHM) of the peak in reciprocal lattice units.

- Features that are broad in energy transfer correspond to short-lived excitations. Resolution-limited features correspond to long-lived excitations. The lifetime is related to the HWHM of a peak in an energy scan, $\Delta t = 2\pi\hbar/\Delta E$.

1.4.1.1 Bragg's Law

The wave-nature of particles makes the scattering of neutrons analogous to scattering by electromagnetic radiation such as x-rays, where Bragg's law for diffraction from crystal planes was first encountered.

The scattering centers in a crystal are arranged in a periodic fashion. In particular directions there will appear to be repeating planes of scatterers that are separated by a distance, d. When a plane-wave (for example, the neutron's wavefunction) is incident upon these planes, parts of it will scatter at each layer. The scattered waves will interfere constructively when a certain condition, called Bragg's law, is satisfied by the geometry of the scattering event.

Constructive interference occurs at a specific angle with respect to the incident beam for a given d-spacing and wavelength. If one were to scan a detector through all possible angles into which neutrons could scatter, sharp peaks of intensity would be observed at the angle given by Bragg's law - these are called Bragg peaks. Bragg's law can be written as,

$$n\lambda = 2d\sin(\theta) \tag{1.14}$$

where n is an integer corresponding to harmonics of the incident wavelength λ (here the scattered wavelength is also assumed to be λ, i.e. the scattering is elastic), and θ is the angle that both the incident and scattered beams make with the normal to the scattering planes.

Bragg's law can also be recast into another form involving the reciprocal lattice vector connecting the two scattering centers. This allows a more direct connection to solid state formalism, which is necessarily written in reciprocal space. Furthermore, it highlights the geometric degrees of freedom at the sample position - a single crystal must have a reciprocal lattice vector $\vec{Q}$ be equal to the difference between the incident and scattered wavevectors of the neutron beam, i.e. $\vec{Q} = \vec{k}_f - \vec{k}_i$, in order to see a Bragg peak at the specified θ, given by a rearranged Bragg's law:

$$Q = \frac{4\pi \sin(\theta)}{\lambda}. \tag{1.15}$$

1.4.1.2 Rods of Diffuse Scattering

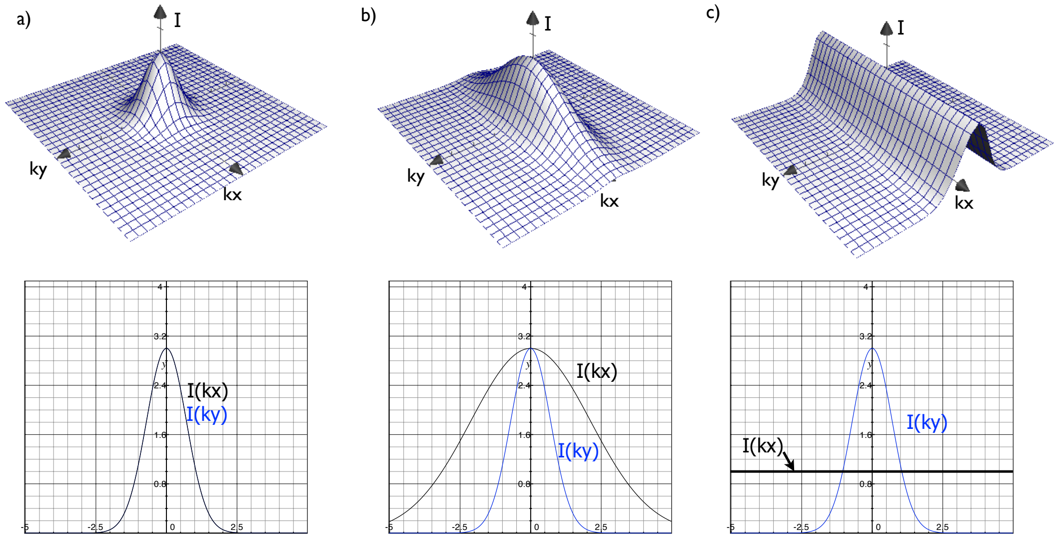

Figure 1.6: Simulated plots of neutron scattering intensity vs. two wavevectors. a) For long-range order in both x and y directions, a sharp feature (Bragg peak) is observed. b) When the correlation length along the x direction becomes short, the scattering feature broadens in the k_x direction. c) In the limit where no correlations exist in the x direction, the scattering feature looks like a "rod" of scattering.

A sharp peak of scattered intensity (a Bragg peak) is an indication of a long-range correlated periodic structure, such as a set of lattice planes with well-defined d-spacing. However, as Eqn. 1.13 shows, the broader the peak (as measured in reciprocal space, (which is related to angular scans of the detector around the sample via Eqn. 1.15), the shorter-range the spatial correlations become.

Imagine the scattering signal from a well-ordered sample in a particular scattering plane, the $k_x - k_y$ plane. The scattering signal would look like an instrumental resolution-limited peak, similar to that shown in Fig. 1.6a). If one relaxes the perfectly long-range order in one direction (x), the signal will still be resolution-limited in k_y but will have a larger HWHM in k_x (Fig. 1.6b). Taking this argument to the limit where there is a complete lack of correlation between planes in the x direction, one would observe a “rod” of scattering which extends along the k_x direction (Fig. 1.6c). In a three-dimensional sample, a rod of scattering such as this indicates two-dimensional correlations (i.e. only one direction is uncorrelated in real space). This is the basis for the discussion of rods of scattering in Chapters 2 and 3.

1.4.1.3 Elastic, quasi-elastic and inelastic scattering

Elastic scattering refers to events in which the neutron does not exchange energy with the system, only crystal momentum (i.e. the momentum is conserved to within a reciprocal lattice vector). Selecting scattering events that are purely elastic gives information on static spatial correlations. Thus, the elastic scattering contains the nuclear and magnetic Bragg peaks, i.e. resolution limited “spots” of intensity, since these are characteristic of a static repeating structure. If a short-range correlated structure is “frozen” into the system, as in the case of glasses, it will give rise to diffuse elastic scattering. In practice, what one calls the elastic scattering is dependent on the energy resolution of the instrument. This means that there is a range of timescales over which the neutron scattering measurement cannot distinguish purely static from slowly fluctuating correlations. Using cold neutrons, which have relatively long wavelengths (above 2 Å), a typical energy resolution is typically 1meV and lower. For example, the resolution of the measurements presented in this thesis is 0.1meV, corresponding to a lower limit of resolvable frequencies of 24 GHz. Meanwhile, μSR and NMR can access lower frequencies; between 0.01 MHz and 10GHz. This is one reason why these local magnetic probes complement neutron scattering studies so well.

"Quasi-elastic" scattering refers to scattering that is centered at $\hbar\omega$=0, but the energy dependence has a characteristic width that is larger than the instrumental resolution. This implies slow relaxation of nearly static correlations.

Finally, inelastic scattering is intensity that is centered on a non-zero energy transfer. Phonons (lattice vibrations) and magnons (spin waves) have well-defined energy-momentum dispersion relations that can be measured using inelastic scattering. Furthermore, the pattern of intensity of the inelastic scattering gives information on the matrix elements of the interaction Hamiltonian that link the ground state to that excited state.

1.4.2 Nuclear and Magnetic scattering

The potential, V, in Eqn. 1.11 is made up of a nuclear potential, V_N, and a magnetic potential, V_m. The scattering from the two potentials can be treated separately, since there are no interference terms between nuclear and magnetic

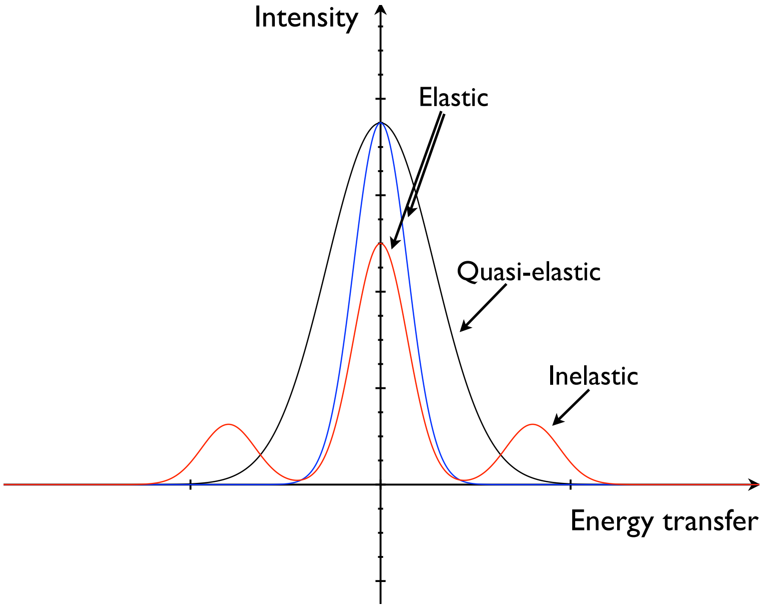

Figure 1.7: Illustration of different types of scattering, plotted as scattered intensity vs. energy transfer of the neutron. Elastic scattering is concentrated at zero energy transfer and its width is resolution-limited. Quasi-elastic scattering is centered at zero energy transfer, but has an intrinsic width that is larger than the resolution of the instrument. Inelastic scattering is centered on non-zero energy transfer and can be resolution-limited or not, depending on the intrinsic lifetime of the excitation it corresponds to.

scattering for experiments that do not use spin-polarized neutron beams [38]. In this case, the two cross sections are always summed together, allowing magnetic scattering to be isolated by a subtraction of the nuclear component. The nuclear component can often be isolated by raising the temperature of the sample above the energy scale at which magnetic correlations develop.

1.4.2.1 Nuclear scattering

The nuclear potential can be written as,

$$V_N(\vec{r}) = \frac{2\pi\hbar^2}{m_n} \sum_{\vec{R}} b_{\vec{R}} \delta(\vec{r} - \vec{R}) \tag{1.16}$$

where $b_{\vec{R}}$ is the scattering length of the nucleus located at position $\vec{R}$ in the lattice. The scattering length appears to vary randomly from element to element, and even from isotope to isotope. Thus, unlike x-rays, neutrons are sensitive to some very light elements as well as some heavy elements, making neutron scattering a useful probe in certain structural characterizations (such as those involving oxygen, which has a relatively large neutron scattering cross-section compared to its x-ray cross section). The nuclear scattering length can also be negative, which indicates that there is no bound state between the nucleus and the neutron [39]; this is somewhat rare, but does occur in the case of naturally occuring titanium, and thus it is relevant to the rare-earth titanates. The negative scattering length can be of use in neutron crystallography where it creates contrast between elements with positive and negative scattering lengths in the nuclear structure factor (Eqn. 1.19). Chapter 5 describes such a case, in which the presence of either ytterbium or titanium on a particular crystallographic site can be precisely distinguished owing to this added contrast in scattering lengths.

Because of the random distribution of the naturally abundant nuclear isotopes throughout the crystal, which each have different scattering lengths and nuclear moments, part of the nuclear scattering cross-section is composed of “incoherent” scattering. This type of scattering occurs because different scattering centers are uncorrelated in space, resulting in an elastic signal which is roughly independent of $\vec{Q}$. “Coherent” scattering is the portion of the cross-section that involves the average scattering length for a particular element; when viewed as an average, the periodic nature of the crystal shows up as angular dependence of the coherent scattering.

Below, only the cross section for *elastic* coherent nuclear scattering from a *long-range ordered* lattice is considered, and it is the only relevant nuclear cross section for the work in this thesis. This is not the most general form of the cross section - generally, the atomic positions within the lattice are not necessarily long-range ordered, in which case one may not employ delta functions such as $\delta(\vec{Q}-\vec{K})$ that result in perfectly sharp Bragg peaks. Furthermore, nuclear inelastic scattering, in which phonon excitations are probed, will not be considered here.

The coherent elastic nuclear scattering cross-section for a perfectly ordered lattice can be written as,

$$\frac{d\sigma}{d\Omega} = \frac{N(2\pi)^3}{\nu_0} S(\vec{Q}), \tag{1.17}$$

with

$$S(\vec{Q}) = \sum_{\vec{K}} \delta(\vec{Q}-\vec{K}) |F_N(\vec{K})|^2 \tag{1.18}$$

where $\vec{Q} = \vec{k}' - \vec{k}$ is the "scattering vector", and $\vec{K}$ is a reciprocal lattice vector. $F_N(\vec{K})$ is called the nuclear structure factor, which is directly related to the real space structure of the unit cell. In particular, for a unit cell that has nuclei positioned at basis vectors $\vec{d}$ with scattering lengths $b_{\vec{d}}$,

$$F_N(\vec{K}) = \sum_{\vec{d}} b_{\vec{d}} \cdot e^{i\vec{K}\cdot\vec{d}}. \tag{1.19}$$

The study of crystallography depends on measurements of nuclear elastic scattering, and in particular, relative intensities of Bragg peaks. This is because one can determine the chemical structure based on a series of relative Bragg intensities. The intensity, or equivalently the number of neutrons counted with scattering vector $\vec{Q}$, is proportional to $S(\vec{Q})^2$. One can work backwards and determine the positions, $r_{\vec{d}}$, of particular atoms with scattering lengths $b_{\vec{d}}$, although information about the phases (encoded in the factor $e^{i\vec{K}\cdot\vec{d}}$) is lost upon squaring $S(\vec{Q})$. As a result, a *direct* mapping back to reciprocal space is impossible without the use of more advanced measurement techniques. Thus, one must provide a starting model from which to further refine the structure. The Rietveld refinements presented in Chapter 5 compare the $S(Q)$ measured by neutron powder diffraction to a calculation based on Eqn. 1.19, by starting with a model of the unit cell that contains some free positional parameters, which are constrained by the symmetry of the space group of the material in question. The free parameters are then adjusted to improve the agreement of the calculated $S(Q)$ profile with the data.

1.4.2.2 Magnetic scattering

The magnetic potential can be wrtten as $V_m = -\vec{\mu_n} \cdot \vec{B}$, where $\vec{B}$ arises from the mangetic dipoles created by unpaired electrons in the lattice. The *magnetic* differential cross section can be written as,

$$\frac{d^2\sigma}{d\Omega dE'} = \frac{k'}{k}\frac{(\gamma r_0)^2}{2\pi\hbar^2} N \left[\frac{1}{2} g F(\vec{Q})\right]^2 \sum_{\alpha,\beta} (\delta_{\alpha\beta} - \hat{Q}_\alpha \hat{Q}_\beta) \times \sum_{\vec{R}} e^{i\vec{Q}\cdot\vec{R}} \int_{-\infty}^{\infty} \langle S_0^\alpha(0) S_{\vec{R}}^\beta(t)\rangle e^{-i\omega t} dt \tag{1.20}$$

The most important aspects of this cross section are the following:

- $F(\vec{Q})$: This is the magnetic form factor. It describes the variation of intensity that is due to the extended nature of the magnetic scattering center. Unlike the potential from nuclear scattering centers, which can be considered to be delta functions when compared to the neutron's wavelength, the magnetic potential occupies a volume essentially defined by the orbital wavefunctions of the unpaired electrons in the crystal. The neutron's wavefunction can interfere with itself upon scattering from this extended object, and this interference is destructive for large $|Q|$ values (short distance scales). Therefore, the magnetic form factor suppresses intensity at higher $|Q|$ values, for both elastic and inelastic magnetic signals. This can be a useful tool in distinguishing magnetic excitations from phonons, since the intensity of latter generally increase as $|\vec{Q} \cdot \vec{\epsilon}|^2$, where $\vec{\epsilon}$ is the eigenvector of the phonon in question [37].

- $\langle S_0^\alpha(0) S_{\vec{R}}^\beta(t)\rangle$: This is the dynamic spin-spin correlation function. From the perspective of condensed matter research, this is the heart of the cross section, and what one sets out to measure in the magnetic neutron scattering experiment. It describes the correlations between a spin at the origin at time 0, and a spin at position $\vec{R}$ at time t. By measuring all possible final energies, dE', and solid angles $d\Omega$, one can learn the full spatial- and time-dependence of the pairwise spin correlations in the system, which provides invaluable insight into the microscopic state and the interactions which lead to it.

- $(\delta_{\alpha\beta} - \hat{Q}_\alpha \hat{Q}_\beta)$: This factor indicates that the cross section is only sensitive to components of the spin-spin correlations that are perpendicular to the scattering vector, $\vec{Q}$. This is as a consequence of the dipolar interaction between the neutron spin and the dipole field arising from the electronic magnetic moment. Because of this factor, even unpolarized neutron scattering experiments contain some information on the anisotropy of the spin-spin correlations.

1.4.3 Neutron scattering techniques

In this thesis, three neutron scattering techniques are employed. Two of them involve time-of-flight neutron scattering, which can be used for different purposes; inelastic neutron spectroscopy (Chapters 2 and 4) and powder diffraction (Chapter 5). The third technique was invented by Bertram Brockhouse (who later worked at McMaster University) in 1958, winning him a share of the 1994 Nobel prize for Physics; triple-axis neutron scattering (Chapter 3).

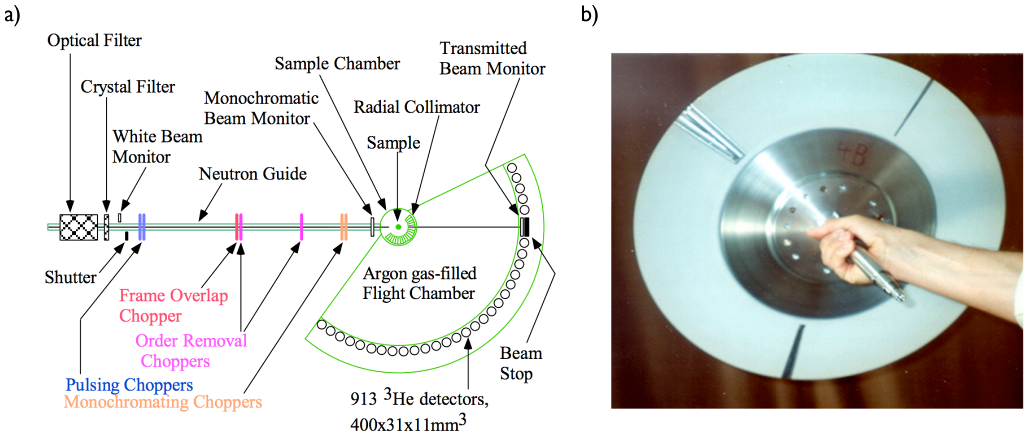

Figure 1.8: a) Schematic diagram of the Disk Chopper Spectrometer at NIST. b) One of the choppers from DCS. The white coating is gadolinium-based paint. The large, medium, and small slits allow for three energy resolution settings for any particular incident wavelength. Pictures are from http://www.ncnr.nist.gov/instruments/dcs/PosterNov2002.pdf.

Time-of-flight neutron scattering makes use of a bank of detectors that covers a large solid angle into which neutrons scatter. Fast electronics are used that can detect the time each scattered neutron arrives at a given detector. Knowing precisely the time of the neutron's arrival at the sample, as well as the distance from the sample to the detectors, one can then determine the speed, and therefore the wavelength, of the scattered neutron. This information could either be used to detect a change in energy of a monochromatic beam of incident neutrons after they scatter from the sample (i.e. inelastic neutron scattering), or to distinguish the wavelength of scattered neutrons originating from a white beam (i.e. energy-integrated scattering, or "diffraction"). The latter usage allows one to determine the d-spacing of the crystal plane which scattered the neutron, by using the wavelength and scattering angle in Bragg's law, Eqn. 1.14.

A schematic diagram of the Disk Chopper Spectrometer (DCS), located at the NIST Center for Neutron Research, is shown in Figure 1.8 a). This time-of-flight instrument first uses 7 "choppers" to produce a monochromatic beam of neutrons with the desired incident energy. The choppers, which consist of rotating disks coated in a highly neutron-absorbing material, gadolinium, have slits cut into them (Figure 1.8 b)) to allow the passage of neutrons when the slit lines up with the incident beam. The choppers rotate with specific relative phases with respect to one another, allowing only a narrow range of wavelengths centered on the desired wavelength to pass through. Those neutrons scatter from the sample, which could be contained in a number of different sample enviornments (for example, a dilution refrigerator plus an 11.5 Tesla superconducting maget, as used in the experiment leading to Chapters 2 and 4). The neutrons are detected by a stationary array of 913 Helium 3 detectors. The DCS was used to collect data shown in Chapter 2, parts of Chapter 3, and Chapter 4.

The NPDF instrument located at Los Alamos National Laboratory has a design similar to the DCS, but it lacks the choppers that would produce a monochromatic beam. Instead, pulses of neutrons are sent from the spallation source (at the LANSCE facility), which contain a broad spectrum of neutron wavelengths. All of these neutrons are allowed to scatter from the sample, which is typically in powder form. Four groups ("banks") of detectors are arranged in a solid angle around the sample space. By detecting the scattering angle and the time-of-flight of the neutron, one may reconstruct $S(|Q|)$ for a large range of $|Q|$. This technique is diffraction, since the singal is energy-integrated. Because elastic scattering is typically several orders of magnitude stronger than inelastic scattering, the diffraction signal consists almost entirely of information on static correlations such as crystal structure. The NPDF instrument was used to collect the data shown in Chapter 5.

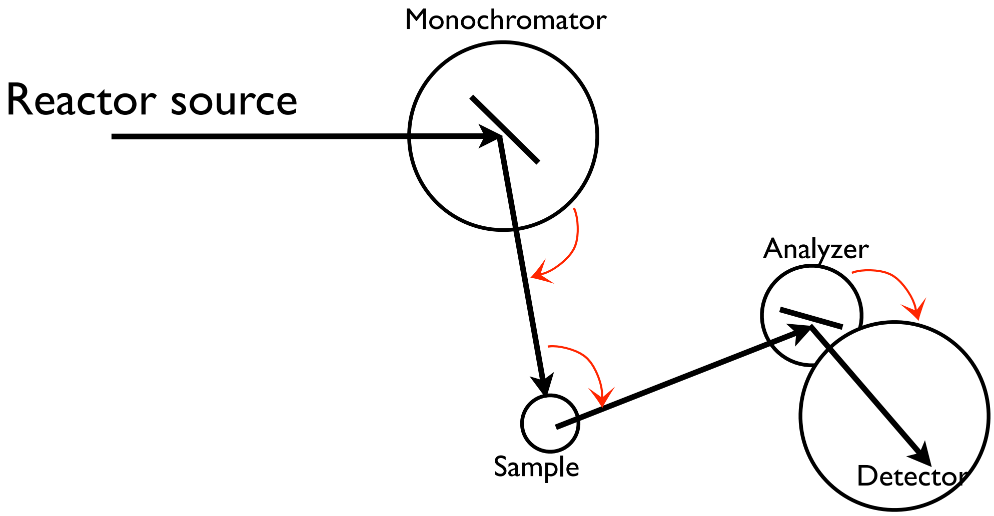

Figure 1.9: Schematic diagram of a triple-axis spectrometer.

A schematic diagram of a triple-axis spectrometer is shown in Figure 1.9. Such an instrument makes use of Bragg scattering from three objects mounted on three rotation axes; the monochromator crystal, the sample, and the analyzer crystal. The instrument can be rotated around the monochromator, which is a large crystal oriented along a particular crystallographic direction with known d-spacing. This selects the incident wavelength. The neutrons then scatter from the sample, about which the detector arm can be rotated to select a given $\vec{Q} = \vec{k}' - \vec{k}$. Finally, the detector itself can be rotated around an analyzer crystal, which selectively scatters neutrons with the desired final wavelength. One can then perform detailed measurements of the scattering intensity at selected $\vec{Q}$ and $\hbar\omega = E' - E$ points. For example, in Chapter 3, measurements are performed at two $\vec{Q}$ positions to obtain the scattered intensity as a function of temperature.

1.5 Crystal growth

The growth of high quality and large single crystals of the rare-earth titanates, as well as many other oxide materials, can be accomplished by the optical floating zone (OFZ) technique. This method involves melting ceramics (pressed polycrystalline rods) of the desired material using light from halogen lamps that is focussed to a small volume by two ellipsoidal mirrors (Figure 1.10 a)). Two ceramic rods are used; one as the seed rod (upon which the molten zone crystallizes) and the other is the feed rod that supplies material to the zone. By slowly moving the seed rod out of the focal point, the molten zone crystallizes on the seed rod and is replenished by the feed rod.

The total length of the growth is limited mainly by the length of ceramic rods that can be produced and the density with which they can be prepared. This method typically produces *single* crystals (i.e. the part of the growth that successfully excludes all competing “grains” of different orientations) that are 3 to 5cm long, and 0.5cm in diameter. These are usually cut from the full growth which can be ∼8cm long. Figure 1.10 b) shows the full growth of the $Yb_2Ti_2O_7$ crystal studied in Chapters 2, 3, and 4.

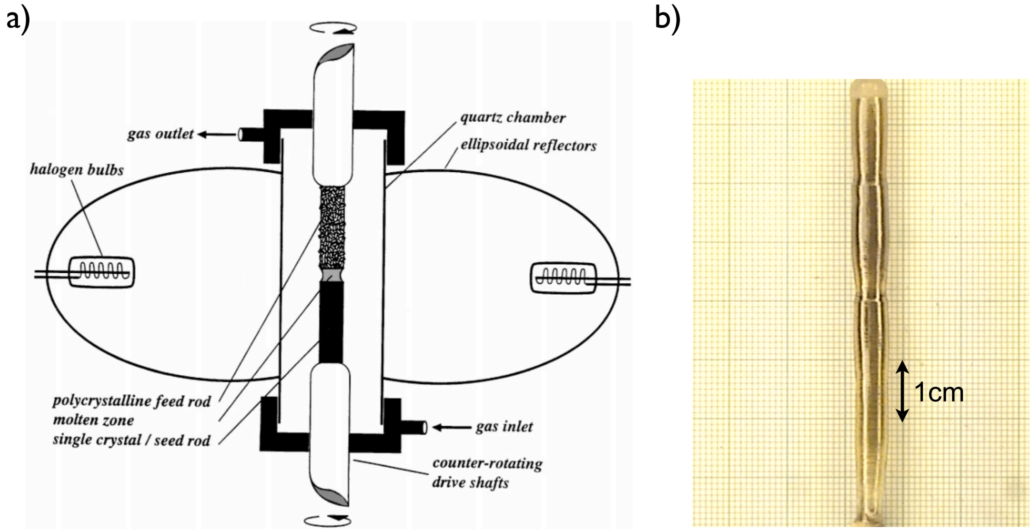

Figure 1.10: a) Schematic diagram of an optical floating zone furnace, from Ref. 40. b) Single crystal of $Yb_2Ti_2O_7$ grown by the optical floating zone method. A 3.5cm long mid-section of this growth was used in the neutron scattering experiments presented in this thesis.

One advantage of this growth method is that it avoids the use of crucibles or flux (the latter is avoided for congruently melting materials, in which all components of the starting material melt at the same temperature - this is the case for $Yb_2Ti_2O_7$), and so the molten zone is expected to be composed purely of the starting material. Additionally, the growth can be carried out inside a quartz tube pressurized with, in principle, any desired gaseous atmosphere. This is useful for minimizing the evaporation of volatile components of the zone [41], or encouraging the oxidation or reduction of certain ions such as vanadium.

It has been shown that OFZ growths of $Dy_2Ti_2O_7$ performed in air, argon and oxygen gas produce crystals of different colours and with significant differences in their magnetization [42]. This indicates that the oxygen stoichiometry plays some role in rare-earth titanates. Similar changes in colour have been observed for $Tb_2Ti_2O_7$ crystals grown in these environments [40]. In Chapter 5, a detailed neutron powder diffraction study is presented which proposes a model for the structural disorder known to exist in $Yb_2Ti_2O_7$ OFZ crystals (see Chapter 3 and Refs. [43, 36] which detail the evidence for this disorder). In that Chapter, it is shown that titanium non-stoichiometry also exists at the 3% level for the OFZ $Yb_2Ti_2O_7$ crystals. It should be expected that the titanium and oxygen contents will be related, since removing a Ti^{4+} atom and replacing it with Yb^{3+} (as proposed in that chapter) requires the loss of oxygen to maintain charge neutrality. Hence the growth atmosphere seems to be of considerable importance for the rare-earth titanates.

The rate at which the seed rod is pulled downwards plays a large role in determining the stability of the molten zone, and hence the quality of the single crystals. This rate is called the growth speed, and it can range from 0.2 mm/h to 10 mm/h depending on the material. The growth speed, combined with the halogen lamp power, work together to determine the temperature of the zone. This strongly influences the surface tension that is responsible for maintaining the zone. The growth speed also influences the cooling rate of the newly formed crystal front; if it cools too quickly, thermally activated defects can be frozen into the crystal. However, sometimes a faster growth rate is necessary to stabilize the zone and this "quenching" disadvantage must be tolerated. Generally, if the growth speed can be lowered, it is advantageous to do so.

Finally, counter-rotation of the feed and seed rods is useful in mixing the components of the zone thoroughly, and tends to avoid compositional gradients over the cross-section of the crystals.

The single crystals of $Yb_2Ti_2O_7$ that were used throughout the work that comprises this thesis were prepared by this method. The growth rate varied between 5-6 mm/h, and the gas environment was 4 atm of oxygen. The counter rotation speed was 30 rpm.

1.6 * References

[1] R. Moessner and A. P. Ramirez, Phys. Today **59**, 24 (2006).

[2] N. W. Ashcroft and N. D. Mermin, *Solid State Physics* (Holt Saunders, New York, 1976), Chap. 31.

[3] B. C. den Hertog and M. J. P. Gingras, Physical Review Letters **84**, 3430 (2000).

[4] M. Elhajal, B. Canals, R. Sunyer, and C. Lacroix, Physical Review B **71**, 094420 (2005).

[5] H. B. Cao, A. Gukasov, I. Mirebeau, and P. Bonville, J. Phys. : Condens. Matter **21**, 492202 (2009).

[6] P. Chandra and B. Doucot, Physical Review B **38**, 9335 (1988).

[7] J. S. Gardner, M. J. P. Gingras, and J. E. Greedan, Reviews of Modern Physics **82**, 53 (2010).

[8] R. Moessner, Physical Review B **57**, 5587 (1998).

[9] J. Villain, Zeitschrift für Physik B Condensed Matter **33**, 31 (1979).

[10] L. Balents, Nature **464**, 199 (2010).

[11] P. W. Anderson, Materials Research Bulletin **8**, 153 (1973).

[12] M. Hermele, M. P. A. Fisher, and L. Balents, Phys. Rev. B **69**, 064404 (2004).

[13] B. Normand, Contemporary Physics **50**, 533 (2009).

[14] R. Coldea, D. A. Tennant, and Z. Tylczynski, Phys. Rev. B **68**, 134424 (2003).

[15] L. Savary and L. Balents, Physical Review Letters **108**, 037202 (2012).

[16] D. J. Griffiths, *Introduction to electrodynamics* (Prentice Hall, New Jersey, 1999), Vol. 3.

[17] S. T. Bramwell, M. N. Field, M. J. Harris, and I. P. Parkin, Journal of Physics: Condensed Matter **12**, 483 (2000).

[18] L. Savary, K. A. Ross, B. D. Gaulin, J. P. C. Ruff, and L. Balents, Arxiv preprint arXiv:1204. 1320 (2012).

[19] M. E. Zhitomirsky, M. V. Gvozdikova, P. C. W. Holdsworth, and R. Moessner, Arxiv preprint arXiv:1204. 0595 (2012).

[20] J. D. M. Champion, A. S. Wills, T. Fennell, S. T. Bramwell, J. S. Gardner, and M. A. Green, Phys. Rev. B **64**, 140407 (2001).

[21] C. Castelnovo, R. Moessner, and S. L. Sondhi, Nature **451**, 42 (2008).

[22] J. S. Gardner, S. R. Dunsiger, B. D. Gaulin, M. J. P. Gingras, J. E. Greedan, R. F. Kiefl, M. D. Lumsden, W. A. MacFarlane, N. P. Raju, J. E. Sonier, I. Swainson, and Z. Tun, Phys. Rev. Lett. **82**, 1012 (1999).

[23] M. Gingras, B. Den Hertog, M. Faucher, J. Gardner, S. Dunsiger, L. Chang, B. Gaulin, N. Raju, and J. Greedan, Physical Review B **62**, 6496 (2000).

[24] B. Z. Malkin, A. R. Zakirov, M. N. Popova, S. A. Klimin, E. P. Chukalina, E. Antic-Fidancev, P. Goldner, P. Aschehoug, and G. Dhalenne, Phys. Rev. B **70**, 075112 (2004).

[25] H. R. Molavian and M. J. P. Gingras, Journal of Physics: Condensed Matter **21**, 172201 (2009).

[26] H. Blöte, R. Wielinga, and W. Huiskamp, Physica **43**, p. 549 (1969).

[27] J. Hodges, P. Bonville, A. Forget, M. Rams, K. Królas, and G. Dhalenne, Journal of Physics: Condensed Matter **13**, 9301 (2001).

[28] J. A. Hodges, P. Bonville, A. Forget, A. Yaouanc, P. Dalmas de Réotier, G. André, M. Rams, K. Królas, C. Ritter, P. C. M. Gubbens, C. T. Kaiser, P. J. C. King, and C. Baines, Phys. Rev. Lett. **88**, 077204 (2002).

[29] J. S. Gardner, G. Ehlers, N. Rosov, R. W. Erwin, and C. Petrovic, Phys. Rev. B **70**, 180404 (2004).

[30] Y. Yasui, M. Soda, S. Iikubo, M. Ito, M. Sato, N. Hamaguchi, T. Matsushita, N. Wada, T. Takeuchi, N. Aso, and K. Kakurai, Journal of the Physical Society of Japan **72**, 3014 (2003).

[31] P. Bonville, J. Hodges, E. Bertin, J. P. Bouchaud, P. Dalmas de Réotier, L. P. Regnault, H. Rønnow, J. P. Sanchez, S. Sosin, and A. Yaouanc, Hyperfine interactions **156**, 103 (2004).

[32] R. Applegate, N. R. Hayre, R. R. P. Singh, T. Lin, A. G. R. Day, and M. J. P. Gingras, Arxiv preprint arXiv:1203. 4569 (2012).

[33] H. Cao, A. Gukasov, I. Mirebeau, P. Bonville, C. Decorse, and G. Dhalenne, Phys. Rev. Lett. **103**, 056402 (2009).

[34] S. Onoda, **320**, 012065 (2011).

[35] J. D. Thompson, P. A. McClarty, H. M. Rønnow, L. P. Regnault, A. Sorge, and M. J. P. Gingras, Physical Review Letters **106**, 187202 (2011).

[36] L. J. Chang, S. Onoda, Y. Su, Y. J. Kao, K. D. Tsuei, Y. Yasui, K. Kakurai, and M. R. Lees, Arxiv preprint arXiv:1111. 5406 (2011).

[37] G. L. Squires, *Introduction to the Theory of Thermal Neutron Scattering* (Cambridge University Press, Cambridge, 1978).

[38] M. Blume, Physical Review **130**, 1670 (1963).

[39] S. B. Patel, *Nuclear physics: an introduction* (Anshan Ltd., Kent, 2011).

[40] J. S. Gardner, B. D. Gaulin, and D. M. Paul, Journal of Crystal Growth **191**, 740 (1998).

[41] S. M. Koohpayeh, D. Fort, and J. S. Abell, Progress in Crystal Growth and Characterization of Materials **54**, 121 (2008).

[42] D. Prabhakaran and A. T. Boothroyd, Journal of Crystal Growth **318**, 1053 (2011).

[43] A. Yaouanc, P. Dalmas de Réotier, C. Marin, and V. Glazkov, Phys. Rev. B **84**, 172408 (2011).

Chapter 2

Diffuse Magnetic Rod Scattering and the Discovery of a High-Field Phase in $Yb_2Ti_2O_7$

This chapter incorporates the article *"Two Dimensional Kagome Correlations and Field Induced Order in the Ferromagnetic XY Pyrochlore* $Yb_2Ti_2O_7$*"*, which has been published in Physical Review Letters. The full reference is given below:

K.A. Ross, J.P.C. Ruff, C.P. Adams, J.S. Gardner, H.A. Dabkowska, Y. Qiu, J.R.D. Copley, and B.D. Gaulin. Physical Review Letters, **103**, 227202 (2009).*

Figures 2.1, 2.2, 2.3 and 2.4 are reproduced from the above article with permission.

This chapter represents the first work performed on $Yb_2Ti_2O_7$ by Bruce Gaulin's research group. At the time of this study, there was controversy in the

---

literature regarding the nature of the ground state in $Yb_2Ti_2O_7$, as well as an intriguing preliminary measurement of the diffuse magnetic scattering which had revealed "rods" of scattering. Few details were known about this diffuse scattering. Our time-of-flight neutron scattering experiments performed at the Disk Chopper Spectrometer allowed us to comprehensively explore the magnetic diffuse scattering, and, for the first time, the inelastic scattering from $Yb_2Ti_2O_7$ in a variety of sample conditions. The response of $Yb_2Ti_2O_7$ to an applied magnetic field was first studied here, which revealed an ordered state with sharp spin wave excitations in fields greater than H=0.5T at T=30mK. We proposed a field vs. temperature phase diagram based on the collected results from the time-of-flight neutron scattering experiment as well as magnetization experiment performed at McMaster University.

2.1 Two Dimensional Kagome Correlations and Field Induced Order in the Ferromagnetic XY Pyrochlore $Yb_2Ti_2O_7$

K. A. Ross,[1] J.P.C. Ruff,[1] C.P. Adams,[1,2] J.S. Gardner,[3,4] H.A. Dabkowska,[1]
Y. Qiu,[4,5] J.R.D. Copley,[4] and B.D. Gaulin,[1,6]

[1] *Department of Physics and Astronomy, McMaster University, Hamilton, Ontario, L8S 4M1, Canada*
[2] *Department of Physics, St. Francis Xavier University, Antigonish, Nova Scotia, B2G 2W5, Canada*
[3] *Indiana University, 2401 Milo B. Sampson Lane, Bloomington, Indiana 47408, USA*
[4] *National Institute of Standards and Technology, 100 Bureau Drive, MS 6102, Gaithersburg, Maryland 20899-6102, USA*
[5] *Department of Materials Science and Engineering, University of Maryland, College Park, Maryland 20742, USA*
[6] *Canadian Institute for Advanced Research, 180 Dundas St. W., Toronto, Ontario, M5G 1Z8, Canada*

Abstract

Neutron scattering measurements show the ferromagnetic XY pyrochlore $Yb_2Ti_2O_7$ to display strong quasi-two dimensional (2D) spin correlations at low temperature, which give way to long range order (LRO) under the application of modest magnetic fields. Rods of scattering along $< 111 >$ directions due to these 2D spin correlations imply a magnetic decomposition of the cubic pyrochlore system into decoupled kagome planes. A magnetic field of ~ 0.5 T applied along the $[1\bar{1}0]$ direction induces a transition to a 3D LRO state characterized by long-lived, dispersive spin waves. Our measurements map out a complex low temperature-field phase diagram for this exotic pyrochlore magnet.

Magnetic materials displaying the pyrochlore structure are of intense current interest due to their varied and often unconventional magnetic ground states. In such materials the magnetic ions form an array of corner-sharing tetrahedra referred to as the pyrochlore lattice, which is illustrated in Fig. 2.1. This lattice is the 3D archetype for geometric frustration; magnetic moments residing on it cannot simultaneously satisfy all local interactions due to geometrical constraints, leading to a macroscopic degeneracy of the ground state [1]. This frustration underlies a range of exotic disordered magnetic states at low temperatures, such as spin liquid, spin ice, and spin glass states [2, 3, 4, 5]. Many rare-earth-titanates with chemical composition $R_2\mathrm{Ti}_2\mathrm{O}_7$ crystalize as pyrochlores with the cubic space group $\mathrm{Fd\bar{3}m}$. The diverse magnetic behavior of these isostructural insulators arises from an interplay between the moment size, exchange interactions, and single-ion anisotropy resulting from crystalline electric field effects. These often-competing interactions make these materials fertile ground for the generation of novel magnetic ground states.

Several model pyrochlore magnets have been well studied theoretically, and such studies are important benchmarks for understanding the nature of the exotic low temperature magnetic states. For example, isotropic Heisenberg spins interacting with simple near-neighbor antiferromagnetic interactions on the pyrochlore lattice possess a disordered spin liquid ground state [6, 7]. Near-neighbour ferromagnetically-coupled spins with hard, local [111] anisotropy, such that magnetic moments point either directly into or out of the individual tetrahedra, display the disordered spin ice state at low temperatures [8].

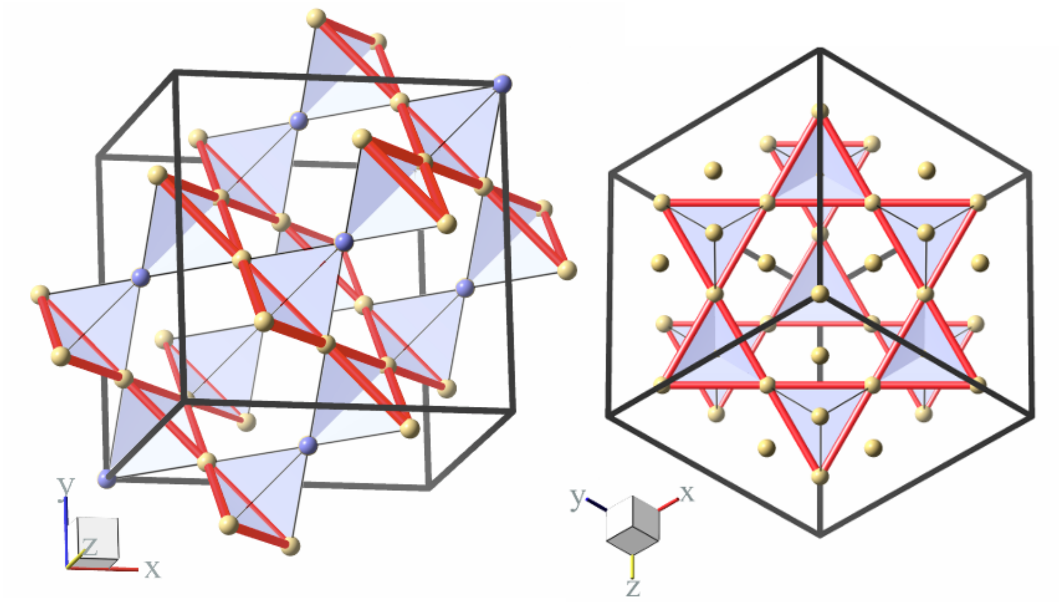

Figure 2.1: (color online) Left: The cubic pyrochlore lattice, showing the positions of magnetic Yb^{3+} ions. This structure can be decomposed into alternating triangular (blue or dark atoms) and kagome planes (gold or light atoms), along the $< 111 >$ directions. The bonds within the kagome planes are shown in red (dark) lines. Right: a view along [111] shows the structure of the kagome planes.

In $Yb_2Ti_2O_7$, the effective spin-1/2 Yb^{3+} moments exhibit overall ferromagnetic (FM) interactions, with a θ_{CW} of between +0.49K and +0.75K [9, 10], as well as easy plane anisotropy *perpendicular* to the local [111] direction [11]. $Yb_2Ti_2O_7$ is the only known example of a ferromagnetic XY pyrochlore, and therefore is an important experimental benchmark in the field. Intriguingly, one is not immediately lead to suspect that geometric frustration is central to the low temperature magnetic behavior of this material. Unlike the ferromagnetic Ising-like case mentioned above, the ferromagnetic XY pyrochlore is expected to have a *non-degenerate* classical ground state. Nevertheless, in this Letter we show that a disordered state is maintained in $Yb_2Ti_2O_7$ to temperatures well below both θ_{CW} and the nominal T$_C$ for this system. We further demonstrate the ease with which a small perturbation, specifically the application of a $[1\bar{1}0]$ magnetic field, can drive this system to stable long range magnetic order (LRO). Both of these phenomena are hallmarks of geometrical frustration. Emergent frustration in a quantum system not expected to be frustrated classically has previously been discussed in relation to other rare-earth-metal titanates [12]. Indeed, the spin-liquid state of $Tb_2Ti_2O_7$ is known to resist LRO to temperatures at least three orders of magnitude lower than the characteristic Curie-Weiss constant [2], despite being approximated by a classical $< 111 >$ Ising antiferromagnet model with a unique ground state [13].

A previous study of $Yb_2Ti_2O_7$ has revealed a sharp specific heat anomaly near T$_C$ $\sim$ 240mK [14]. Yasui *et al* presented single crystal elastic neutron scattering results that indicate simple, collinear FM ordering below T$_C$ [15]. However, this type of ordering is inconsistent with the results of a polarized neutron scattering study [16]. Additionally, powder neutron diffraction measurements by Hodges *et al* indicate no obvious signs of long range order below T$_C$ [11]. Using Mössbauer and μSR techniques, this group instead argued that the nature of the transition is comparable to that of a gas-liquid system, in that the fluctuation rate of the $\sim 3\mu_\mathrm{B}$ Yb^{3+} moments drops by up to two orders of magnitude at T$_C$, but does not vanish [11]. Most intriguingly, a single crystal neutron diffraction measurement of $Yb_2Ti_2O_7$ revealed "rods" of diffuse magnetic scattering along the [111] direction of reciprocal space [17]. These rods indicate an unexpected 2D correlated spin state that is present both above and below T$_C$.

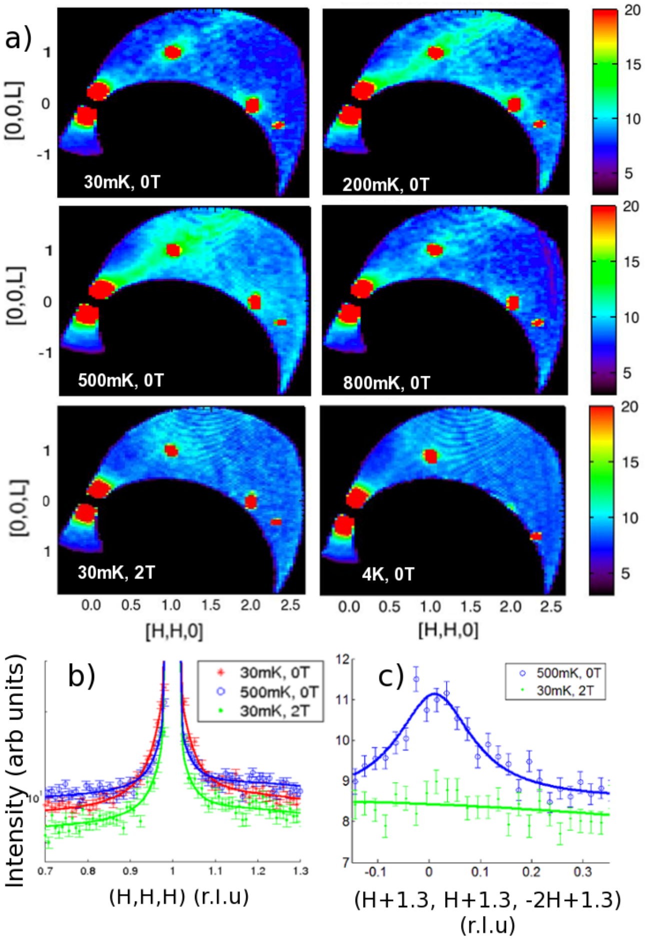

Figure 2.2: (color online)a) Color contour maps of elastic neutron scattering in the HHL plane. In zero applied field, diffuse rods of scattering that extend along the [111] direction are visible at 800mK and below. The diffuse scattering in applied field (30mK, 2T) is similar to the disordered state (4K, 0T). b) Cuts of the scattering along the rod direction show the evolution of this 2D scattering with temperature and field. c) Cuts perpendicular to the rod direction at 500mK, 0T, and within the field-induced LRO state at 30mK, 2T.

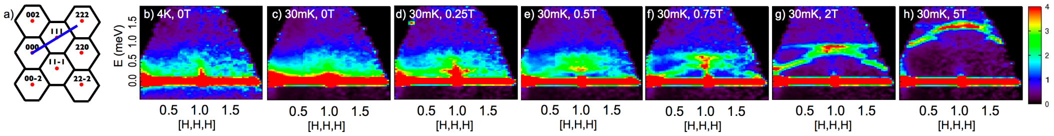

Figure 2.3: (color online) Color contour maps of the inelastic neutron scattering along the [HHH] direction. The data is binned in [H,H,-2H] over the range [-0.1,0.1]. Panel a) is a schematic of the nuclear zones in the HHL plane, and the blue line shows the direction of the cut in the inelastic panels. Panels b) through d) show the absence of well defined spin excitations in low field, even at 30mK (panel c and d). Resolution-limited spin waves appear at all wavevectors upon application of a magnetic field greater than ~ 0.5T (panels e through h), indicating a LRO state.

A single crystal of $Yb_2Ti_2O_7$ was prepared at McMaster University using a two-mirror floating zone image furnace. It was grown in 4 bars of oxygen, at a rate of 5 mm/h, and the growth procedure closely resembled that reported previously for other rare earth titanates [18]. Recently, a single crystal of $Y_2Ti_2O_7$ prepared in this manner has been shown to have an exceptionally long phonon mean-free-path (10μm at 2K), indicative of the very high quality of these crystals [19]. The ~7 gram single crystal of $Yb_2Ti_2O_7$ was mounted in a vertical field dilution refrigerator cryomagnet with its (HHL) plane coincident with the horizontal plane. Time-of-flight neutron scattering measurements were performed using the Disk Chopper Spectrometer at the NIST Center for Neutron Research[20]. Measurements were performed using 5 Å incident neutrons, allowing us to map out the pattern of diffuse scattering in the (HHL) plane as a function of temperature and magnetic field, as well as to investigate inelastic scattering with an approximate energy resolution of ~ 0.09 meV.

In zero magnetic field, elastic scattering at low temperatures within the (HHL) plane confirms the presence of rods of magnetic diffuse scattering along the [111] direction (Fig. 2.2a), indicating 2D magnetic correlations in planes perpendicular to this direction. The rods are visible at 800mK and become more clearly defined as the temperature is lowered to 200mK. At the lowest measured temperature, 30mK, the diffuse scattering remains extended along [111], but intensity has accumulated around the (111) Bragg peak (Fig. 2.2b). This indicates that 3D interplane correlations have developed at 30mK, although these are short range.

The 3D cubic pyrochlore lattice can be naturally decomposed along $< 111 >$ into interleaved kagome and triangular planes, and we argue that the 2D spin correlations form within the kagome planes (Fig. 2.1). This is in view of the fact that the exchange interactions are expected to be stronger between moments within the kagome rather than the triangular planes, due to their 1st, rather than 3rd near-neighbor separation. The question of what prevents the correlations from extending between the kagome planes is puzzling in light of the underlying cubic symmetry of the lattice, which requires that the interactions between each neighboring spin be equivalent. Nonetheless, we conclude that only three of four spins per tetrahedron are correlated to a significant degree above $\sim$ 200mK.

This recalls the frustrated antiferromagnetic spinel $Li_2Mn_2O_4$, whose magnetic pyrochlore sublattice also decouples into kagome planes at a range of temperatures above the Néel temperature [21, 22]. However, in the case of $Li_2Mn_2O_4$ the lattice is known to be tetragonally distorted, whereas no evidence for a departure from cubic symmetry has been reported for $Yb_2Ti_2O_7$. We note that the diffuse rods of magnetic scattering in $Yb_2Ti_2O_7$ appear along all measured < 111 > directions, consistent with either a spatially (domain) or temporally averaged magnetic structure. Temporal fluctuations would require the rods be dynamic in nature, as will be shown to be the case.

Related to modifications of the rods of diffuse scattering upon cooling from 500mK to 30mK, we observe a small increase (∼3%) in the total intensity of the (111) Bragg peak, in qualitative agreement with earlier studies[15, 16]. This increase does not correspond to a fully ordered state; rather, it results from the diffuse rods of scattering coalescing around Bragg peaks, an effect that is illustrated by cuts along the rods, shown in Fig. 2b). A similar broad feature is observed at ($\bar{1}\bar{1}\bar{3}$), producing a ∼2% increase in intensity at this peak. The observed increase of scattering near the base of these Bragg peaks at 30mK indicates a developing short range ordered 3D magnetic state. Aside from the increase of diffuse scattering at (111) and ($\bar{1}\bar{1}\bar{3}$), no other changes in Bragg intensities were observed upon cooling from 500mK, measured out to $Q = 2.34$ Å^{-1}. This is in disagreement with the increase in (222) Bragg scattering on cooling from 300mK reported by Yasui *et al* , and we note that like the polarized neutron work [16], our result is inconsistent with the LRO simple collinear FM state proposed therein [15].

Application of even a weak magnetic field along [$1\bar{1}0$] dramatically alters the low temperature magnetic state. Strikingly, sharp spin waves are evident at all wavevectors in the inelastic neutron scattering (INS) spectrum for magnetic fields as low as 0.75T (Fig. 2.3 f). Meanwhile, the diffuse rods of scattering are eliminated. These results demonstrate that a magnetic LRO state is induced by the application of a [$1\bar{1}0$] magnetic field. Such perturbation-induced order is also observed in other magnetic pyrochlore systems; $Tb_2Ti_2O_7$ can be driven from a spin liquid to a LRO state upon application of a $[1\bar{1}0]$ magnetic field [23], as well as as by combinations of uniaxial and hydrostatic pressure and magnetic fields [24, 25].

The evolution of the inelastic scattering with the $[1\bar{1}0]$ applied field is shown in Fig. 2.3. The spectrum is displayed along [HHH], which coincides with the direction of the rods in the low temperature, low field state. At μ_0H=0T, T=4K (panel b), diffuse, quasi-elastic (QE) scattering extends in energy to 0.6meV. The QE scattering is most intense along the rod direction, indicating that weak, dynamic rods are present at 4K in zero field. On cooling to 30mK, the intensity of the QE scattering increases, but its energy scale remains constant. The corresponding fluctuation rate, $\sim$ 145 GHz, is much higher than that reported by Hodges *et al* in their μSR study [11]. It also shows no temperature dependence in contrast to the first order-like transition they reported. The differences between this and the present study suggest two energy scales characterizing the spin fluctuations, which are accessible individually by the μSR and INS techniques. The energy scale reported here is exclusive to the rods of scattering, and hence to the short range correlations.

Notably, no spin wave modes appear in the low temperature zero-field state, which is consistent with short ranged, 3D correlations, as opposed to a LRO state which would support spin wave excitations. At μ_0H=0.25T, T=30mK, the QE rod of scattering lifts off from the elastic channel, and at μ_0H=0.5T a dispersion of this excitation into spin wave modes is observed (panel d and e). In stronger applied fields, the spin waves are increasingly gapped by the

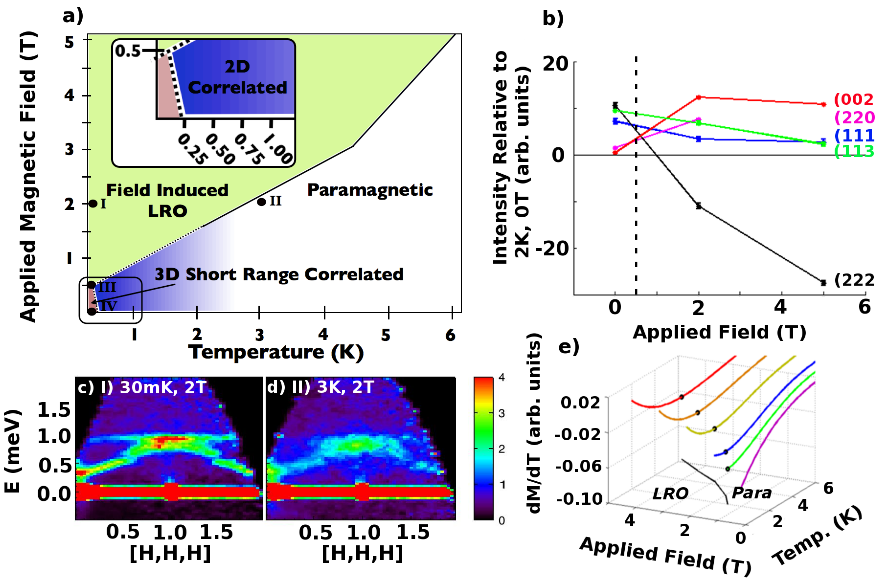

Figure 2.4: (color online) a) Phase diagram for $Yb_2Ti_2O_7$. At 30mK, the transition to LRO is indicated near 0.5T (inset), which is evinced by inelastic neutron data at points III and IV (shown in Fig. 2.3c and e). b) Changes in elastic Bragg scattering as a function of field at 30mK. c) and d) Inelastic neutron scattering data at points I and II confirm the phase boundary, which is measured from magnetization data (panel e) above T=2K.

Zeeman energy and become nearly resolution-limited, having a full width of approximately 0.1meV at 2T, 30mK (panel g). Three spin wave branches are observed in this field-induced state; one with little or no dispersion while the other two exhibit minima tending to zero energy (i.e. Goldstone modes) at the (111) and (222) positions. We argue that these dispersive modes are indicative of a LRO state on the basis that they are resolution-limited at all wavevectors, particularly at the magnetic zone centers where this quality indicates a large correlation length to the long wavelength dynamics. The presence of two types of branches, one dispersionless and the other Goldstone-like, may be associated with fluctuations out-of and within the easy XY plane, respectively. Indeed, a related spin wave spectrum is observed for the XY AF pyrochlore $Er_2Ti_2O_7$ [26]. In $Yb_2Ti_2O_7$, the magnetic zones are well-defined and coincident with the nuclear zones, as indicated by clear gapping of the dispersive branches at the nuclear zone boundaries. We therefore identify μ_0H∼0.5T at T=30mK as a transition to a long ranged ordered magnetic state, and note that the coincidence of magnetic and nuclear Bragg peaks presents a challenge for the determination of the LRO structure.

Taking well-defined spin waves at all wavevectors as a defining characteristic of the field-induced LRO state, we propose the phase diagram for $Yb_2Ti_2O_7$ shown in Fig. 2.4a). To further characterize the phase diagram, magnetization measurements were performed on a small single crystal of $Yb_2Ti_2O_7$ using a SQUID magnetometer with the field aligned along $[1\bar{1}0]$. A minimum is observed in dM/dT(T), which we have mapped as a function of field (Fig. 2.4e) for temperatures of 2K and above. The resulting phase boundary is consistent with our spin wave measurements, in particular with the spin wave spectrum at points I and II, shown in Fig. 2.4c) and d), which are characteristic of the LRO state and nearly paramagnetic state, respectively.

The changes in the elastic Bragg scattering with field at T=30mK, shown in Fig. 2.4b), merit comment. Subtraction of nuclear Bragg intensities (from the 2K, 0T set) reveals that the change in (222) intensity as the field is increased past H_C, while a robust result, is anomalous since the intensity falls below the purely nuclear scattering level. This could indicate a magnetically driven structural distortion of the lattice, which necessarily hinders the determination of the magnetic structure based on these intensity changes.

In conclusion, $Yb_2Ti_2O_7$ exhibits spontaneous 2D correlations at low temperature, which emerge via unknown mechanisms from a seemingly isotropic cubic lattice. The previously reported transition in fluctuation rate at $\sim$240mK involves a crossover from this 2D correlated state to a short-ranged 3D correlated state. Application of a small magnetic field relieves the frustration and induces long range magnetic order. Upon entering the ordered state, anomalous changes in Bragg scattering indicate the possibility of magneto-elastic coupling in $Yb_2Ti_2O_7$, which may ultimately underlie the emergent planar spin correlations in zero field.

The authors would like to acknowledge M.J.P.Gingras, J.P. Clancy and G. MacDougall for useful discussions, as well as P. Dube for technical assistance. We acknowledge the use of the DAVE software package. This work utilized facilities supported in part by the National Science Foundation under Agreement No. DMR-0454672, and was supported by NSERC of Canada.

2.2 * References

[1] H. T. Diep, *Magnetic Systems with Competing Interactions: Frustrated Spin Systems* (World Scientific, Singapore, 1994).

[2] J. S. Gardner, S. R. Dunsiger, B. D. Gaulin, *et al.*, Phys. Rev. Lett. **82**, 1012 (1999).

[3] J. S. Gardner, A. Keren, G. Ehlers, *et al.*, Phys. Rev. B **68**, 180401 (2003).

[4] S. T. Bramwell, M. J. Harris, B. C. den Hertog, *et al.*, Phys. Rev. Lett. **87**, 047205 (2001).

[5] B. D. Gaulin, J. N. Reimers, T. E. Mason, *et al.*, Phys. Rev. Lett. **69**, 3244 (1992).

[6] R. Moessner and J. T. Chalker, Phys. Rev. Lett. **80**, 2929 (1998).

[7] B. Canals and C. Lacroix, Phys. Rev. Lett. **80**, 2933 (1998).

[8] S. T. Bramwell and M. J. P. Gingras, Science **294**, 1495 (2001).

[9] S. T. Bramwell, M. N. Field, M. J. Harris, *et al.*, J. Phys.: Condens. Matter **12**, 483 (2000).

[10] J. A. Hodges, P. Bonville, A. Forget, *et al.*, J. Phys.: Condens. Matter **13**, 9301 (2001).

[11] J. A. Hodges, P. Bonville, A. Forget, *et al.*, Phys. Rev. Lett. **88**, 77204 (2002).

[12] H. R. Molavian, M. J. P. Gingras, and B. Canals, Phys. Rev. Lett. **98**, 157204 (2007).

[13] M. Enjalran, M. J. P. Gingras, Y. J. Kao, *et al.*, J. Phys.: Condens. Matter **16**, S673 (2004).

[14] H. W. J. Blöte, R. F. Wielinga, and W. J. Huiskamp, Physica **43**, p.549 (1969).

[15] Y. Yasui, M. Soda, S. Iikubo, *et al.*, J. Phys. Soc. Jpn. **72**, 3014 (2003).

[16] J. S. Gardner, G. Ehlers, N. Rosov, *et al.*, Phys. Rev. B **70**, 180404 (2004).

[17] P. Bonville, J. A. Hodges, E. Bertin, *et al.*, Hyperfine Interactions **156**, 103 (2004).

[18] J. S. Gardner, B. D. Gaulin, and D. M. Paul, Journal of Crystal Growth **191**, 740 (1998).

[19] M. B. Johnson, D. D. James, A. Bourque, *et al.*, Journal of Solid State Chemistry **182**, 725 (2009).

[20] J. R. D. Copley and J. C. Cook, Chemical Physics **292**, 477 (2003).

[21] C. R. Wiebe, P. L. Russo, A. T. Savici, *et al.*, J. Phys.: Condens. Matter **17**, 6469 (2005).

[22] A. S. Wills, N. P. Raju, C. Morin, *et al.*, Chem. Mater. **11**, 1936 (1999).

[23] K. C. Rule, J. P. C. Ruff, B. D. Gaulin, *et al.*, Phys. Rev. Lett. **96**, 177201 (2006).

[24] I. Mirebeau, I. N. Goncharenko, G. Dhalenne, *et al.*, Phys. Rev. Lett. **93**, 187204 (2004).

[25] I. Mirebeau, I. N. Goncharenko, P. Cadavez-Peres, *et al.*, Nature **420**, 54 (2002).

[26] J. P. C. Ruff, J. P. Clancy, A. Bourque, *et al.*, Phys. Rev. Lett. **101**, 147205 (2008).

Chapter 3

Investigation of the Significance of the Low Temperature Specific Heat Anomaly

This chapter incorporates the article *"Dimensional Evolution of Spin Correlations in the Magnetic Pyrochlore $Yb_2Ti_2O_7$"*, which has been published in Physical Review B. The full reference is given below:

K.A. Ross, L.R. Yaraskavitch, M. Laver, J.S. Gardner, J.A. Quilliam, S. Meng, J.B. Kycia, D.K. Singh, Th. Proffen, H.A. Dabkowska, and B.D. Gaulin. Physical Review B, **84**, 174442 (2011). [*]

Figures 3.1, 3.2, 3.3, 3.4, 3.5, and 3.6 are reproduced from said article with permission.

The neutron scattering experiment presented in this chapter was designed to reveal the temperature dependence, at zero applied magnetic field, of the magnetic diffuse scattering in $Yb_2Ti_2O_7$. From the previous chapter, it is clear

---

[*] ©(2011)The American Physical Society

that the magnetic diffuse scattering undergoes a qualitative change at temperatures between 500mK and 30mK, and a logical assumption could be that this change occurs at the temperature of the specific heat anomaly, 240mK. We quantified the temperature dependence of the change in diffuse scattering using a triple-axis-spectrometer, which allowed us to efficiently collect data at two $\vec{Q}$ points along the rods of scattering. The temperature dependence held a surprise, which was that the change occured gradually, starting at a higher temperature than expected (400mK). Upon searching for signals of this dimensional crossover at 400mK in the low-temperature specific heat, Jan Kycia and his group (most notably Jeff Quilliam and Luke Yaraskavitch) found a startling result; the temperature and sharpness of the specific heat anomaly varied between samples, indicating underlying structural defects in some samples of $Yb_2Ti_2O_7$. This paper contributed to the understanding of $Yb_2Ti_2O_7$ in two ways. First, it confirmed and quantified the dimensional evolution of the spin correlations from a 2D state to a very short range 3D correlated state at 400mK in a single crystal of $Yb_2Ti_2O_7$. Second, it revealed a sample-dependence issue which is likely behind the controversy surrounding the nature of the ground state of $Yb_2Ti_2O_7$. Following the presentation of this paper at the APS March Meeting in 2011[†], two other groups (Yaouanc 2011 and Chang 2011) reported the sample-dependence of the low-temperature specific heat in $Yb_2Ti_2O_7$, indicating that this is a prevalent issue worldwide, particularly in the single crystals.

[†] Kate Ross, APS March Meeting 2011, http://meetings.aps.org/link/BAPS.2011.MAR.A18.1

3.1 Dimensional Evolution of Spin Correlations in the Magnetic Pyrochlore $Yb_2Ti_2O_7$

K. A. Ross,[1] L.R. Yaraskavitch,[2,3] M. Laver,[4,5,6] J.S. Gardner,[7,8] J.A. Quilliam,[2,3] S. Meng,[2,3] J.B. Kycia,[2,3] D.K. Singh,[8,9] Th. Proffen,[10,11] H.A. Dabkowska,[12] and B.D. Gaulin,[1,12,13]

[1] *Department of Physics and Astronomy, McMaster University, Hamilton, Ontario, L8S 4M1, Canada*

[2] *Department of Physics and Astronomy and Guelph-Waterloo Physics Institute, University of Waterloo, Waterloo, ON, N2L 3G1, Canada*

[3] *Institute for Quantum Computing, University of Waterloo, Waterloo, ON, N2L 3G1, Canada*

[4] *Materials Research Division, Risö DTU, Technical University of Denmark, DK-4000 Roskilde, Denmark*

[5] *Nano-Science Center, Niels Bohr Institute, University of Copenhagen, DK-2100 Köbenhavn, Denmark*

[6] *Laboratory for Neutron Scattering, Paul Scherrer Institut, 5232 Villigen PSI, Switzerland*

[7] *Indiana University, 2401 Milo B. Sampson Lane, Bloomington, Indiana 47408, USA*

[8] *National Institute of Standards and Technology, 100 Bureau Drive, MS 6102, Gaithersburg, Maryland 20899-6102, USA*

[9] *Dept. of Materials Science and Engineering, University of Maryland, College Park, MD 20742*

[10] *Los Alamos National Laboratory, Los Alamos, New Mexico 87545, USA*

[11] *Spallation Neutron Source, Experimental Facilities Division, Oak Ridge National Laboratory, P.O. Box 2008, Oak Ridge, TN 37831, USA*

[12] *Brockhouse Institute for Materials Research, McMaster University, Hamilton, Ontario, L8S 4M1, Canada*

[13] *Canadian Institute for Advanced Research, 180 Dundas St. W.,Toronto, Ontario, M5G 1Z8, Canada*

Abstract

The pyrochlore material $Yb_2Ti_2O_7$ displays unexpected quasi-two-dimensional (2D) magnetic correlations within a cubic lattice environment at low temperatures, before entering an exotic disordered ground state below T=265mK. We report neutron scattering measurements of the thermal evolution of the

2D spin correlations in space and time. Short range three dimensional (3D) spin correlations develop below 400 mK, accompanied by a suppression in the quasi-elastic (QE) scattering below ~ 0.2 meV. These show a slowly fluctuating ground state with spins correlated over short distances within a kagome-triangular-kagome (KTK) stack along [111], which evolves to isolated kagome spin-stars at higher temperatures. Furthermore, low-temperature specific heat results indicate a sample dependence to the putative transition temperature that is bounded by 265mK, which we discuss in the context of recent mean field theoretical analysis.

3.1.1 Introduction

The corner-sharing tetrahedral geometry of the pyrochlore lattice favors strong *geometric frustration*, wherein a competition of exchange interactions between localized magnetic moments results directly from their arrangement within the lattice. This phenomenon tends to suppress transitions to magnetic long range order (LRO), leaving in their place unusual short-range magnetic correlations at low temperatures. The form of such correlations varies between frustrated systems, with ground states typically determined by subleading terms in the relevant Hamiltonian, such as dipole interactions, further neighbor exchange, and structural distortions within the underlying crystal lattice.[1,2] The rare earth titanate series of materials, which have the chemical formula $R_2\mathrm{Ti}_2\mathrm{O}_7$ with R being a trivalent magnetic rare earth ion, crystallize into the face centered cubic (fcc) space group Fd$\bar{3}$m which characterizes the pyrochlore lattice. This series provides excellent examples of the variety of exotic ground states that can emerge in nearly identical chemical environments when geometric frustration is at play. Several of the rare earth titanates exhibit disordered ground states which persist down to 30mK, namely the spin ices $\mathrm{Dy}_2\mathrm{Ti}_2\mathrm{O}_7$ and $\mathrm{Ho}_2\mathrm{Ti}_2\mathrm{O}_7$,[3,4,5] and the enigmatic spin liquid $\mathrm{Tb}_2\mathrm{Ti}_2\mathrm{O}_7$.[6,7] Others in the series do order magnetically, such as $\mathrm{Gd}_2\mathrm{Ti}_2\mathrm{O}_7$[8,9,10] and $\mathrm{Er}_2\mathrm{Ti}_2\mathrm{O}_7$,[11,12] but the nature of the ordering is unusual in both cases. In all of these cases, the source of the frustration (or lack thereof) is well-understood in terms of the spin interactions and the single-ion anisotropy imposed by the crystal electric field. In particular, the spin ices combine effective ferromagnetic (FM) exchange with strong Ising-like anisotropy, such that the moments are constrained to point into or out of each tetrahedron.

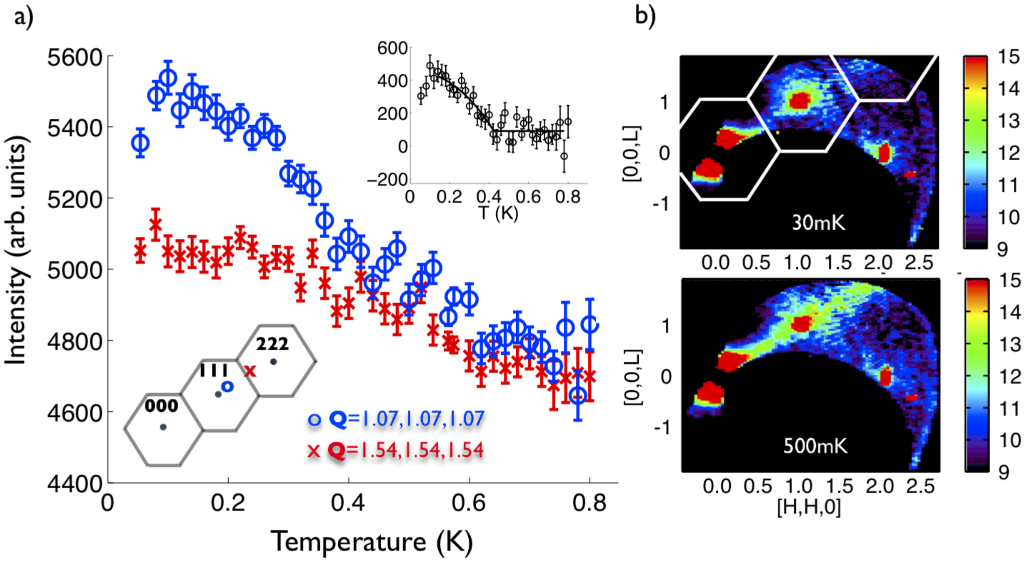

Figure 3.1: (color online) a) The temperature dependence of neutron scattering intensity at two $\mathbf{Q}$ points that lie on the rod of scattering, $\mathbf{Q}_{1.54}$ (red x's) and $\mathbf{Q}_{1.07}$ (blue o's) (10K background subtracted). Bottom Inset: the position of the two $\mathbf{Q}$ points is shown relative to the fcc Brillouin zone boundaries in the (HHL) plane. Top Inset: the difference of intensities, $I_{1.07}$ - $I_{1.54}$, with the solid line as a guide to the eye. b) Elastic time-of-flight neutron scattering data at 30mK and 500mK (reproduced from Ref. 13). Error bars represent $\pm\ 1\sigma$.

$Yb_2Ti_2O_7$ provides an intriguing contrast to the spin ices. It is known to combine FM exchange ($\theta_{CW}\sim$600mK to 800mK[14,15]) with XY anisotropy.[16,17,18] The continuous degree of freedom provided by the XY anisotropy leads one to naively expect an ordered FM ground state. However, despite what appears to be a transition near 200mK,[19,16,20] most experimental evidence suggests that $Yb_2Ti_2O_7$ displays a disordered ground state down to 30mK in zero-magnetic field.[13,16] Application of a modest magnetic field along [110] at 30 mK induces a transition to a polarized, ordered phase with well defined spin wave excitations.[13] Using anisotropic exchange Hamiltonians, recent theoretical studies have sought to understand the spin wave dispersions in the magnetic field induced ordered state,[21] as well as the diffuse scattering at relatively high temperatures in zero field[22] and the local spin susceptibility.[18,23] Interestingly, some of these studies indicate that the dominant exchange interaction is the Ising component, which may explain the lack of simple FM behaviour in $Yb_2Ti_2O_7$, making it an *exchange* analog to the spin ices.[21,18]

An early heat capacity (C_p) measurement showed an anomaly at T=214mK, indicating a possible phase transition, in addition to a broad Schottky-like hump at 2K.[19] The putative transition, whose temperature varies somewhat in the literature and which we henceforth label T_c, has previously been explored through several techniques.[16,24,25,13] Much of this characterization is consistent with the absence of conventional LRO below T_c, although single crystal neutron diffraction and AC susceptibility results presented in Ref. 25, suggest a collinear FM ground state. Hodges *et al* found a discontinuous change in the spin fluctuation frequency at T_c=240mK as measured by Mössbauer and μSR, along with an absence of magnetic Bragg peaks in neutron powder diffraction.[16] The specific heat of the sample used in Ref. 16 was found to display a sharp anomaly at 250mK,[20] close to the observed first order drop in the spin fluctuation rate. Single crystal neutron scattering studies revealed a pattern of diffuse scattering, notably taking the form of *rods* of scattering along the <111> directions, with a characteristic QE energy scale of 0.3meV.[13,26] This diffuse scattering, which indicates short range spin correlations, is present both above and below T_c, but a qualitative difference was observed between 500mK and 30mK that indicated short-range 3D spin correlations at the lowest temperatures.[13] The observed change was that the rod of scattering became more strongly peaked near the (111) zone center, moving from a featureless rod at 500mK to a rod with structure at 30mK. The conventional interpretation of a *flat* rod of scattering in any diffraction pattern is the presence of 2D correlations. Though the rod of scattering is flat at 500mK, this interpretation is striking in the present case, as it implies a magnetic decomposition of the 3D pyrochlore structure into a stacking of alternating kagome and triangular planes along <111>, breaking the underlying cubic symmetry.

It should be noted that in Ref. 22, where exchange parameters were extracted by fitting a modified measurement of the diffuse scattering pattern in the HHL plane at 1.4K , the real space spin correlations derived from these parameters were reported to show a more nuanced anisotropic behavior. However, their calculated spin correlation functions display some decoupling of the kagome planes with pronounced correlations along near neighbor [110] directions.

The nature of the transition near 200mK, and the resulting ground state of $Yb_2Ti_2O_7$, remains a matter of debate. Most of the experimental studies indicate a disordered ground state. This is supported by a recent theoretical study[21] that makes use of the measured high-field spin wave spectrum to determine microscopic exchange parameters. The parameters are highly anisotropic, favoring a local <111> exchange. From a mean field perspective, these parameters predict an ordered ferromagnetic state below 3.2K. Frustration and quantum fluctuations therefore must be responsible for suppressing a transition to long range FM order, possibly to zero temperature. Furthermore, the extracted exchange parameters may place $Yb_2Ti_2O_7$ within the non-magnetic spin liquid ground state studied by Refs. 27 and 28. In this scenario, the zero-field QE diffuse scattering measured at 30mK in the most recent single crystal work, Ref. 13, would represent two-spinon-type magnetic excitations.

Contrary to this scenario, the work of Yasui *et al* indicates an ordered, collinear FM ground state below 250mK, albeit possibly a glassy one with a very long relaxation time.[25] In light of the results to be described in the present report, which identify a prevalent sample dependence to the temperature and sharpness of the specific heat anomaly at "T_c", this FM ordering remains a possibility for the true ground state of $Yb_2Ti_2O_7$. However, we will show that the sample dependence of the C_p anomaly is seemingly irrelevant to the changes in energy-integrated diffuse scattering, which occur at a temperature that does not coincide with any specific heat anomaly. Furthermore, the spread of T_c in various samples is quite small compared to the overall suppression from the predicted mean field transition temperature, lending further support to the idea of a low temperature state dominated by quantum fluctuations.

This paper details the temperature dependence of the aforementioned changes in diffuse magnetic scattering in zero-field, and determines the extent to which they correlate to features in the specific heat. Further, through specific heat measurements on various samples of $Yb_2Ti_2O_7$, we reveal evidence for sample dependence in both single-crystalline and powder samples, which we posit affects all samples reported on in the literature to date. Through neutron powder diffraction and Rietveld analysis, we show that the sample-dependence is not due to an obvious structural distortion, but rather to small levels of random disorder or strain within an average ordered structure.

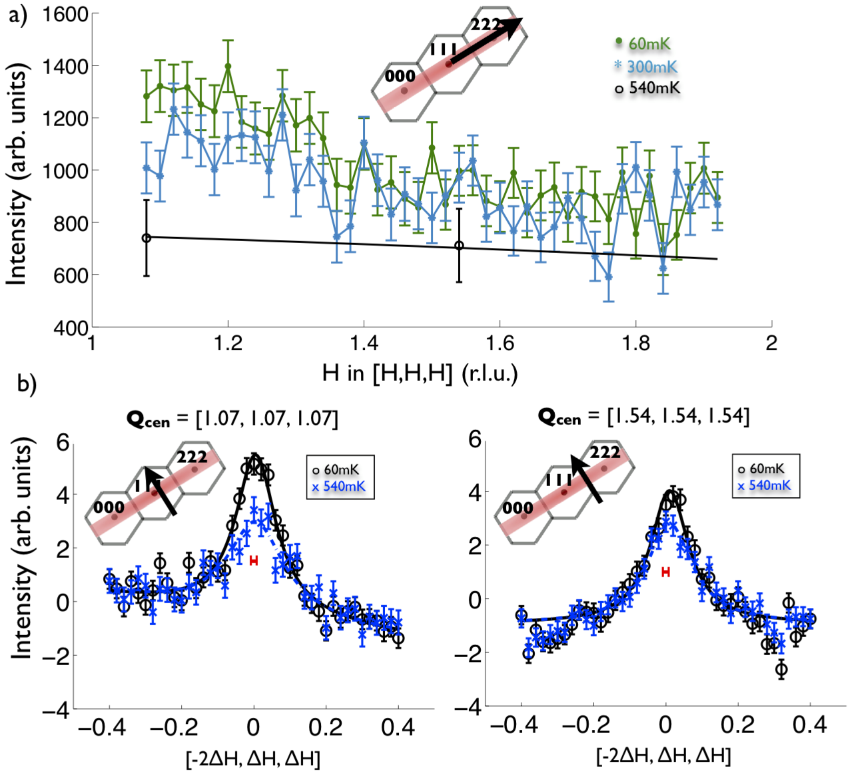

Figure 3.2: a) (10K background subtracted) Longitudinal rod scans at T = 60 mK and 300 mK. Data points at 540mK are consistent with a **Q** dependence that follows the Yb^{3+} magnetic form factor (black solid line). b) Examples of transverse scans across the rod, centered at $\mathbf{Q}_{1.07}$ and $\mathbf{Q}_{1.54}$. The insets show the positions of the scans in reciprocal space.

3.1.2 Experimental Method

Single crystalline $Yb_2Ti_2O_7$ was prepared at McMaster University using a two-mirror floating zone image furnace. It was grown in 4 atm of oxygen, at a rate of 5 mm/h, the growth procedure resembling Ref. 29. The single crystal that was the subject of these neutron measurements was the same one studied previously[13]. The specific heat measurements were performed on this and one other crystal prepared under identical conditions. The starting material for these growths, a pressed polycrystalline sample, was prepared by mixing Yb_2O_3 and TiO_2 in stoichiometric ratio and annealing at 1200°C for 24 hours, with a warming and cooling rate of 100°C/h. The specific heat of this polycrystalline material was measured for comparison to the single crystals.

Single crystal time-of-flight neutron scattering measurements were carried out using the Disk Chopper Spectrometer at the National Institute of Standards and Technology (NIST), with 5Å incident neutrons, giving an energy resolution of 0.09meV. Triple-axis neutron scattering experiments were also performed at NIST, using SPINS. For the triple-axis measurements, a pyrolytic graphite (PG) monochromator provided an incident energy of 5meV, and an energy resolution of $\sim \delta E = 0.25$meV. Elastically scattered neutrons were selected using five flat PG analyzer blades. Due to the aforementioned energy resolution, the nominal elastic scattering in fact integrates over much of the quasi-elastic component of the diffuse scattering found in Ref. 13. A cooled Be filter was used to remove higher order wavelengths from the scattered beam, and was followed by an 80' radial collimator.

A neutron powder diffraction experiment was performed on two samples of $Yb_2Ti_2O_7$, using the NDPF instrument at the Lujan Neutron Scattering Center. One sample studied was a polycrystalline rod (i.e. "sintered powder"), and the other was a single crystal grown in an identical manner to the sample used in the single crystal neutron experiments. Both samples were subsequently crushed using a Fritsch Pulverisette 2 mortar grinder, for 20 minutes per sample.

The heat capacity measurements were performed using the quasi-adiabatic method (see Ref. 30 for details) with a 1 kΩ RuO_2 thermometer and 10 kΩ heater mounted directly on the thermally isolated sample. A weak thermal link to the mixing chamber of a dilution refrigerator was made using Pt-W (92% Pt, 8% W) wire for the smaller single crystal piece, A (142.3mg) and polycrystalline sample (24.37 mg), and yellow brass foil for the 7.0515 g crystal, B, used in the neutron scattering experiments. The time constant of relaxation provided by the weak link was several hours, much longer than the internal relaxation time of the samples, minimizing thermal gradients and ensuring that the sample cooled slowly into an equilibrium state. The addenda contributed less than 0.1% to the specific heat of the system.

3.1.3 Results

3.1.3.1 Diffuse Magnetic Neutron Scattering

Figure 3.1 (a) shows the temperature dependence of the intensity of elastically scattered neutrons at two **Q** points using SPINS. One point is near the fcc zone center and structurally allowed (111) Bragg peak ($\mathbf{Q}_{1.07}$ = [1.07, 1.07, 1.07]), while the other is near the fcc Brillouin zone boundary ($\mathbf{Q}_{1.54}$ = [1.54, 1.54, 1.54]). Figure 3.1 (b) locates these two points relative to the rod of diffuse scattering along [111] and the Brillouin zone boundaries, using reciprocal space maps of the elastic scattering at 30 mK and 500 mK measured with DCS. These two intensities track each other at relatively high temperatures, but they separate below $\sim$ 400 mK, with the scattering near the zone centre (at $\mathbf{Q}_{1.07}$) growing more strongly before leveling off at the lowest temperatures. The inset of Figure 3.1(a) shows the difference between the elastic intensities at $\mathbf{Q}_{1.07}$ and at $\mathbf{Q}_{1.54}$, and this resembles conventional order parameter behavior with a phase transition near 400 mK.

A longitudinal scan of the elastic scattering along the rod (i.e. along the [H,H,H] direction) shows that the low temperature buildup of intensity occurs near the (111), but not (222), zone centre (Figure 2a). Below 400mK, the scattering peaks up near (111) and the the **Q** dependence of the longitudinal scattering can be fit to an Ornstein-Zernike (Lorentzian) form, from which an interplane, or 'longitudinal', correlation length ξ_L can be determined. We find ξ_L = 3.2Å at 60mK, implying correlated spins over $\sim$ 6.4Å in the [111] direction. This indicates that even at the lowest temperatures, 3D correlations

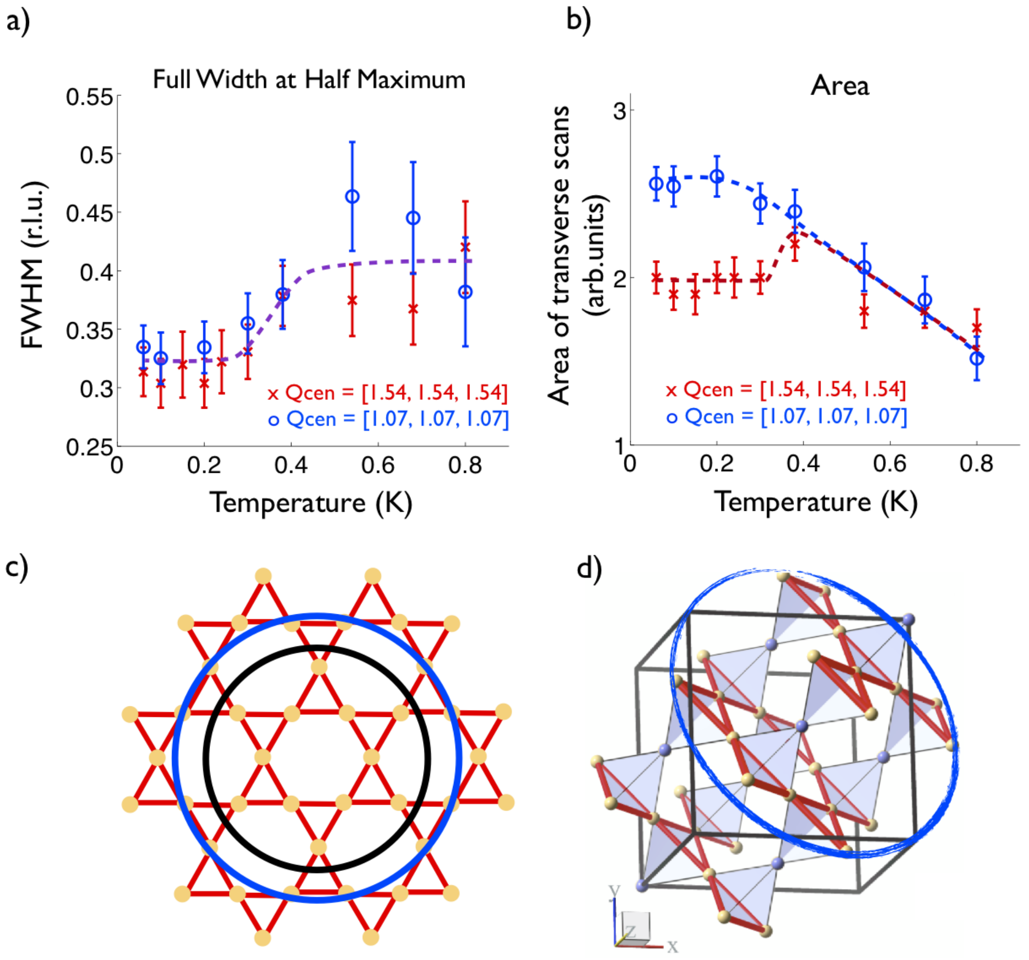

Figure 3.3: a) Full width at half maxima (FWHM), and b) integrated area extracted from the Lorentzian fits to the transverse scans shown in Fig. 2a). c) The range of ξ_T within the kagome layer. Above 400mK (black) the correlations are restricted to a single kagome star unit. Below 265mK (blue), the transverse correlations grow only to encompass the next near neighbors in the kagome layer. d) The pyrochlore lattice decomposed into kagome and interleaved triangular layers. Below 400mK, the longitudinal correlations extend only between a single KTK unit.

do not extend beyond a KTK stack, whose spatial extent is 5.8Å. Above 400mK, this interplane correlation vanishes, leaving the Yb^{3+} form factor[31] as the only contribution to the $\mathbf{Q}$ dependence of the diffuse scattering along [111] as expected for truly 2D spin correlations.

The scattering normal to the rod probes spin correlations within the kagome and triangular planes. Figure 2(b) shows scans across the rods centered on $\mathbf{Q}_{1.07}$ and $\mathbf{Q}_{1.54}$. Representative scans at T=60 mK and T=540 mK are shown. These data sets were fit to Lorentzian lineshapes, allowing the transverse correlation length and integrated area of the scattering to be determined as a function of temperature. The resolution widths appropriate to the spectrometer are shown as the horizontal bars in Fig. 2(b), and are negligibly small compared to the FWHM of the rod scattering. The results of the Lorentzian fits are plotted in Fig. 3 (a) and (b). The integrated areas at the two $\mathbf{Q}$ positions differ only for T<400mK, (Fig. 3 (b)) consistent with the behavior of the peak intensities along the rod shown in Fig. 1(a).

Meanwhile, the FWHM (Fig. 3a), which is inversely related to the transverse correlation length ξ_T, does not depend on the longitudinal position along the rod at any temperature. Below 265mK, ξ_T is constant at 9.6Å and it decreases to 7.8Å above 400mK, leaving a correlated area corresponding roughly to one kagome 'star', which has a diameter of 15.4Å. Combined with $\xi_L \sim 0$ above 400 mK, we conclude that for $T \gtrsim \Theta_{CW}$ the spin system is characterized by uncorrelated kagome stars. Figure 3(c) summarizes the size of the spin correlated regions in the kagome planes both below 265mK and above 400mK. In the ground state, which stabilizes below 265mK, short 3D spin correlations form along [111], encompassing a single KTK stack of width $\sim$ 6Å, as illustrated by the blue region in Fig.3(d).

3.1.3.2 Quasi-Elastic Neutron Scattering

Inelastic magnetic scattering can inform on the dynamics associated with this exotic disordered zero field ground state. Time-of-flight neutron scattering data is shown in Fig. 3.4 at both 30mK and 500mK, and at positions both along the [111] rod of scattering and well removed from the rod of scattering. These positions are located in the reciprocal space map of the elastic scattering shown in the Fig. 3.4 inset. Consistent with earlier work, this shows the QE scattering along the [111] direction extends to $\sim$ 0.3 meV, but that the spectral weight is depleted at energies less than 0.2 meV, on entering the ground state. Hence, a dramatic slowing down of the spin fluctuations is observed, consistent with the earlier Mössbauer and μSR results,[16] as the 3D correlated ground state forms. Application of a [110] magnetic field in excess of $\sim$ 0.5 T, induces a polarized, ordered state, and completely eliminates the diffuse scattering. Thus, the data in Fig. 3 (c) at 30 mK and 5 T serves as a measure of the background.

Comparison of the of zero-field quasi-elastic diffuse scattering to the non-magnetic background revealed in a magnetic field of 5T makes it clear that although diffuse scattering is organized into rods of scattering along [111], there is appreciable diffuse, inelastic scattering throughout the Brillouin zone. This “off-rod” scattering has a relatively flat energy dependence out to 0.6meV. Furthermore, unlike the rod diffuse scattering along [111], the “off-rod” diffuse

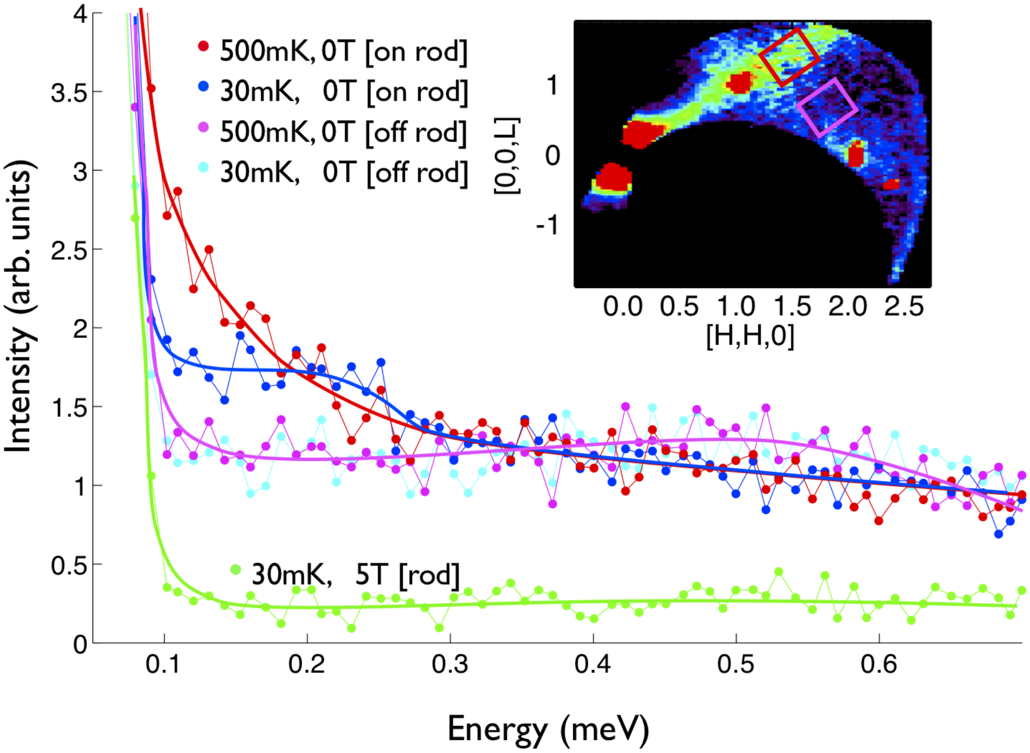

Figure 3.4: Energy dependence of the diffuse scattering above and below T_c, both on and off the rod of scattering. Thick lines are guides to the eye. Inset: range of binning for the on- and off-rod positions. On-rod: HHH=[1.2,1.6], HH-2H= $[-0.1, 0.1]$. Off-rod: HHH=[1.2,1.6], HH-2H=[0.3,0.5].

scattering shows no temperature dependence between 500mK and 30mK. This implies that a dynamic and essentially uncorrelated component of the spins persists in the zero-field ground state. A similar situation is encountered in the classical spin ice $Ho_2Ti_2O_7$, which retains appreciable *elastic* diffuse scattering throughout the Brillouin zone at very low temperatures, indicating static zero-field spin correlations that encapsulate at most a single tetrahedron.[5]

3.1.3.3 Specific Heat

The specific heat provides insight into the extent to which the entropy changes at temperatures relevant to the diffuse scattering. Figure 3.5 shows specific heat results of poly- and single-crystalline samples, including the sample from the neutron scattering study. There is significant sample dependence of the low temperature C_p anomaly, with at least one feature occurring between 150mK and 265mK in all samples. The sharpest anomaly is observed in our powder sample, at a temperature that seems to be the upper limit for all others, T=265mK. Significantly, our powder C_p peak is sharper by an order of magnitude, and occurs at a higher temperature than both the original powder C_p data by Blöte *et al*, as well as the powder C_p data by Dalmas de Réotier *et al*, which displays an anomaly at 250mK with a peak height of ~9 J/K mol Yb.[20] The neutron scattering sample B exhibits a sharp peak at 265mK, but also has a broad feature as seen in sample A.

The specific heat does not show any indication of a feature at 400mK. This indicates that the buildup of 3D correlations, as well as the small increase in transverse correlation length, produces, at most, subtle changes in the entropy. This could be another manifestation of the persistently short correlation lengths at all temperatures. However, an important question remains - what is the physical significance of the C_p features at 265mK and 200mK observed in the neutron scattering crystal? Drawing on the large change in spin fluctuation frequency observed by Hodges *et al* at 240mK in their powder sample,[16] we should expect a change in dynamics at these temperatures. As discussed

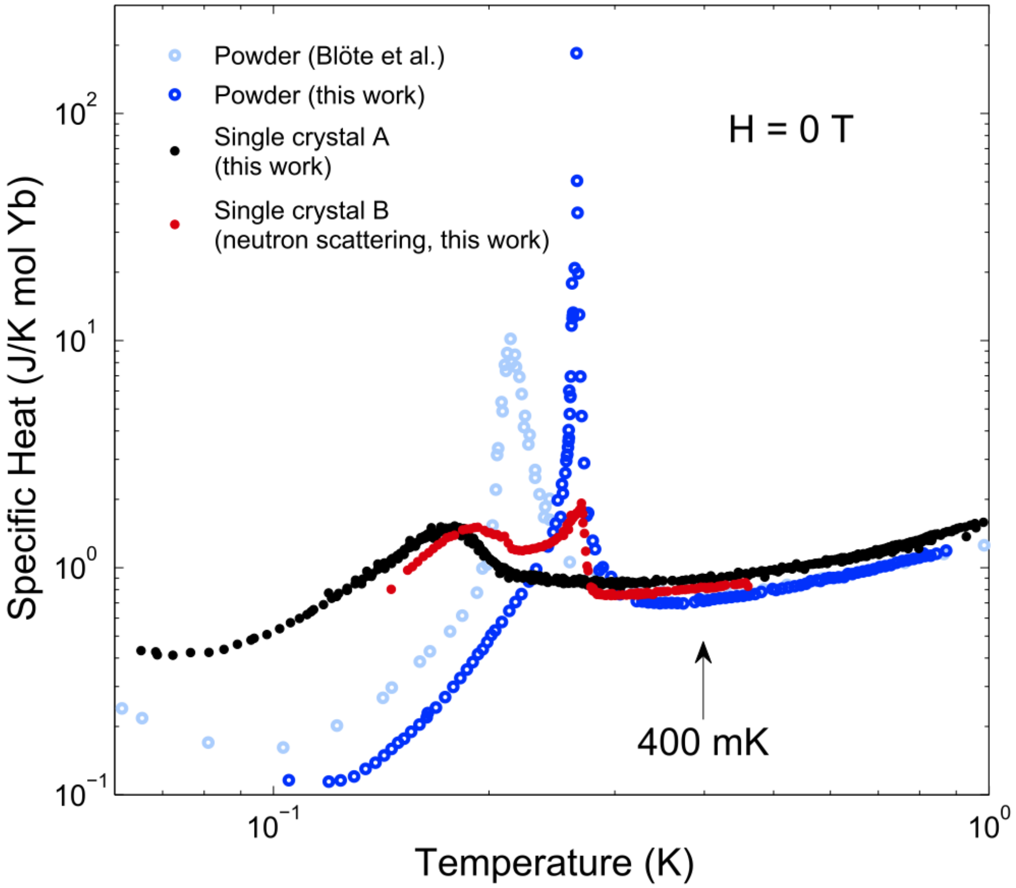

Figure 3.5: Examples of low temperature specific heat in $Yb_2Ti_2O_7$. Significant sample dependence is observed in both powders and single-crystals. The powder sample prepared at McMaster University shows the highest temperature (265mK) and sharpest anomaly. The neutron scattering sample, B, shows a sharp peak at 265mK similar to the powder, and a broad, low temperature feature similar to crystal A. None of the samples studied had any feature at 400mK.

in relation to Fig. 4, we do observe a change in dynamics between 500mK and 30mK but the intermediate temperature regime awaits further study.

3.1.3.4 Structural Information

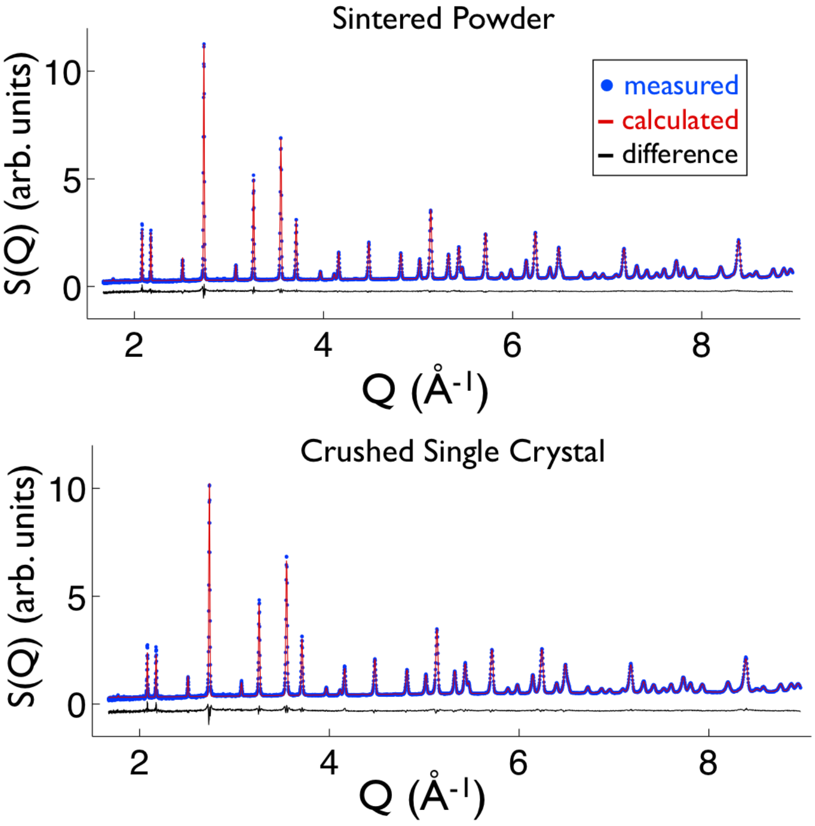

Figure 3.6: Neutron diffraction data from two samples of $Yb_2Ti_2O_7$ taken at 250K: a sintered powder (top) and a crushed single crystal (bottom). The result of Rietveld analysis, using a fully ordered model for $Yb_2Ti_2O_7$, is shown in red. The difference between the measured and calculated profiles is in black.

To investigate structural differences between the single crystals as grown by the method described in Section II, and the polycrystalline material which was used as the starting material for these growths (the "sintered powder"), we turn to neutron powder diffraction results. After a successful growth, a single crystal was crushed back into polycrystalline form in order to facilitate direct comparison to the sintered powder. Figure 3.6 shows the two neutron diffraction patterns from the powder and crushed single crystal at 250K. The data is normalized to the incident time-of-flight spectrum, and corrected for detector efficiency using a vanadium normalization. A Rietveld refinement was performed on both patterns using a fully ordered model of the pyrochlore structure (see, for example, Ref. 32 for details of this structure). The results indicate that both the powder and crushed crystal are described extremely well by the fully ordered model, with R_p values of 2.16% and 2.83% respectively. Some differences can be observed between the two samples, namely that the crushed crystal has a larger lattice parameter ($a_{xtal} = 10.02006(2)$ compared to $a_{pow} = 10.01322(1)$) as well as greater widths of the Bragg peaks, indicating lattice strain. Site substitution between Yb^{3+} and Ti^{4+} was found not to be important for either sample (refinement gives less than 1% substitution in both cases).

A detailed, temperature-dependent Rietveld refinement as well as Pair Distribution Function analysis is forthcoming, but these preliminary results already indicate that there are only subtle structural differences between the two forms of $Yb_2Ti_2O_7$, pointing to random disorder or lattice strain as the root cause for the differences in specific heat.

3.1.4 Conclusions

In summary, we have explored, using diffuse and inelastic neutron scattering, the transformation of spin correlations as $Yb_2Ti_2O_7$ enters its exotic ground state at zero field. Within this ground state, we observe slow, short-range 3D correlated fluctuations that extend over single KTK stacks. In contrast, at temperatures characteristic of Θ_{CW} and above, the system is comprised of decoupled kagome stars, with 2D spin correlations confined to single kagome units. The temperature $T^* \simeq 400$mK at which correlations lose their 3D nature and also shrink in the 2D kagome plane is found to be much higher than any of the temperatures $T_c < 265$mK marking anomalies in C_p. Random structural disorder or lattice strain may account for the variability in T_c and the sharpness of the associated anomalies, but would seem unlikely to be the factor capping the extremely short range of correlations in the ground state. Both $T^* \simeq 400$mK and the highest $T_c = 265$mK observed are an order of magnitude smaller than the predicted mean-field transition temperature, 3.2K.[21] It is clear that the transition to the exotic ground state, whether this be characterized by T_c and/or T^*, is strongly suppressed by geometrical frustration, quantum fluctuations, or both.

The authors acknowledge many useful discussions with M.J.P. Gingras, J.D. Thompson, and P. A. McClarty, and are grateful for technical assistance from Y. Qiu. This work has benefited from the use of the NPDF beamline at the Lujan Center at Los Alamos Neutron Science Center, funded by the US DOE Office of Basic Energy Sciences. Los Alamos National Laboratory is operated by Los Alamos National Security LLC under DOE contract No.

DE-AC52-06NA25396. This work utilized facilities supported in part by the National Science Foundation under Agreement No. DMR-0944772, and was supported by NSERC of Canada.

3.2 * References

[1] C. Lacroix, P. Mendels, and F. Mila, *Introduction to Frustrated Magnetism* (Springer Series in Solid-State Sciences, Heidelberg, 2011).

[2] J. S. Gardner, M. J. P. Gingras, and J. E. Greedan, Reviews of Modern Physics **82**, 53 (2010).

[3] S. T. Bramwell, M. J. Harris, B. C. den Hertog, M. J. P. Gingras, J. S. Gardner, D. F. McMorrow, A. R. Wildes, A. L. Cornelius, J. D. M. Champion, R. G. Melko, and T. Fennell, Phys. Rev. Lett. **87**, 047205 (2001).

[4] S. T. Bramwell and M. J. P. Gingras, Science **294**, 1495 (2001).

[5] J. P. Clancy, J. P. C. Ruff, S. R. Dunsiger, Y. Zhao, H. A. Dabkowska, J. S. Gardner, Y. Qiu, J. R. D. Copley, T. Jenkins, and B. D. Gaulin, Phys. Rev. B **79**, 014408 (2009).

[6] J. S. Gardner, S. R. Dunsiger, B. D. Gaulin, M. J. P. Gingras, J. E. Greedan, R. F. Kiefl, M. D. Lumsden, W. A. MacFarlane, N. P. Raju, J. E. Sonier, I. Swainson, and Z. Tun, Phys. Rev. Lett. **82**, 1012 (1999).

[7] J. S. Gardner, B. D. Gaulin, A. J. Berlinsky, P. Waldron, S. R. Dunsiger, N. P. Raju, and J. E. Greedan, Physical Review B **64**, 224416 (2001).

[8] N. P. Raju, M. Dion, M. J. P. Gingras, T. E. Mason, and J. E. Greedan, Phys. Rev. B **59**, 14489 (1999).

[9] J. D. M. Champion, A. S. Wills, T. Fennell, S. T. Bramwell, J. S. Gardner, and M. A. Green, Phys. Rev. B **64**, 140407 (2001).

[10] J. R. Stewart, G. Ehlers, A. S. Wills, S. T. Bramwell, and J. S. Gardner, Journal of Physics: Condensed Matter **16**, L321 (2004).

[11] J. D. M. Champion, M. J. Harris, P. C. W. Holdsworth, A. S. Wills, G. Balakrishnan, S. T. Bramwell, E. Čižmár, T. Fennell, J. S. Gardner, J. Lago, D. F. McMorrow, M. Orendáč, A. Orendáčová, D. M. Paul, R. I. Smith, M. T. F. Telling, and A. Wildes, Phys. Rev. B **68**, 020401 (2003).

[12] J. P. C. Ruff, J. P. Clancy, A. Bourque, M. A. White, M. Ramazanoglu, J. S. Gardner, Y. Qiu, J. R. D. Copley, M. B. Johnson, H. A. Dabkowska, and B. D. Gaulin, Phys. Rev. Lett. **101**, 147205 (2008).

[13] K. A. Ross, J. P. C. Ruff, C. P. Adams, J. S. Gardner, H. A. Dabkowska, Y. Qiu, J. R. D. Copley, and B. D. Gaulin, Phys. Rev. Lett. **103**, 227202 (2009).

[14] S. T. Bramwell, M. N. Field, M. J. Harris, and I. P. Parkin, Journal of Physics: Condensed Matter **12**, 483 (2000).

[15] J. Hodges, P. Bonville, A. Forget, M. Rams, K. Królas, and G. Dhalenne, Journal of Physics: Condensed Matter **13**, 9301 (2001).

[16] J. A. Hodges, P. Bonville, A. Forget, A. Yaouanc, P. Dalmas de Réotier, G. André, M. Rams, K. Królas, C. Ritter, P. C. M. Gubbens, C. T. Kaiser, P. J. C. King, and C. Baines, Phys. Rev. Lett. **88**, 077204 (2002).

[17] B. Z. Malkin, A. R. Zakirov, M. N. Popova, S. A. Klimin, E. P. Chukalina, E. Antic-Fidancev, P. Goldner, P. Aschehoug, and G. Dhalenne, Phys. Rev. B **70**, 075112 (2004).

[18] H. B. Cao, A. Gukasov, I. Mirebeau, and P. Bonville, J. Phys. : Condens. Matter **21**, 492202 (2009).

[19] H. Blöte, R. Wielinga, and W. Huiskamp, Physica **43**, p. 549 (1969).

[20] P. Dalmas de Réotier, V. Glazkov, C. Marin, A. Yaouanc, P. C. M. Gubbens, S. Sakarya, P. Bonville, A. Amato, C. Baines, and P. J. C. King, Physica B: Condensed Matter **374**, 145 (2006).

[21] K. A. Ross, L. Savary, B. D. Gaulin, and L. Balents, Physical Review X **1**, 16 (2011).

[22] J. D. Thompson, P. A. McClarty, H. M. Rønnow, L. P. Regnault, A. Sorge, and M. J. P. Gingras, Physical Review Letters **106**, 187202 (2011).

[23] J. D. Thompson, P. A. McClarty, and M. J. P. Gingras, J. Phys. : Condens. Matter **23**, 164219 (2011).

[24] J. S. Gardner, G. Ehlers, N. Rosov, R. W. Erwin, and C. Petrovic, Phys. Rev. B **70**, 180404 (2004).

[25] Y. Yasui, M. Soda, S. Iikubo, M. Ito, M. Sato, N. Hamaguchi, T. Matsushita, N. Wada, T. Takeuchi, N. Aso, and K. Kakurai, Journal of the Physical Society of Japan **72**, 3014 (2003).

[26] P. Bonville, J. Hodges, E. Bertin, J. P. Bouchaud, P. Dalmas de Réotier, L. P. Regnault, H. Rønnow, J. P. Sanchez, S. Sosin, and A. Yaouanc, Hyperfine interactions **156**, 103 (2004).

[27] M. Hermele, M. P. A. Fisher, and L. Balents, Phys. Rev. B **69**, 064404 (2004).

[28] A. Banerjee, S. V. Isakov, K. Damle, and Y. B. Kim, Phys. Rev. Lett. **100**, 47208 (2008).

[29] J. S. Gardner, B. D. Gaulin, and D. M. Paul, Journal of Crystal Growth **191**, 740 (1998).

[30] J. A. Quilliam, C. G. A. Mugford, A. Gomez, S. W. Kycia, and J. B. Kycia, Phys. Rev. Lett. **98**, 037203 (2007).

[31] P. J. Brown, International Tables for Crystallography **C**, 454 (2006).

[32] J. E. Greedan, D. Gout, A. D. Lozano-Gorrin, S. Derahkshan, T. Proffen, H. J. Kim, E. Božin, and S. J. L. Billinge, Phys. Rev. B **79**, 014427 (2009).

Chapter 4

Quantum Spin Ice

This chapter incorporates the article *"Quantum Excitations in Quantum Spin Ice"*, which has been published in Physical Review X. The full reference is given below:

K.A. Ross, L.Savary, B.D. Gaulin, and L. Balents. Physical Review X, **1**, 021002 (2011).*

Figures 4.1, 4.2, 4.3, 4.4, 4.5, and 4.6 are reproduced from the above article with permission.

For this work, we took advantage of the large dataset obtained from our intial time-of-flight experiment on $Yb_2Ti_2O_7$ at the Disk Chopper Spectrometer (DCS). Some of that data has already been presented in Chapter 2. This paper takes a different approach and uses the *full* set of inelastic neutron scattering information in the field-polarized phase of $Yb_2Ti_2O_7$, for which we measured the energy dispersion of spin wave excitations in the (HHL) scattering plane at both H=2T and H=5T, for T=30mK. DCS has a large bank of detectors

---

which cover a significant range of scattering angles, which, when coupled with sample rotation in fixed angular increments, produces data that covers the full (HHL) plane for both elastically and inelastically scattered neutrons. This allowed us to take slices through the plane in any direction so-desired. In this way, we obtain $S(\vec{Q},\omega)$ for 5 indepedent directions in the (HHL) plane.

This detailed measurement of the spin wave dispersions in the field-polarized phase allows one to extract parameters for a realistic model Hamiltonian, as we have done here. The work contained in this chapter unveils a remarkably accurate Hamiltonian for $Yb_2Ti_2O_7$, which necessarily includes the full symmetry-allowed anisotropy of the exchange interactions. Four independent exchange parameters were extracted from fits to the $S(\vec{Q},\omega)$ data using linear spin wave theory. The parameters we extract are remarkable in that they confirm the the dominant ferromagnetic Ising-like nature of the exchange interaction (in contrast to the XY nature of the g-tensor, which describes the size of the magnetic moments when they are oriented along various local directions), as well as quantify the nature and degree of quantum fluctuations that are introduced by the planar terms in the Hamiltonian.

These parameters allow us to think of $Yb_2Ti_2O_7$ as a frustrated spin ice material (similar to $Ho_2Ti_2O_7$ and $Dy_2Ti_2O_7$), but with significant quantum fluctuations. The frustration and quantum fluctuations push $Yb_2Ti_2O_7$ towards a disordered ground state called a Coulombic Quantum Spin Liquid. While the exact theoretical description of the ground state of this model with these parameters is still unknown, it is now suspected (particularly because of work presented in the preceding chapter) that the disordered nature of the zero-field ground state, as observed in several experiments including our own, may arise from a small density of structural defects, rather than being intrinsically present in a "perfect" sample of $Yb_2Ti_2O_7$. Chapter 5 will show that these defects are quite low in concentration, indicating that if the true ground state of $Yb_2Ti_2O_7$ is ordered, it is unusually unstable in the presence of perturbations. This is perhaps a sign that the exchange parameters extracted here place $Yb_2Ti_2O_7$ near the boundary of several competing phases.

I would like to stress that this work is a "true" collaboration between the theory group at UC Santa Barbara (Leon Balents and his Ph.D. student Lucile Savary) and the group at McMaster University (Bruce Gaulin and myself), in the sense that each group provided significant and vital contributions to the work. All of the theoretical modelling and analysis was executed by the UC Santa Barbara group. The experiment was of course performed by the McMaster group. Once a model Hamiltonian and spin wave theory had been developed, I constructed a method to perform least squares fits to the data, and successfully extracted the four exchange parameters. Details of the fitting procedure are found in Appendix 4.D of this chapter. The other appendices in this chapter (which are also included in the published article) outline the theoretical procedures relevant to this work. These were performed and written by the UC Santa Barbara group, and I include them here for completeness.

4.1 Quantum Excitations in Quantum Spin Ice

Kate A. Ross,[1] Lucile Savary,[2] Bruce D. Gaulin,[1,3,4] Leon Balents[5]

[1] *Department of Physics and Astronomy, McMaster University, Hamilton, Ontario, L8S 4M1, Canada*

[2] *Ecole Normale Supérieure de Lyon, 46, allée d'Italie, 69364 Lyon Cedex 07, France*

[3] *Canadian Institute for Advanced Research, 180 Dundas St. W., Toronto, Ontario, M5G 1Z8, Canada*

[4] *Brockhouse Institute for Materials Research, McMaster University, Hamilton, Ontario, L8S 4M1, Canada*

[5] *Kavli Institute for Theoretical Physics, University of California, Santa Barbara, CA, 93106-4030, U.S.A.*

Abstract

Recent work has highlighted remarkable effects of classical thermal fluctuations in the dipolar spin ice compounds, such as "artificial magnetostatics", manifesting as Coulombic power-law spin correlations and particles behaving as diffusive "magnetic monopoles". In this paper, we address *quantum* spin ice, giving a unifying framework for the study of magnetism of a large class of magnetic compounds with the pyrochlore structure, and in particular discuss $Yb_2Ti_2O_7$ and extract its full set of Hamiltonian parameters from high field inelastic neutron scattering experiments. We show that fluctuations in $Yb_2Ti_2O_7$ are strong, and that the Hamiltonian may support a Coulombic "Quantum Spin Liquid" ground state in low field and host an unusual quantum

critical point at larger fields. This appears consistent with puzzling features in prior experiments on $Yb_2Ti_2O_7$. Thus $Yb_2Ti_2O_7$ is the first quantum spin liquid candidate in which the Hamiltonian is quantitatively known.

Rare earth pyrochlores display a diverse set of fascinating physical phenomena [1]. One of the most interesting aspects of these materials from the point of view of fundamental physics is the strong frustration experienced by coupled magnetic moments on this lattice. The best explored materials exhibiting this frustration are the "spin-ice" compounds, $Ho_2Ti_2O_7$, $Dy_2Ti_2O_7$, in which the moments can be regarded as *classical* spins with a strong easy-axis (Ising) anisotropy [2, 3]. The frustration of these moments results in a remarkable *classical spin liquid* regime displaying Coulombic correlations and emergent "magnetic monopole" excitations that have now been studied extensively in theory and experiment [4, 5, 6].

Strong quantum effects are absent in the spin ice compounds, but can be significant in other rare earth pyrochlores. In particular, in many materials the low energy spin dynamics may be reduced to that of an effective spin $S = 1/2$ moment, with the strongest possible quantum effects expected. In this case symmetry considerations reduce the exchange constant phase space of the nearest neighbor exchange Hamiltonian to a maximum of three dimensionless parameters [7]. The compounds $Yb_2Ti_2O_7$, $Er_2Ti_2O_7$, $Pr_2Sn_2O_7$[1] (and possibly $Tb_2Ti_2O_7$[8]) are of this type, and it has recently been argued that the spins in $Yb_2Ti_2O_7$ and $Er_2Ti_2O_7$ are controlled by exchange coupling rather than by the long-range dipolar interactions which dominate in spin ice [9, 10]. This makes these materials beautiful examples of strongly quantum magnets on the highly frustrated pyrochlore lattice. They are also nearly ideal subjects for detailed experimental investigation, existing as they do in large high purity single crystals, and with large magnetic moments amenable to neutron scattering studies. $Yb_2Ti_2O_7$ is particularly appealing because its lowest Kramers doublet is extremely well separated from the first excited one [11], and a very large single crystal neutron scattering data set is available, allowing us to measure the full Hamiltonian quantitatively, as we will show. Although we specialize to the latter material in the present article the theoretical considerations and parameter determination method described here will very generally apply to *all* pyrochlore materials where exchange interactions dominate and whose dynamics can be described by that of a single doublet.

Theoretical studies have pointed to the likelihood of unusual ground states of quantum antiferromagnets on the pyrochlore lattice [12, 13]. Most exciting is the possibility of a *quantum spin liquid* (QSL) state, which avoids magnetic ordering and freezing even at absolute zero temperature, and whose elementary excitations carry fractional quantum numbers and are decidedly different from spin waves [14]. Intriguingly, neutron scattering measurements have reported a lack of magnetic ordering and the absence of spin waves in $Yb_2Ti_2O_7$ at low fields [15, 16]. In a recent study, sharp spin waves emerged when a magnetic field of 0.5T or larger was applied, suggesting that the system transitioned into a conventional state [16]. The possible identification of the low field state with a quantum spin liquid is tantalizing, but progress certainly requires a more detailed understanding of the spin Hamiltonian.

In this article, we present a detailed experimental and theoretical investigation of the excitation spectrum in the high field state throughout the Brillouin zone. We show that the spectrum is extremely well fit by spin wave theory, and through this fit we unambiguously extract *all* the microscopic exchange parameters in the spin Hamiltonian (see below). Interestingly, we find that the largest exchange interaction is of the same "frustrated ferromagnetic" Ising type as in spin ice, despite the fact that the g-tensor tends to orient magnetic moments primarily normal to the Ising axes. Moreover, spin-flip terms which induce quantum dynamics are comparable to the Ising exchange, which confirms the picture of $Yb_2Ti_2O_7$ as a strongly quantum magnet, in qualitative agreement with recent studies [17, 10, 18]. Strikingly, we find that the predictions of mean field theory (MFT) using these parameters disagree drastically with experiment in zero field, indicating that fluctuations strongly reduce or destroy the classically expected spin order. Taken together, these observations make $Yb_2Ti_2O_7$ a promising candidate for observation of QSL physics. The precise determination of the microscopic spin interactions sets the stage for a quantitative understanding and test of this proposal.

Time-of-flight neutron scattering measurements were performed on a 7g single crystal of $Yb_2Ti_2O_7$, grown via the optical floating zone method. Details of the crystal growth were given elsewhere [16, 19]. The neutron scattering data was collected at the Disk Chopper Spectrometer at the NIST Center for Neutron Research, using 5Å incident neutrons. This configuration allowed an energy resolution of 0.09meV. The sample environment consisted of a 11.5T vertical field magnet combined with a dilution insert that achieved a base temperature of 30mK. The scattering plane was HHL, with the field applied along the $[1\bar{1}0]$ vertical direction. The sample was rotated 147 degrees in 1.5 degree steps about the vertical, allowing a three dimensional data set to be acquired, i.e. two components of the wavevector $\mathbf{Q}$ within the scattering plane, and energy transfer. The spin excitation spectra along several high symmetry directions with the scattering plane were thereby obtained.

At 30mK, the inelastic spectrum changes qualitatively at $H = 0.5$T; above this field strength, resolution-limited spin wave excitations which go soft with quadratic dispersion at nuclear-allowed positions develop, indicating a transition to a field-polarized ferromagnetic state [16]. The spin wave excitations indicate that the symmetry of the underlying lattice is preserved, as is evident from gaps in the spectrum at the nuclear zone boundaries. In Figure 4.1 we show the spin wave dispersions along several directions in the HHL plane for $H = 2$T and $H = 5$T. These high symmetry directions are shown relative to the Brillouin zone structure within the HHL plane in Fig. 4.2.

We compare the experimental data to spin-wave theory. We assume nearest-neighbor exchange coupling only, as appropriate to the strongly localized f-electron states, and neglect dipolar interactions. The Hamiltonian, written in global spin coordinates, is then

$$H = \frac{1}{2}\sum_{ij} J_{ij}^{\mu\nu} S_i^{\mu} S_j^{\nu} - \mu_B H^{\mu} \sum_i g_i^{\mu\nu} S_i^{\nu}, \tag{4.1}$$

where $J_{ij}^{\mu\nu} = J_{ji}^{\nu\mu}$ is the matrix of exchange couplings between sites i and j, $g_i^{\mu\nu}$ is the g-tensor for the spin at site i, and we take $\hbar = 1$. Symmetry allows four independent exchange constants,[7] $J_1, \cdots, J_4$. To specify them, we give the exchange matrix on one pair of nearest-neighbor sites, located at positions

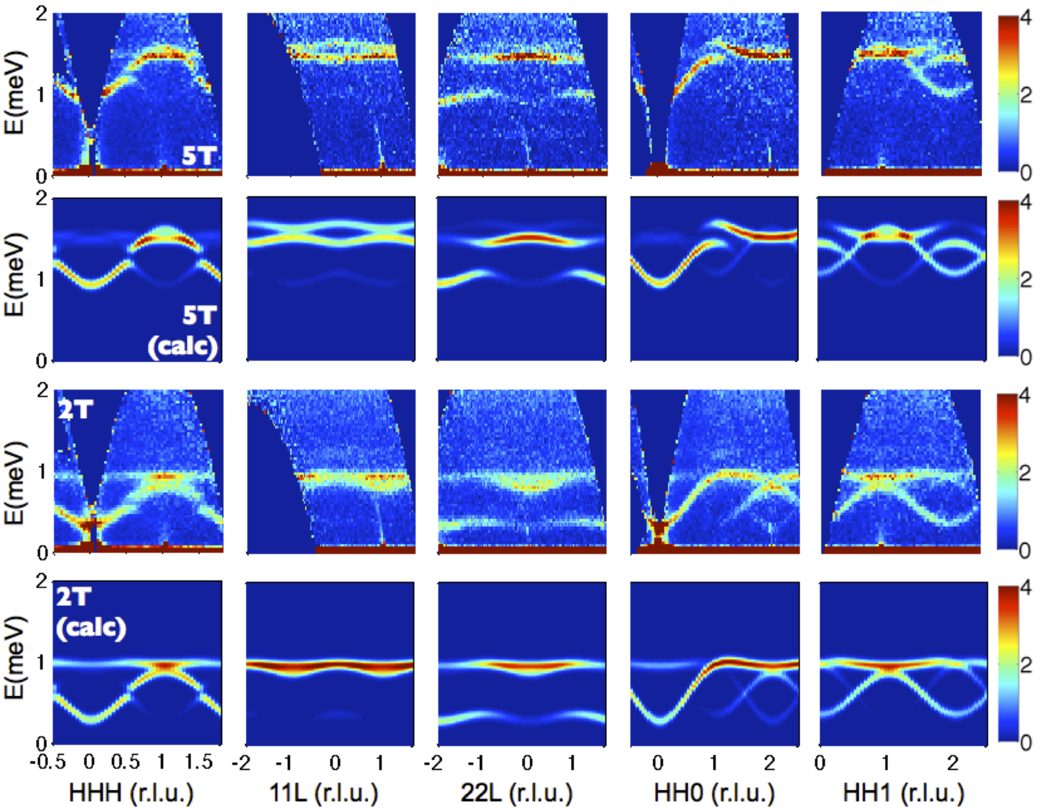

Figure 4.1: Color) The measured $S(\mathbf{Q},\omega)$ at $T = 30$mK, sliced along various directions in the HHL plane, for both $H = 5$T (first row) and $H = 2$T (third row). The second and fourth row show the calculated spectrum for these two field strengths, based on an anisotropic exchange model with five free parameters (see text) that were extracted by fitting to the 5T data set. For a realistic comparison to the data, the calculated $S(\mathbf{Q},\omega)$ is convoluted with a gaussian of full-width 0.09meV. Both the 2T and 5T data sets, comprised of spin wave dispersions along five different directions, are described extremely well by the same parameters.

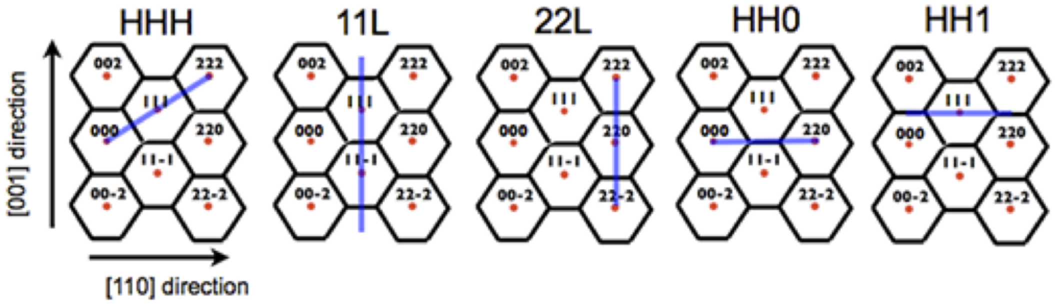

Figure 4.2: Color) Representations of the HHL scattering plane, showing the FCC Brillouin zone boundaries and the corresponding zone centers (labelled in terms of the conventional simple-cubic unit cell). Blue lines indicate the directions of the five different cuts shown in Figure 4.1.

$\mathbf{r}_0 = \frac{a}{8}(1,1,1)$ and $\mathbf{r}_1 = \frac{a}{8}(1,-1,-1)$ on a tetrahedron centered at the origin (a is the conventional cubic lattice spacing for the fcc Bravais lattice):

$$\mathbf{J}_{01} = \begin{pmatrix} J_2 & J_4 & J_4 \\ -J_4 & J_1 & J_3 \\ -J_4 & J_3 & J_1 \end{pmatrix}. \tag{4.2}$$

The other exchange matrices can be obtained from this one by cubic rotations given in Appendix 4.A. The g-tensor contains two components: g_z parallel to and g_{xy} perpendicular to the *local* C_3 rotation axis through the Yb site.

Spin wave theory, carried out as described in Appendix 4.C, is fit to the $H = 5\,\mathrm{T}$, $T = 30\,\mathrm{mK}$ measurements; the fitting procedure focuses on the dispersion relation alone, and the overall intensity of the calculated spin waves is scaled to agree with the experiment at a single wavevector and energy point. The resulting inelastic structure factor $S(\mathbf{Q}, \omega)$ (see Appendix 4.C) is compared to both the 5T and 2T data in Figure 4.1. The best fit is achieved with the following exchange parameters, in meV:

$$\begin{aligned} J_1 &= -0.09 \pm 0.03, \qquad J_2 = -0.22 \pm 0.03, \\ J_3 &= -0.29 \pm 0.02, \qquad J_4 = 0.01 \pm 0.02. \end{aligned} \tag{4.3}$$

Here we quote rough uncertainties obtained by the visual comparison of the theoretical and experimental intensities. The fit is performed by taking the ratio of components of the g-tensor to be $g_{xy}/g_z = 2.4$, i.e. the ratio obtained by Ref. [11]. The fit then produces $g_z = 1.80$, in nearly perfect agreement with these studies (using the g-factor ratio of Cao *et al.* instead [17], i.e. $g_{xy}/g_z = 1.8$, does not reproduce the data as precisely). Using these results, a high temperature expansion gives (see Appendix 4.B) a theoretical Curie-Weiss temperature $\Theta_{CW} = 312$mK, which is comparable to but smaller than the experimentally determined values, $\Theta_{CW} = 400$mK [20] and 750mK [11]. The deviations may be explained by the sensitivity of the theoretical value to small changes in the g-factors and exchange parameters, and to the dependence of the experimental value on the fitting range [17]. Furthermore, and most importantly, our extracted exchange parameters correctly reproduce relative intensities as well as the shape of the spin wave dispersion for each of the five directions. Agreement is excellent for $H = 2$T, showing that these parameters produce a robust description of the field-induced ferromagnetic state. We note, however, that there is a significant quantitative disagreement with the exchange parameters quoted in Refs. [9, 10] (see Appendix 4.H).

Implications: The excellent agreement with spin-wave theory for fields $H \geq 2$T clearly indicates that the high field state is accurately modeled semiclassically, and is smoothly connected to the fully polarized limit. Theoretically, the ground state in this regime breaks no symmetries, and supports a ferromagnetic polarization along the axis of the applied field (for the $\langle 110 \rangle$ field used in the experiment). However, the semiclassical analysis clearly and dramatically fails at small fields, where the measurements show no signs of spontaneous long range order.[16] The classical zero field ground state for our Hamiltonian parameters has a large spontaneous polarization along the $\langle 100 \rangle$ axis. Extension of this analysis to a $T > 0$ mean-field theory wrongly predicts a continuous magnetic ordering transition at a temperature of $T_c^{MF} = 3.2$K (see Appendix 4.F). The experimental indications of a zero-field transition to long range order are mixed [21, 22], but early specific heat measurements[20] found an anomaly at $T_c = 214$mK, and Mössbauer spectroscopy [15] suggested a transition at 240mK. This temperature is approximately 14 times lower than T_c^{MF}. If there is magnetic ordering at all, it appears to be substantially suppressed, indicating strong fluctuations – classical, quantum, or both.

The presence of strong fluctuations makes a QSL ground state plausible in low field. We now use the Hamiltonian parameters to suggest the nature of this state. To do so, we rewrite the zero field Hamiltonian in terms of spins quantized along the local C_3 axis for each site, similarly to Ref. [18]:

$$\begin{aligned} H &= \sum_{\langle ij\rangle} \Big\{ J_{zz} \mathsf{S}_i^z \mathsf{S}_j^z - J_{\pm} (\mathsf{S}_i^+ \mathsf{S}_j^- + \mathsf{S}_i^- \mathsf{S}_j^+) \\ &\quad + J_{\pm\pm} \left[\gamma_{ij} \mathsf{S}_i^+ \mathsf{S}_j^+ + \gamma_{ij}^* \mathsf{S}_i^- \mathsf{S}_j^- \right] \\ &\quad + J_{z\pm} \left[\mathsf{S}_i^z (\zeta_{ij} \mathsf{S}_j^+ + \zeta_{ij}^* \mathsf{S}_j^-) + i \leftrightarrow j \right] \Big\}, \end{aligned} \tag{4.4}$$

where here S_i^μ are *local* spin coordinates, $J_{zz} = -\frac{1}{3}(2J_1 - J_2 + 2(J_3 + 2J_4))$, $J_\pm = \frac{1}{6}(2J_1 - J_2 - J_3 - 2J_4)$, $J_{\pm\pm} = \frac{1}{6}(J_1 + J_2 - 2J_3 + 2J_4)$ and $J_{z\pm} = \frac{1}{3\sqrt{2}}(J_1 + J_2 + J_3 - J_4)$, and the matrices γ_{ij}, ζ_{ij} consist of unimodular complex numbers (given in the Appendix 4.A). From the fits in Eq. (4.3), we find, in meV,

$$\begin{aligned} J_{zz} &= 0.17 \pm 0.04, \qquad J_\pm = 0.05 \pm 0.01, \\ J_{\pm\pm} &= 0.05 \pm 0.01, \qquad J_{z\pm} = -0.14 \pm 0.01, \end{aligned} \tag{4.5}$$

where the uncertainties have been estimated by treating those in Eq. (4.3) as Gaussian random variables. Note that the strongest interaction is $J_{zz} > 0$, which precisely coincides with the nearest-neighbor spin-ice model. The model with $J_\pm$ and J_{zz} only has been studied theoretically [23, 13]. It does indeed support a QSL ground state, for sufficiently small $J_\pm/J_{zz}$. For larger $J_\pm/J_{zz}$, the ground state is instead a magnet with $\langle S_i^\pm \rangle \neq 0$ [23]. While the actual value of $J_\pm/J_{zz} \approx 0.3$ would place this model in the magnetic state [23]. the $J_{z\pm}$ interaction in particular is non-negligible in $\mathrm{Yb_2Ti_2O_7}$, and preliminary theoretical work suggests that it tends to stabilize the QSL state. Indeed, in perturbation theory, the leading effect of the $J_{z\pm}$ coupling is to induce in the effective Hamiltonian a term close to the Rokhsar-Kivelson interaction of Ref. [13] (see Appendix 4.G), which was shown to stabilize the QSL [13, 24]. Although perturbation theory is strictly speaking only valid for $J_{z\pm}/J_{zz} \ll 1$, the conclusions of this analysis are likely to extend to a larger range of values. A non-perturbative study of the full Hamiltonian in Eq. (4.4) is beyond the scope of this paper, but will be reported in a future publication. Given the uncertainty in the phase boundary for the QSL state, we cannot disregard the possibility that an ideal sample of $Yb_2Ti_2O_7$ would be magnetically ordered, but that such order is here disrupted by crystal defects. This possibility should be pursued further in the future taking into account the new understanding of the Hamiltonian. We proceed now to discuss the implications of the alternative possibility of a zero field QSL state.

Many of the key properties of the QSL state of the $J_{zz} - J_{\pm}$ model were established in Ref. [13]. Conceptually, it is a quantum analog of the classical regime of Coulombic correlations observed in spin ice [5]. Specifically, where spin ice realizes an analog of magnetostatics, the QSL state of Eq. (4.4) embodies a complete fictitious *quantum electrodynamics*. In this phase, the magnetic monopoles of spin ice become full-fledged coherent excitations of the system. In addition, the QSL supports dual *electric monopoles* and a dynamical *emergent photon* mode at low energy. The complex and largely diffuse character of the scattering in zero field[16] may well be a consequence of the combination of these diverse excitations. Indeed, where a neutron can create just one spin wave ($S = 1$) excitation, the $S = 1/2$ magnetic monopoles are excited in pairs with no *individual* momentum conservation constraints. A careful comparison of theoretical modeling and focused experiments in low field is clearly needed.

A key consequence of the QSL scenario is the presence of a *quantum confinement phase transition* in applied field (see Fig. 4.3). Such a quantum phase transition is required to remove the "fractional" excitations of the QSL phase (electric and magnetic monopoles) from the spectrum in the semiclassical high field phase. Theoretically, such quantum critical points have been studied in related model Hamiltonians, and occur by a mechanism analogous to the Higgs transition in the standard model [25] or by magnetic monopole condensation [26]. The gapless excitations observed by neutrons at $H \approx 0.5$T in Ref. [16] indeed indicate a quantum critical point at this field. Further theoretical work is required for detailed comparison to experiment.

$Yb_2Ti_2O_7$ enjoys several major advantages over other materials considered candidates for QSL states up to now [14]: it is the only case in which the Hamiltonian parameters are precisely known, and for which large single-crystal samples highly suitable for detailed neutron scattering measurements are available. Moreover, similar methods may be applicable to other rare earth pyrochlores in which substantial quantum effects are present, such as $Er_2Ti_2O_7$ and $Tb_2Ti_2O_7$ [1, 8]. Especially in this broader context, the prospects for detailed observation of the long-sought QSL physics are bright. The basic framework established here will allow coordinated theoretical and experimental studies to confront the problem.

We thank M. Gingras for abundant comments on a first draft. K.A.R. acknowledges useful discussions with B. Prasanna Venkatesh. L.S. acknowl-

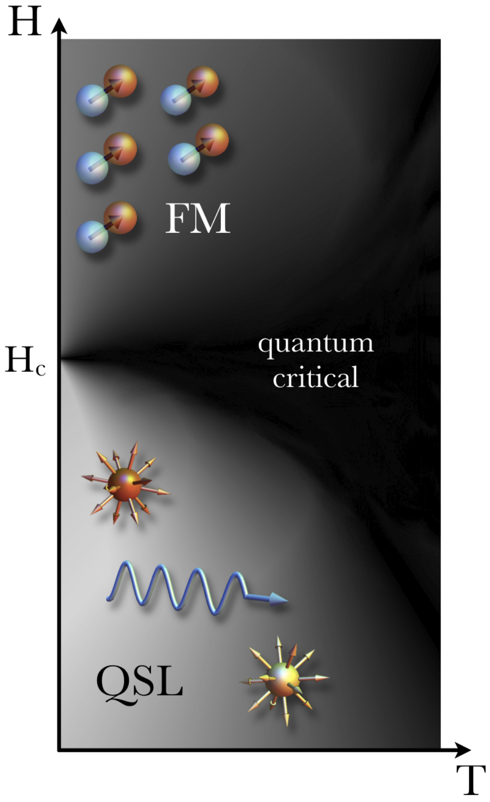

Figure 4.3: Color) Schematic phase diagram in the temperature (T) - magnetic field (H) plane, for a material in the quantum spin liquid (QSL) phase of Eq. (4.1) at $T = H = 0$. At low field and temperature, the QSL state supports exotic excitations: magnetic (red sphere) and "electric" (yellow sphere) monopoles, and an emergent photon (wavy line). The field H_c marks a quantum critical point: the confinement phase transition. For $H > H_c$, the ground state is a simple field-polarized ferromagnet (FM), and the elementary excitations are conventional magnetic dipoles. The two lines indicate crossovers to the quantum critical region between them, governed by the $T = 0$ confinement phase transition.

edges B. Canals and P. Holdsworth for many enlightening discussions, and the Institut Néel, Grenoble for hospitality. K.A.R. and B.D.G. were supported by NSERC of Canada. L.B. and L.S. were supported by the DOE through Basic Energy Sciences grant DE-FG02-08ER46524.

4.A Cubic Rotations and Local Bases

As described in the main text, we use the usual coordinate system for the pyrochlore lattice, with sites located on tetrahedra whose centers form a FCC lattice. We take one to be centered at the origin with its four corners at $\mathbf{r}_0 = \frac{a}{8}(1,1,1)$, $\mathbf{r}_1 = \frac{a}{8}(1,-1,-1)$, $\mathbf{r}_2 = \frac{a}{8}(-1,1,-1)$ and $\mathbf{r}_3 = \frac{a}{8}(-1,-1,1)$. The exchange matrices $\mathbf{J}_{ij}$ between sites of types i and j are obtained by applying the following cubic rotations $\mathcal{R}_{ij}$ to $\mathbf{J}_{01}$:

- $\mathcal{R}_{02}$ is a $\frac{2\pi}{3}$ rotation about the [111] axis,
- $\mathcal{R}_{03}$ is a $\frac{4\pi}{3}$ rotation about the [111] axis,
- $\mathcal{R}_{21}$ is a $\frac{4\pi}{3}$ rotation about the $[1\bar{1}\bar{1}]$ axis,
- $\mathcal{R}_{31}$ is a $\frac{2\pi}{3}$ rotation about the $[1\bar{1}\bar{1}]$ axis,
- $\mathcal{R}_{23}$ is a rotation made of a $\frac{2\pi}{3}$ rotation about the [111] axis followed by a $\frac{4\pi}{3}$ rotation about the $[1\bar{1}\bar{1}]$ axis.

Note $\mathbf{J}_{ji} = \mathbf{J}_{ij}^T$.

We use the following local $(\hat{\mathbf{a}}_i, \hat{\mathbf{b}}_i, \hat{\mathbf{e}}_i)$ bases

$$\begin{cases} \hat{\mathbf{e}}_0 = \frac{1}{\sqrt{3}}(1,1,1) \\ \hat{\mathbf{e}}_1 = \frac{1}{\sqrt{3}}(1,-1,-1) \\ \hat{\mathbf{e}}_2 = \frac{1}{\sqrt{3}}(-1,1,-1) \\ \hat{\mathbf{e}}_3 = \frac{1}{\sqrt{3}}(-1,-1,1), \end{cases}, \qquad \begin{cases} \hat{\mathbf{a}}_0 = \frac{1}{\sqrt{6}}(-2,1,1) \\ \hat{\mathbf{a}}_1 = \frac{1}{\sqrt{6}}(-2,-1,-1) \\ \hat{\mathbf{a}}_2 = \frac{1}{\sqrt{6}}(2,1,-1) \\ \hat{\mathbf{a}}_3 = \frac{1}{\sqrt{6}}(2,-1,1) \end{cases}, \tag{4.6}$$

$\hat{\mathbf{b}}_i = \hat{\mathbf{e}}_i \times \hat{\mathbf{a}}_i$, and the 4 × 4 complex unimodular matrices

$$\zeta = \begin{pmatrix} 0 & -1 & e^{i\frac{\pi}{3}} & e^{-i\frac{\pi}{3}} \\ -1 & 0 & e^{-i\frac{\pi}{3}} & e^{i\frac{\pi}{3}} \\ e^{i\frac{\pi}{3}} & e^{-i\frac{\pi}{3}} & 0 & -1 \\ e^{-i\frac{\pi}{3}} & e^{i\frac{\pi}{3}} & -1 & 0 \end{pmatrix}, \quad \gamma = -\zeta^*, \tag{4.7}$$

for which our exchange Hamiltonian takes the form of Eq. (4.4).

4.B Curie-Weiss Temperature

A high-temperature expansion of the Hamiltonian of Eq. (4.1) yields the $O(1/T^2)$ term in the uniform susceptibility from which we extract the Curie-Weiss temperature,

$$\begin{aligned} &\Theta_{CW} = \\ &\frac{-1}{6k_B(2g_{xy}^2+g_z^2)}\big[2g_{xy}^2(4J_1+J_2-5J_3+2J_4) \\ &+8g_{xy}g_z(J_1+J_2+J_3-J_4)+g_z^2(2J_1-J_2+2J_3+4J_4)\big], \end{aligned} \tag{4.8}$$

where k_B is the Boltzmann constant. Using the formulation of Eq. (4.4) Θ_{CW} takes the simpler form

$$\begin{aligned}\Theta_{CW} &= \frac{1}{2k_B(2g_{xy}^2+g_z^2)}\big[\, g_z^2 J_{zz} - 4g_{xy}^2(J_\pm + 2J_{\pm\pm}) \\ &\qquad -8\sqrt{2}\, g_{xy}\, g_z J_{z\pm}\,\big]. \end{aligned} \tag{4.9}$$

4.C Spin Wave Theory

As usual, we expand the Hamiltonian about one of the classical states using Holstein-Primakoff bosons in the spirit of large s, and keep only terms of and up to order s, which shall then be set to 1/2. We define the transverse Holstein-Primakoff bosons $x_a = x_a^\dagger$, $y_a = y_a^\dagger$, conjugate with one another on site a of the pyrochlore lattice, satisfying

$$[x_a, y_a] = i, \qquad n_a = \frac{x_a^2 + y_a^2}{2} - \frac{1}{2}, \tag{4.10}$$

such that

$$\mathbf{S}_a \cdot \mathbf{u}_a = s - n_a, \quad \mathbf{S}_a \cdot \mathbf{v}_a = \sqrt{s}\, x_a, \quad \mathbf{S}_a \cdot \mathbf{w}_a = \sqrt{s}\, y_a\,. \tag{4.11}$$

Here $(\mathbf{v}_a, \mathbf{w}_a, \mathbf{u}_a)$ is an orthonormal basis, chosen so that $\mathbf{u}_a$ gives the direction of the spin in the classical ground state at site a (which we find numerically). We find that for all fields, the ground state does not enlarge the unit cell, so that there are only four distinct such bases, which we denote by $a = 0, .., 3$.

One may choose, for example, $\mathbf{v}_a = \mathbf{u}_a \times (1,1,1)/\|\mathbf{u}_a \times (1,1,1)\|$ and $\mathbf{w}_a = \mathbf{u}_a \times \mathbf{v}_a$.

Since the classical ground state does not enlarge the unit cell, we can readily proceed to Fourier space in the four site basis. Keeping only terms of order s, we arrive at the spin-wave (quadratic) Hamiltonian,

$$H_{\mathbf{k}} = \left(\begin{array}{cc} X^T_{-\mathbf{k}} & Y^T_{-\mathbf{k}} \end{array} \right) \left(\begin{array}{cc} A_{\mathbf{k}} & C_{\mathbf{k}} \\ C^T_{\mathbf{k}} & B_{\mathbf{k}} \end{array} \right) \left(\begin{array}{c} X_{\mathbf{k}} \\ Y_{\mathbf{k}} \end{array} \right), \tag{4.12}$$

where $\left(\begin{array}{cc} X^T & Y^T \end{array} \right) = \left(\begin{array}{cccccc} x_0 & .. & x_3 & y_0 & .. & y_3 \end{array} \right)$ and $D^{ab}_{\mathbf{k}} = \tilde{D}_{ab} \cos(\mathbf{k} \cdot (\mathbf{r}_a - \mathbf{r}_b))$, $D = A, B, C$, with

$$\begin{aligned} \tilde{A}_{ab} &= s\mathbf{v}_a \cdot \mathbf{J}_{ab} \cdot \mathbf{v}_b + \frac{\mu_B}{2}\mathbf{H} \cdot \mathbf{g}_a \cdot \mathbf{u}_a \, \delta_{ab} - s\mathbf{u}_a \cdot \sum_b \mathbf{J}_{ab} \cdot \mathbf{u}_b \\ \tilde{B}_{ab} &= s\mathbf{w}_a \cdot \mathbf{J}_{ab} \cdot \mathbf{w}_b + \frac{\mu_B}{2}\mathbf{H} \cdot \mathbf{g}_a \cdot \mathbf{u}_a \, \delta_{ab} - s\mathbf{u}_a \cdot \sum_b \mathbf{J}_{ab} \cdot \mathbf{u}_b \\ \tilde{C}_{ab} &= s\mathbf{v}_a \cdot \mathbf{J}_{ab} \cdot \mathbf{w}_b, \end{aligned} \tag{4.13}$$

where $\mathbf{H}$ is the magnetic field and $\mathbf{J}_{ab}$ and $\mathbf{g}_a$ are 3×3 matrices with matrix elements $J^{\mu\nu}_{ab}$ and $g^{\mu\nu}_a$, respectively. To find the modes, we resort to the path-integral formulation. The action at temperature $T = 1/(k_B\beta)$ is

$$\mathcal{S} = \frac{1}{2\beta} \sum_n \sum_{\mathbf{k}} Z^T_{-\mathbf{k},-\omega_n} \left[G_{\mathbf{k}} + (i\omega_n)\Gamma \right] Z_{\mathbf{k},\omega_n}, \tag{4.14}$$

where $\omega_n = \frac{2\pi n}{\beta}$ is the Matsubara frequency, where we have defined $Z^T = \begin{pmatrix} X^T & Y^T \end{pmatrix}$,

$$G_{\mathbf{k}} = 2 \begin{pmatrix} A_{\mathbf{k}} & C_{\mathbf{k}} \\ C_{\mathbf{k}}^T & B_{\mathbf{k}} \end{pmatrix} \quad \text{and} \quad \Gamma = \begin{pmatrix} 0 & -i\mathbf{1}_4 \\ i\mathbf{1}_4 & 0 \end{pmatrix} \tag{4.15}$$

($\mathbf{1}_4$ is the four-by-four identity matrix). As usual, the *real frequency* dispersion relations $\omega(\mathbf{k})$ are found by solving the zero eigenvalue equations of the matrix $G_{\mathbf{k}}+\omega\Gamma$. Here, these are equivalently the (both zero and non-zero) eigenvalues of $-\Gamma G_{\mathbf{k}}$.

We calculate the inelastic structure factor (to which the intensity $I(\mathbf{k}, \omega)$ of the scattering is proportional) obtained from the moment-moment correlation function,[27]

$$S(\mathbf{k}, \omega) = \sum_{\mu,\nu} \left[\delta_{\mu\nu} - (\hat{\mathbf{k}})_\mu (\hat{\mathbf{k}})_\nu\right] \sum_{a,b} \langle m_a^\mu(-\mathbf{k}, -\omega) m_b^\nu(\mathbf{k}, \omega)\rangle, \tag{4.16}$$

where $\hat{\mathbf{k}}$ is the unit vector associated with $\mathbf{k}$, $m_a^\mu(\mathbf{k}, \omega) = \mu_B \sum_\kappa g_a^{\mu\kappa} S_a^\kappa(\mathbf{k}, \omega)$ is the moment at momentum $\mathbf{k}$ and real frequency ω on the $a = 0, .., 3$ sublattice in direction $\mu = x, y, z$, and S_a^κ is, as usual, the κth coordinate of the effective spin-1/2 spin at site a. $\mathcal{F}_{\mu\nu}(\mathbf{k}) = \delta_{\mu\nu} - (\hat{\mathbf{k}})_\mu (\hat{\mathbf{k}})_\nu$ selects the component of the spin-spin correlations perpendicular to the scattering vector,[27] and $\mathcal{G}_{ab}^{\mu\nu}(\mathbf{k}, \omega) = \langle m_a^\mu(-\mathbf{k}, -\omega) m_b^\nu(\mathbf{k}, \omega)\rangle$ is the moment-moment correlation function that originates from the interaction between the neutrons' moment and the spins' moments, which we find to be

$$\mathcal{G}_{ab}^{\mu\nu} = -\pi s \eta_a^\mu \eta_b^\nu \sum_\alpha \delta(\omega - \epsilon_\alpha) \frac{1}{\psi_{R,\alpha}^\dagger \Gamma \psi_{R,\alpha}} \left([\psi_{R,\alpha}^\dagger]_a [\psi_{R,\alpha}]_b \right), \tag{4.17}$$

where δ is the Dirac distribution, $\eta_a^\mu = \sum_{\kappa=x,y,z} g_a^{\mu\kappa} \begin{pmatrix} v_a^\kappa & w_a^\kappa \end{pmatrix}$, ϵ_α is the αth eigenvalue of $-\Gamma G$, and $\psi_{R,\alpha}$ is its corresponding "right" eigenvector, i.e. such that $-\Gamma G \cdot \psi_{R,\alpha} = \epsilon_\alpha \, \psi_{R,\alpha}$. Also note that the momentum and frequency dependences are implied everywhere to be $\mathbf{k}, \omega$.

Now we estimate the amplitude of quantum fluctuations using our spin wave theory, by evaluating the quantum moment reduction in zero field and at zero temperature. In the Holstein-Primakoff boson language the reduction of the spin expectation value from the classical value of 1/2, averaged over the four site basis, is $r = \frac{1}{4} \sum_{a=0}^{3} \langle 0 | n_a | 0 \rangle$, where $\langle 0 | n_a | 0 \rangle$ indicates a ground state quantum expectation value. Evaluating this using the path integral method, we obtain $r = \frac{1}{8} \int_{\mathbf{k},\omega} \mathrm{Tr} \, \langle [G_\mathbf{k} + \omega \Gamma]^{-1} \rangle - \frac{1}{2}$, i.e.

$$r = \frac{1}{8} \int_\mathbf{k} \sum_\alpha \Theta(\epsilon_\alpha) \frac{\psi_{R,\alpha}^\dagger \psi_{R,\alpha}}{\psi_{R,\alpha}^\dagger \Gamma \psi_{R,\alpha}} - \frac{1}{2} \approx 0.05 \tag{4.18}$$

(Θ is the usual Heaviside distribution), which is a 10% reduction compared with the classical value of 1/2.

4.D Further Details of Experimental Data and Fits

The inelastic neutron scattering data (rows 1 and 3 in Figure 4.1) contains several features worth commenting on further. First, the darkest blue areas do not contain any data, either for kinematic reasons near $\mathbf{Q} = (0, 0, 0)$, or because of the finite angular extend of the scan. Second, at $E = 0$ one observes intensity which is due to coherent and incoherent elastic scattering from the sample, and hence is more intense than the inelastic features by up to several orders of magnitude, thus appearing red (off scale). Third, near the $(0, 0, 0)$ position there is higher background leading to unphysical intensities due to contamination from the un-scattered incident beam. This is observable in the HHH and HH0 data sets near the zero position.

The data sets were collected by counting for 8 minutes per angular rotation of the sample. The total time per magnetic field setting was about 12 hours.

Figure 4.4 shows the dispersions obtained from the fitting procedure overplotted on the data. These fits were accomplished by digitizing the shape of the dispersion from the experimental data, and performing a least squares minimization routine to match it. Intensities were calculated based on the spin wave theory using the extracted exchange parameters, and were not fit to the data. The 5D parameter space (four exchange plus one g-tensor parameter) was explored using a uniform search technique with the resulting excellent description obtained (Figure 4.1).

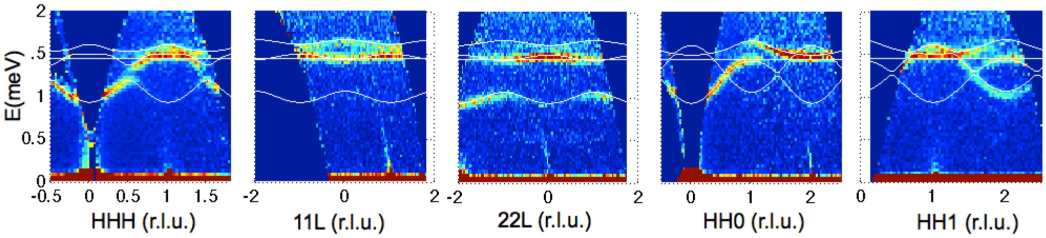

Figure 4.4: Color) Dispersions (white curves) obtained from the fitting procedure over-plotted on the data at $H = 5\,\mathrm{T}$.

4.E Features of the Spin Wave Spectrum

The spectra of Figure 4.1 are very rich. Because of the many parameters and of the presence of *classical* phase transitions (there are several ground states to the classical model), it is very difficult to track which features are due to what terms of Eq. (4.4). One remarkable feature which can be easily identified throughout most of phase space (including the region around which Eq. (4.3) places $\mathrm{Yb_2Ti_2O_7}$) is a quasi-flat band. Specifically, one spin wave mode is completely dispersionless in the plane of reciprocal space with $k_x = k_y$, i.e. normal to the magnetic field direction and passing through the origin in reciprocal space. All scattering measurements on $\mathrm{Yb_2Ti_2O_7}$ have been taken in this plane, so this feature is quite significant in the experiments. In the region of phase space around $\mathrm{Yb_2Ti_2O_7}$ and for $H = 5\,\mathrm{T}$, we find its energy to be, numerically, in meV:

$$E_{\mathrm{2d\,flat}} \approx 0.74 + 0.51\, J_{zz} - 1.18\, J_{\pm} - 3.11\, J_{\pm\pm} - 5.81\, J_{z\pm}, \tag{4.19}$$

where the J_α's must be input in meV, and which for our fit gives $E_{\mathrm{2d\,flat}}^{\mathrm{Yb_2Ti_2O_7}} \approx 1.45\,\mathrm{meV}$. Note that the energy of this feature is most sensitive to $J_{z\pm}$.

Moreover, we observe the following trends in the region around $Yb_2Ti_2O_7$:

- as $|J_{z\pm}|$ increases, all bands go up in energy (especially the two-dimensional flat one),

- increases in $J_{\pm}$ and $J_{\pm\pm}$ seem to have more or less the same effect: the bands get closer, and this happens in particular because the energy of the top bands decreases.

4.F Mean Field Theory Calculation

The Curie-Weiss mean field Hamiltonian obtained from Eq. (4.1) takes the form

$$\begin{aligned} H_{\mathrm{MF}} &= \sum_{\langle i,j \rangle} \sum_{\mu,\nu} J_{ij}^{\mu\nu} \left(\langle S_i^\mu \rangle S_j^\nu + S_i^\mu \langle S_j^\nu \rangle - \langle S_i^\mu \rangle \langle S_j^\nu \rangle \right) \\ &\quad - \mu_B H^\mu \sum_i g_i^{\mu\nu} S_i^\nu, \end{aligned} \tag{4.20}$$

where H^μ is the magnetic field in the μ direction, $\langle S_i^\mu \rangle$ is the mean field quantum thermal expectation value of S_i^μ, defined by $\langle S_i^\mu \rangle = \frac{1}{Z} \mathrm{Tr}\, S_i^\mu \exp(-\beta H_{\mathrm{MF}})$, where β is the inverse temperature $\beta = 1/(k_B T)$, where k_B is the Boltzmann constant and Z is the partition function $Z = \mathrm{Tr}\, \exp(-\beta H_{\mathrm{MF}})$. The traces are taken over the up and down spin states of every spin.

The ground state does not enlarge the unit cell at zero temperature, and we assume this is still the case at non-zero temperature. Thus, we define, for every sublattice a and every axis μ the average magnetization

$$m_a^\mu = \langle S_{t,a}^\mu \rangle, \tag{4.21}$$

which is the same for every tetrahedron t, which can be either "up" or "down". We arrive at the twelve consistency equations

$$\mathbf{m}_a = -\frac{\mathbf{h}_a^{\text{eff}}}{2\|\mathbf{h}_a^{\text{eff}}\|} \tanh \frac{\beta \|\mathbf{h}_a^{\text{eff}}\|}{2}, \tag{4.22}$$

where $\mathbf{h}_a^{\text{eff}} = 2\sum_b \mathbf{m}_b \cdot \mathbf{J}_{ba} - \mu_B \mathbf{H} \cdot \mathbf{g}_a$; the free energy per site is

$$f = -\frac{1}{4}\sum_{a,b} \mathbf{m}_a \cdot \mathbf{J}_{ab} \cdot \mathbf{m}_b - \frac{1}{4\beta}\sum_a \ln\left[2\cosh\frac{\beta\|\mathbf{h}_a^{\text{eff}}\|}{2}\right]. \tag{4.23}$$

We solve Eqs. (4.22) numerically, choosing the solution which minimizes the free energy in Eq. (4.23). With the field oriented along the [110] direction, we find the phase diagram shown in Figure 4.5, which contains two phases. In zero field, the low temperature phase is a ferromagnet with net magnetization along any of the $\langle 100 \rangle$ axes. In low fields, this expands into a phase in which the average magnetization is *not* aligned with the field, but lies within a $\{001\}$ plane. On increasing fields, a transition occurs to the high field state in which the net magnetization is aligned with the applied field, and no symmetries are spontaneously broken. This state is continuously connected to the high temperature paramagnetic phase.

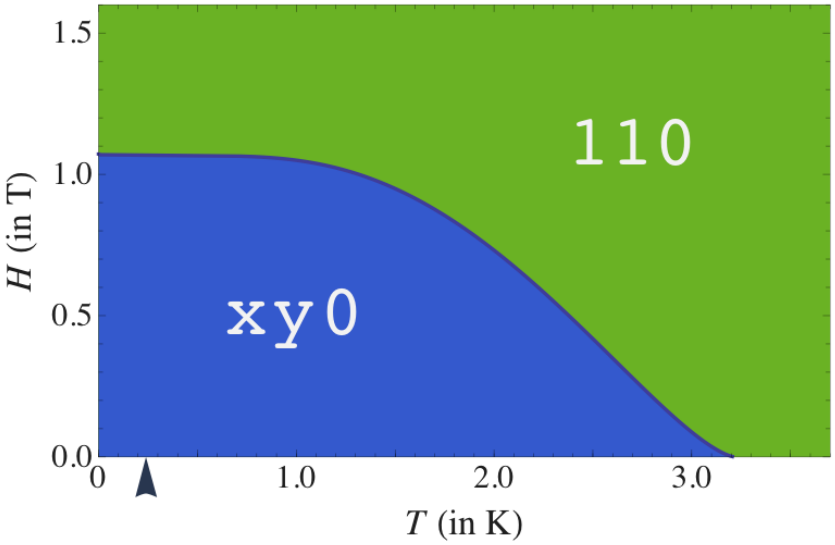

Figure 4.5: Color) Field versus temperature phase diagram obtained from a mean-field analysis of the Hamiltonian of Eq. (4.1), for a field **H** parallel to the [110] direction and with the exchange constant values obtained with our fits, Eq. (4.3). The system displays a net magnetic moment throughout the (H, T) plane. The blue region denotes a region where the total magnetization lies in the xy plane, and the green region is the paramagnetic phase; the two zones are separated by a continuous transition. In zero field, this transition takes place at $T_c^{MF} = 3.2\,\mathrm{K}$. At zero temperature, the amplitude of the transition field is $H_c^{MF} = 1.1\,\mathrm{T}$. The dark blue arrow shows the experimentally reported transition temperature of 240 mK: the actual transition occurs at a much lower temperature than that predicted by mean-field theory T_c^{MF}.

4.G Perturbation Theory

We show that the $U(1)$ QSL described by Hermele *et al.*[13, 23] is stable to the addition of the terms in the symmetry-obtained Hamiltonian Eq. (4.4), provided all coupling constants are small with respect to the Ising exchange parameter J_{zz}. In other words, we show that the $U(1)$ QSL exists in a finite region of parameter space, specifically where $J_{\pm}$, $J_{z\pm}$ and $J_{\pm\pm}$ are small with respect to J_{zz}.

In that limit, one may apply perturbation theory. When $J_{zz} > 0$, the ground state manifold of the unperturbed Hamiltonian is the extensively degenerate "two-in-two-out" manifold. When $J_{z\pm} = J_{\pm\pm} = 0$, Eq. (4.4) can be mapped exactly onto the Hamiltonian of Ref. [13], where the first non-vanishing and non-constant term in perturbation theory (above the "two-in-two-out" manifold) was shown to be third order in $J_{\pm}/J_{zz}$:

$$H_{\text{ring}}^{\text{eff}} = -K \sum_{\{i,j,k,l,m,n\}=\hexagon} \left(\mathsf{S}_i^+\mathsf{S}_j^-\mathsf{S}_k^+\mathsf{S}_l^-\mathsf{S}_m^+\mathsf{S}_n^- + \text{h.c.}\right), \tag{4.24}$$

where $K = \frac{12J_{\pm}^3}{J_{zz}^2}$ is a ring exchange interaction. $H_{\text{ring}}^{\text{eff}}$ flips the spins on the "flippable" hexagons, i.e. those with alternating up and down spins, and yields zero otherwise. This represents a ring move responsible for favoring the quantum superpositions of the $U(1)$ QSL. As shown in Refs. [13, 23, 28], this ring Hamiltonian has as its ground state a $U(1)$ QSL, whose low energy physics is described as the Coulomb phase of a $U(1)$ gauge theory. This phase is locally stable to *all* perturbations[13] in three dimensions, which is enough already to guarantee the persistence of the QSL state when the other exchange couplings are sufficiently small, i.e. when the induced terms in the effective Hamiltonian are much smaller than the ring coupling K.

We can, however, go further and consider these effects explicitly in the perturbative limit, which extends the discussion to the case when $J_{z\pm}, J_{\pm\pm} \ll J_{zz}$ but with no particular assumptions placed upon the magnitude of the induced terms in the effective Hamiltonian relative to K. When $J_{z\pm}$ or $J_{\pm\pm}$ are non-zero, other "non-ring" effective Hamiltonians are allowed. In particular, the

$J_{z\pm}$ term gives rise to an effective third neighbor ferromagnetic Ising Hamiltonian:

$$H^{\mathrm{eff}}_{\mathrm{3rd\,Ising}} = -J_{(3)} \sum_{\langle\langle\langle i,j\rangle\rangle\rangle} \mathsf{S}^z_i \mathsf{S}^z_j, \tag{4.25}$$

where $J_{(3)} = \frac{3J^2_{z\pm}}{J_{zz}}$. This term alone has six symmetry-related ordered ground states. Each of them consists of the choice of one of the six two-in-two-out tetrahedra, with the *same* pattern repeated on each "up" tetrahedron (these states are magnetic with their moment along the $\langle 100\rangle$ directions) and contain no flippable hexagons, see Figure 4.6.

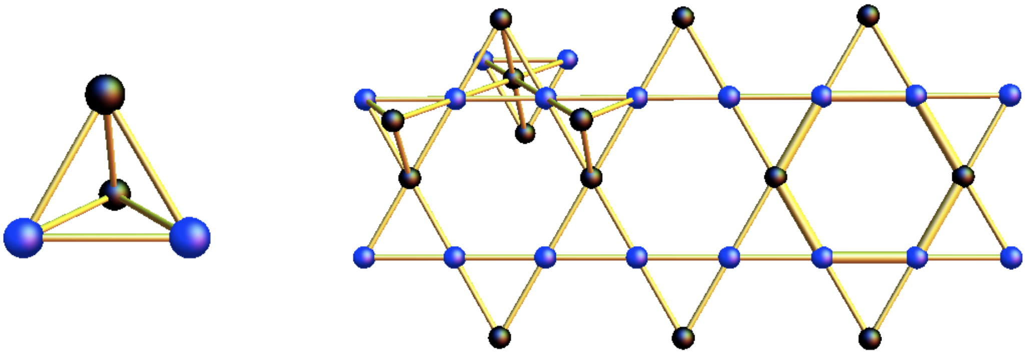

Figure 4.6: Color) One of the six ground states of $H^{\mathrm{eff}}_{\mathrm{3rd\,Ising}} = -\frac{3J^2_{z\pm}}{J_{zz}} \sum_{\langle\langle\langle i,j\rangle\rangle\rangle} \mathsf{S}^z_i \mathsf{S}^z_j$. A blue sphere represents an "in" spin while a black sphere represents an "out" one. Because two of the four chain types contain *non*-alternating spins, there are no flippable hexagons in any of the six (equivalent) ground states.

This implies that states which contain flippable hexagons represent an energy cost. We can therefore consider, $H^{\mathrm{eff}}_{\mathrm{3rd\,Ising}}$ as an analog of the Rokhsar-Kivelson term introduced by Hermele *et al.*,[24, 13] $H_{RK} = VN_{\mathrm{f}}$, where N_{f} is the operator that counts the number of flippable hexagons. This term actually *stabilizes* the QSL state[13, 28]. In particular, the QSL phase grows in stability as V is increased from zero up to the point $V = K$, beyond which (for $V > K$), the system undergoes a first order transition to a degenerate set of classical unflippable states, which includes the six ordered $\langle 100 \rangle$ ferromagnetic ground states described above.

In the case relevant here, when $J_{(3)}/K$ is sufficiently large, the system must undergo a transition to the unflippable $\langle 100 \rangle$ ground states. Since this model and the RK one of Ref. [13] agree on the phases both when $J_{(3)} \ll K$ and when $J_{(3)} \gg K$, it is natural to expect that the intervening phase diagram coincides in the two models as well. Therefore we expect that the QSL state is maximally stable when $J_{(3)}/K$ takes some value of $O(1)$. (For the values of the exchange constants given by our fits we find $J_{(3)}/K = \frac{J_{z\pm}^2 J_{zz}}{4J_{\pm}^3} = 6.2$, but we caution that this is probably outside the perturbative regime). We note in passing that the $J_{(3)}$ exchange can also be expressed in terms of purely plaquette interactions, which might allow further analytical connection to the RK theory. We will not, however, pursue this further here.

Inclusion of the other coupling $J_{\pm\pm}$, higher order effects, and cross terms amongst the exchange couplings does not lead to any new effects. Indeed, all the associated terms in the effective Hamiltonian assume a ferromagnetic or ring form, and can be subsumed in the above couplings. They are also higher order in J_α/J_{zz}, $\alpha = \pm, z\pm, \pm\pm$.

4.H Comparison between our Exchange Constants and those of Thompson *et al.*[10]

The correspondence between our effective spin-1/2 operators $\mathbf{S}_i$ in Eq. (4.1) and the full 7/2-angular-momentum operators $\mathbf{J}_i$ used by Thompson *et al.* in Ref. [10] is given by projecting the full angular momentum into the ground state Kramer's doublet

$$P_{1/2}\,\mathbf{J}_i\,P_{1/2} = \frac{\mathbf{g}_i \cdot \mathbf{S}_i}{g_J}, \tag{4.26}$$

where $P_{1/2}$ is the projection operator to the ground state Kramer's doublet, and $g_J = 8/7$ is the Landé factor.

We use $g_{xy}/g_z = 2.4$ and $g_z = 1.79$ for concreteness, but the results do not depend too much upon the details of this choice within the range of parameters found in the literature. With this choice, we find that the semi-formal relations between our parameters and those given in Ref. [10] are

$$\begin{aligned}
J_1 &= 0.818\,\mathcal{J}_{\text{Ising}} - 9.08\,\mathcal{J}_{\text{iso}} - 1.21\,\mathcal{J}_{\text{pd}} - 2.34\,\mathcal{J}_{\text{DM}} \\
J_2 &= -0.818\,\mathcal{J}_{\text{Ising}} - 8.03\,\mathcal{J}_{\text{iso}} - 11.2\,\mathcal{J}_{\text{pd}} + 6.16\,\mathcal{J}_{\text{DM}} \\
J_3 &= 0.818\,\mathcal{J}_{\text{Ising}} + 4.88\,\mathcal{J}_{\text{iso}} + 12.7\,\mathcal{J}_{\text{pd}} - 2.34\,\mathcal{J}_{\text{DM}} \\
J_4 &= 0.818\,\mathcal{J}_{\text{Ising}} - 0.523\,\mathcal{J}_{\text{iso}} - 5.49\,\mathcal{J}_{\text{pd}} + 5.62\,\mathcal{J}_{\text{DM}}.
\end{aligned}$$

For $\mathcal{J}_{\text{Ising}} = 6.98\ 10^{-2}\,\text{meV}$, $\mathcal{J}_{\text{iso}} = 1.90\ 10^{-2}\,\text{meV}$, $\mathcal{J}_{\text{pd}} = -2.50\ 10^{-2}\,\text{meV}$ and $\mathcal{J}_{\text{DM}} = -2.33\ 10^{-2}\,\text{meV}$ as calculated by Thompson *et al.* in Ref. [10], we obtain $J_1 = -0.03\,\text{meV}$, $J_2 = -0.07\,\text{meV}$, $J_3 = -0.11\,\text{meV}$ and $J_4 = 0.05\,\text{meV}$, or, in the formulation of Eq. (4.4), $J_{zz} = 1.9\ 10^{-4}\,\text{meV}$, $J_{\pm} = 3.0\ 10^{-3}\,\text{meV}$,

$J_{\pm\pm} = 3.8\ 10^{-2}\,\mathrm{meV}$ and $J_{z\pm} = -6.4\ 10^{-2}\,\mathrm{meV}$. These values are rather different from those found in our fits, Eq. (4.3) and Eq. (4.5), and indeed yield spin wave spectra in strong disagreement with experiment. In principle, one resolution of the difference could be that the exchange couplings are actually strongly temperature dependent, and distinctly different in the temperature range studied in Ref. [10] and at the low temperatures studied here. Such a change in exchange parameters could conceivable occur if the transition observed at 214-240mK had a substantial structural component. However, we do not have any a priori reason to suspect this. In any case, it would be very interesting to resolve the differences between the two exchange models.

4.9 * References

[1] J. S. Gardner, M. J. P. Gingras, and J. E. Greedan, Rev. Mod. Phys. **82**, 53 (2010).

[2] S. T. Bramwell and M. J. P. Gingras, Science **294**, 1495 (2001).

[3] J. P. Clancy, J. P. C. Ruff, S. R. Dunsiger, Y. Zhao, H. A. Dabkowska, J. S. Gardner, Y. Qiu, J. R. D. Copley, T. Jenkins, and B. D. Gaulin, Phys. Rev. B **79**, 14408 (2009).

[4] C. Castelnovo, R. Moessner, and S. L. Sondhi, Nature **451**, 42 (2008).

[5] T. Fennell, P. P. Deen, A. R. Wildes, K. Schmalzl, D. Prabhakaran, A. T. Boothroyd, R. J. Aldus, D. F. McMorrow, and S. T. Bramwell, Science **326**, 415 (2009).

[6] L. D. C. Jaubert and P. C. W. Holdsworth, Nature Physics **5**, 258 (2009).

[7] S. H. Curnoe, Phys. Rev. B **78**, 094418 (2008).

[8] H. R. Molavian, M. J. P. Gingras, and B. Canals, Phys. Rev. Lett. **98**, 157204 (2007).

[9] J. D. Thompson, P. A. McClarty, and M. J. P. Gingras, J. Phys. : Condens. Matter. **23**, 164219 (2011).

[10] J. D. Thompson, P. A. McClarty, H. M. Rønnow, L. P. Regnault, A. Sorge, and M. J. P. Gingras, Phys. Rev. Lett. **106**, 187202 (2011).

[11] J. A. Hodges, P. Bonville, A. Forget, M. Rams, K. Królas, and G. Dhalenne, J. Phys. : Condens. Matter **13**, 93019310 (2001).

[12] B. Canals and C. Lacroix, Phys. Rev. Lett. **80**, 2933 (1998).

[13] M. Hermele, M. P. A. Fisher, and L. Balents, Phys. Rev. B **69**, 064404 (2004).

[14] L. Balents, Nature **464**, 199 (2010).

[15] J. A. Hodges, P. Bonville, A. Forget, A. Yaouanc, P. Dalmas de Réotier, G. André, M. Rams, K. Królas, C. Ritter, P. C. M. Gubbens, C. T. Kaiser, P. J. C. King, and C. Baines, Phys. Rev. Lett. **88**, 077204 (2002).

[16] K. A. Ross, J. P. C. Ruff, C. P. Adams, J. S. Gardner, H. A. Dabkowska, Y. Qiu, J. R. D. Copley, and B. D. Gaulin, Phys. Rev. Lett. **103**, 227202 (2009).

[17] H. B. Cao, A. Gukasov, I. Mirebeau, and P. Bonville, J. Phys. : Condens. Matter **21**, 492202 (2009).

[18] S. Onoda, arXiv:1101. 1230v1 (2011).

[19] J. S. Gardner, B. D. Gaulin, and D. M. Paul, Journal of Crystal Growth **191**, 740 (1998).

[20] H. W. J. Blöte, R. F. Wielinga, and W. J. Huiskamp, Physica **43**, 549 (1969).

[21] Y. Yasui, M. Soda, S. Iikubo, M. Ito, M. Sato, N. Hamaguchi, T. Matsushita, N. Wada, T. Takeuchi, N. Aso, and K. Kakurai, Journal of the Physical Society of Japan **72**, 3014 (2003).

[22] J. S. Gardner, G. Ehlers, N. Rosov, R. W. Erwin, and C. Petrovic, Phys. Rev. B **70**, 180404 (2004).

[23] A. Banerjee, S. V. Isakov, K. Damle, and Y. B. Kim, Phys. Rev. Lett. **100**, 047208 (2008).

[24] D. S. Rokhsar and S. A. Kivelson, Phys. Rev. Lett. **61**, 2376 (1988).

[25] T. Senthil, A. Vishwanath, L. Balents, S. Sachdev, and M. P. A. Fisher, Science **303**, 1490 (2004).

[26] D. L. Bergman, G. A. Fiete, and L. Balents, Phys. Rev. B **73**, 134402 (2006).

[27] G. L. Squires, *Introduction to the Theory of Thermal Neutron Scattering* (Cambridge University Press, Cambridge, 1978).

[28] N. Shannon, O. Sikora, F. Pollmann, K. Penc, and P. Fulde, Arxiv preprint arXiv:1105. 4196 (2011).

Chapter 5

Structural Defects in $Yb_2Ti_2O_7$

This chapter incorporates the preprint *"Single crystals of* $Yb_2Ti_2O_7$ *grown by the Optical Floating Zone technique: naturally "stuffed" pyrochlores?"*, which will appear in Physical Review B.

This paper addresses the sample-dependence issue that was raised in Chapter 3 in the context of the low temperature magnetic specific heat. The experiments done here compare the chemical structure of a single crystal of $Yb_2Ti_2O_7$ to a sintered powder sample. This was accomplished by pulverising the single crystal and performing a powder neturon diffraction experiment on both samples. The single crystal is grown in an identical manner to that used in the neutron scattering sudies presented in the earlier chapters, and is expected to be a good indicator for the type of disorder generally present in single crystals of $Yb_2Ti_2O_7$ grown by the floating zone method.

This work has shown that oxygen non-stoichiometry is not enough to explain the differences in the observed powder diffraction patterns. The best model is a "stuffed" pyrochlore model, with 2.3% of the titanium atoms replaced by ytterbium. These extra moments appear to create a slightly more anti-ferromagnetic exchange interaction over all, as indicated by susceptibility measurements. The work presented here is the first detailed structural investigation of single crystals of $Yb_2Ti_2O_7$, and is expected to be a benchmark in the effort to improve the crystal quality enough to recover a single, sharp specific heat anomaly at 265mK, as observed in the best powder samples. Future studies of such a crystal could resolve the longstanding controversy over the nature of the ground state in $Yb_2Ti_2O_7$.

5.1 Single crystals of $Yb_2Ti_2O_7$ grown by the Optical Floating Zone technique: naturally "stuffed" pyrochlores?

Kate A. Ross,[1] Thomas Proffen,[2,3] Hanna A. Dabkowska,[4] Jeffery A. Quilliam,[5,6,7], Luke R. Yaraskavitch,[5,6], Jan B. Kycia,[5,6], Bruce D. Gaulin,[1,4,8]

[1] *Department of Physics and Astronomy, McMaster University, Hamilton, Ontario, L8S 4M1, Canada*
[2] *Los Alamos National Laboratory, Los Alamos, New Mexico 87545, USA*
[3] *Spallation Neutron Source, Experimental Facilities Division, Oak Ridge National Laboratory, P.O. Box 2008, Oak Ridge, TN 37831, USA*
[4] *Brockhouse Institute for Materials Research, McMaster University, Hamilton, Ontario, L8S 4M1, Canada*
[5] *Department of Physics and Astronomy and Guelph-Waterloo Physics Institute, University of Waterloo, Waterloo, ON, N2L 3G1, Canada*
[6] *Institute for Quantum Computing, University of Waterloo, Waterloo, ON, N2L 3G1, Canada*
[7] *Laboratoire de Physique des Solides, Universit Paris-Sud 11, UMR CNRS 8502, F-91405 Orsay, France*
[8] *Canadian Institute for Advanced Research, 180 Dundas St. W., Toronto, Ontario, M5G 1Z8, Canada*

Abstract

Recent neutron scattering and specific heat studies on the pyrochlore $Yb_2Ti_2O_7$ have revealed variations in its magnetic behavior below 265mK. In the best samples, a sharp anomaly in the specific heat is observed at T=265mK. Other samples, especially single crystals, have broad features in the specific heat which vary in sharpness and temperature depending on the sample, indicating that the magnetic ground state may be qualitatively different in such samples. We performed detailed comparisons of the chemical structure of a pulverised single crystal of $Yb_2Ti_2O_7$, grown by the floating zone technique, to a sintered powder sample of $Yb_2Ti_2O_7$. Rietveld refinements of neutron

powder diffraction data on these samples reveal that the crushed single crystal is best described as a "stuffed" pyrochlore, $Yb_2(Ti_{2-x}Yb_x)O_{7-x/2}$ with $x = 0.046(4)$, despite perfectly stoichiometric starting material. Substituting magnetic Yb^{3+} on the non-magnetic Ti^{4+} sublattice would introduce random exchange bonds and local lattice deformations. These are expected to be the mechanism leading to of the variation of the delicate magnetic ground state of $Yb_2Ti_2O_7$. Determination of the cubic cell length, a, could be useful as a method for characterizing the stoichiometry of non-pulverised single crystals at room temperature.

5.1.1 Introduction

The rare-earth titanate series of compounds, $R_2Ti_2O_7$, has been essential in furthering the understanding of geometrically frustrated magnetism over the past two decades. Compounds in this series, in which R stands for a trivalent rare earth (RE) ions, form perfect magnetic pyrochlore sublattices. The pyrochlore lattice lends itself to studies of geometric frustration since it consists of corner-sharing tetrahedra. The geometrical constraints imposed by this tetrahedral array frustrate near-neighbor magnetic interactions, coaxing rich behavior from even the simplest models for the spin Hamiltonian.[1] The rare earth titanates are realizations of this magnetic lattice where one has several choices of RE ions available, from Sm to Lu.[2] This choice introduces sufficient variability of the strongest terms in the spin Hamiltonians (such as single-ion anisotropy, dipolar interactions, and sign of exchange interactions) that a broad range of exotic magnetic behaviour has been observed across the series.[3] Furthermore, the relatively straightforward synthesis of large single crystals of these compounds, amenable to directionally dependent studies such as neutron scattering, has made them invaluable to the experimental side of the field.

The synthesis of large single crystals of many compounds in this series can be accomplished by the optical floating zone (OFZ) method.[4,5,6,7] Aside from producing very large crystals (cylindrical in shape, with lengths of about 3cm and diameters of 0.5cm), this method is desirable since it is expected to keep impurities in the growths to a minimum by avoiding the use of a crucible. Further, for congruently melting compounds such as the $R_2Ti_2O_7$ series, the chemical composition of the crystal is expected to stay constant, and identical to the starting material, over the length of the growth. Despite these benefits, recent studies have shown that there is some variability in the magnetic properties of single crystals of the same $R_2Ti_2O_7$ compound produced by this method. This has been observed in $Tb_2Ti_2O_7$, where the magnetic specific heat was shown to vary from sample to sample, particularly in the single crystals.[8,9,10] Since $Tb_2Ti_2O_7$ is known for its lack of long range magnetic ordering down to 50mK, maintaining a disordered ground state with cooperatively fluctuating magnetic moments,[11] the effect of this sample dependence is not manifested in the ground state properties in an immediately obvious way, though a small fraction of spins appear to "freeze" in some samples.[12,13,14] No work has been published that investigates the cause of this sample dependence in the single crystals, though a powder neutron diffraction study of a sintered powder found exact stoichiometry to within their experimental error of 2%.[15] We can assume that the sample dependence of the magnetic properties is the result of structural defects of some type which are so far uncharacterized in the single crystals, and are therefore uncontrolled.

More recently, the same issue of sample dependence has arisen in $Yb_2Ti_2O_7$, but with much more dramatic consequences. $Yb_2Ti_2O_7$ has long been an enigma when it comes to its magnetic ground state, which has been variously, and incompatibly, described as being long-range ordered in a collinear ferromagnetic (FM) state,[16,17] having non-collinear long range FM fluctuations,[18] or having short-range correlated fluctuations.[19,20,21] The specific heat of $Yb_2Ti_2O_7$ is particularly revealing. Some samples show sharp anomalies, with the sharpest and highest temperature anomaly observed so far being at

265mK in a powder sample prepared at McMaster University.[21] Other powder samples show slightly broader anomalies at lower temperatures; 250mK[22,23] and 214mK.[24] The single crystal samples grown by the OFZ method in several laboratories are even more variable, showing very broad humps instead of sharp anomalies ,[21,23,17] and in some cases show a mixture of both broad humps and sharp peaks.[21] The loss of the extremely sharp specific heat anomaly, which signals a magnetic phase transition, likely means that some of the samples do not reach the ground state that would occur in a nominally "perfect" sample.

Initial work on an effective Hamiltonian to describe $Yb_2Ti_2O_7$ was performed by Thompson *et al*, who extracted four independent exchange parameters from fits to the single crystal diffuse magnetic neutron scattering above the transition.[25] While these parameters describe the local susceptibility of the moments well,[26] they do not reproduce the spin wave excitations that were revealed in a neutron scattering study of single crystal $Yb_2Ti_2O_7$ in the presence of a high magnetic field applied along the [110] direction.[20] These spin wave excitations, which present stronger constraints on the effective Hamiltonian, have themselves been accurately modeled by a different set of anisotropic exchange parameters.[27] These parameters revealed spin-ice type exchange, i.e. FM exchange between the local $\langle 111 \rangle$ components of the spins at the Yb^{3+} sites, in addition to significant quantum fluctuations. $Yb_2Ti_2O_7$ can thus be thought of as a "quantum spin ice" material, an analog to the classical spin ice state found in $Ho_2Ti_2O_7$ and $Dy_2Ti_2O_7$[28] but with quantum dynamics allowing tunnelling between the many allowed spin ice ground states.[27,29,30,31] The precise location of $Yb_2Ti_2O_7$ on the four-exchange-parameter phase diagram of the S=1/2 anisotropic exchange model for the pyrochlore lattice is still unknown, but it appears to be close to the predicted Coulombic Quantum Spin Liquid (QSL) phase that is expected to remain disordered and support exotic emergent excitations such as magnetic monopoles.[32] Another likely possibility is a simple FM ordered phase which is nearby in the phase diagram.[32] This proximity to the phase boundary may mean that small perturbations to the exchange parameters, even locally, could induce a significant change in its ground state.

The body of work on $Yb_2Ti_2O_7$ contains the following information on the sample dependence and the nature of the ground state:

- Powder samples tend to have a single specific heat anomaly, variable in both sharpness and temperature, reported to occur between 214mK and 265mK.[24,22,23,21]

- Single crystal samples tend to have broad humps in the specific heat.[23,21]

- A powder sample with a fairly sharp specific heat anomaly at T=250mK[22] shows a first-order drop in spin flucutation frequency, but remains dynamic below this transition and does not show signs for long-range order.[19]

- A single crystal sample with both a broad hump in the specific heat at 200mK and a sharp anomaly at 265mK shows a dynamic, short-range three-dimensionally correlated ground state that emerges from a short range two-dimensionally correlated state for $T \geq 400$mK.[21]

- One crystal has been reported to have a single, somewhat-sharp specific heat anomaly at 240mK. This crystal shows some signs of a simple, almost-collinear FM ground state that emerges from a two-dimensionally correlated state that exists above the transition temperature.[16,17]

Because the single crystal samples show variable, broad, and lower temperature specific heat features, one is lead to suspect that structural disorder is present in those samples to a higher degree than in the powders. It is quite likely that these structural defects are small in number, since the growth conditions are well-known and repeatable, and investigation of the structures reveals perfectly ordered and stoichiometric compounds at first glance.[21] Nevertheless, even small numbers of defects have the potential to cause significant changes in frustrated systems by disrupting the inherent delicate balance of energy scales present therein. This may be particularly true for $\mathrm{Yb_2Ti_2O_7}$ since it appears to be near a boundary in its exchange interaction phase diagram, as discussed above. Therefore, we must look more closely at the structures of the single crystals, and at the possibility of subtle structural defects, to try to understand what implications they have for the magnetism in this material. In the end, our goal should be to be able to characterize the level of such defects, which will allow us to systematically study their effects, since we must accept that real materials are never ideal.

With this goal in mind, we performed powder neutron diffraction experiments on two samples of $\mathrm{Yb_2Ti_2O_7}$. One sample is a sintered powder prepared identically to the starting material used in the OFZ growth of the single crystal. Another powder sample prepared in this way has been shown to have the sharpest and highest temperature specific heat anomaly reported in the literature to date (this is reproduced in Fig. 5.6).[21] The second sample is a single crystal grown by the OFZ method and then crushed (see Section 5.1.2 for details of the growth conditions). We find, using Rietveld refinements of the neutron powder diffraction data, that the crushed single crystal is accurately modeled by full occupation of Yb^{3+} ions on the Yb^{3+} site, and by a 2.3% substitution of Yb^{3+} ions on the Ti^{4+} sites.

It is well-known that the $R_2Ti_2O_7$ pyrochlore materials can accommodate extra (magnetic) R^{3+} ions on the (non-magnetic) Ti^{4+} sites, leading to what is known as a "stuffed" pyrochlore structure.[33,34] The Ti sites themselves form a pyrochlore lattice which is interpenetrating with the R sublattice (see Figure 5.1), and the nearest neighbor (n. n.) distance between Ti and R sublattices is equal to the n. n. distance between R atoms; approximately 3.6 Å.

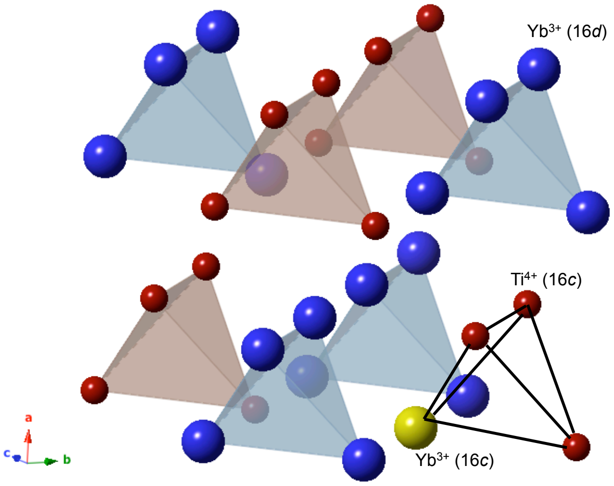

Figure 5.1: The pyrochlore lattice, showing only cation positions. The stuffed pyrochlores include some RE cations (magnetic Yb^{3+}) on the transition metal (non-magnetic Ti^{4+}) site. Here, this extra rare earth is shown in yellow. This introduces extra near-neighbor exchange at some RE sites.

Stuffing introduces an extra n.n. bond for some RE ions which has different exchange pathway due to different oxygen environment, and thus may be of different strength or even sign. This spatially random addition of a small number of exchange interactions, combined with the frustration already inherent in the system, could conceivably lead to a spin glass state. This is consistent with the observation of broad humps in the magnetic specific heat in some of the single crystal samples of $Yb_2Ti_2O_7$,[21,23] the formation of short range correlations with reduced fluctuation time scales,[19,21] and observed long-relaxation times[16] with multiple timescales of relaxation,[19] though no frequency-dependent ac susceptibility is reported at these low temperatures which could conclusively identify a spin glass transition. We note that the frustrated garnet system $Gd_3Ga_5O_{12}$ (GGG) is also naturally and unavoidably "stuffed" with 1-2% excess Gd on the Ga sites during crystal growth. This may also be the cause of the low-temperature unconventional glassiness that is observed in that system.[35,36]

There are reports of the magnetic properties of some stuffed rare-earth titanates with relatively high stuffing levels. The stuffed spin ices, $Ho_2(Ti_{2-x}Ho_x)O_{7-x/2}$ and $Dy_2(Ti_{2-x}Dy_x)O_{7-x/2}$ with $x = 0.3$ (i.e. 15% stuffing), show marked changes in spin dynamics compared to the unstuffed compounds, including the introduction of multiple timescales for relaxation,[37,38] and slower low temperature dynamics in the Dy compound[37], yet more persistent dynamics in the Ho compound.[39] There is evidence for a change in n.n. exchange interactions, from ferromagnetic (FM) in the unstuffed spin ices, to anti-ferromagnetic (AFM) in the stuffed spin ices with $x = 0.3$.[39,38,37]

In the Tb-based pyrochlores, a different type of disorder on the transition metal site has been investigated. $Tb_2Sn_2O_7$ is known to reach an unusual ground state below $T_c = 850$mK, consisting of both short- and long-range spin ordering,[40,41] while maintaining spin dynamics to the lowest measurable temperatures.[40,41,42] This is in contrast to the isostructural compound $Tb_2Ti_2O_7$, which shows no signs of long range order at any measurable temperature. Dahlberg *et al* have shown that 5% substitution of Ti for Sn in $Tb_2Sn_2O_7$ completely removes the transition to long range magnetic order.[43] This example shows that the rare-earth pyrochlores can be very sensitive to small concentrations of defects on the non-magnetic sublattice, even when these substitutions are themselves non-magnetic in nature.

The structure of several stuffed rare earth titanates has been studied in detail by Lau *et al*,[33,34] who found that for lightly stuffed compounds, one observes on average a pyrohclore structure. At higher levels of stuffing ($x = 0.3$) for small RE ions such as Yb^{3+}, one observes a transition to defect fluorite structure with short range correlated pyrochlore superstructure.[33] The lattice spacing of the cubic unit cell increases linearly with stuffing level, and has been characterized for several stuffed rare earth titanates including $Yb_2(Ti_{2-x}Yb_x)O_{7-x/2}$.[33] We have drawn on this previous work to identify signatures in our data which indicate that the stuffed model is appropriate to the crushed crystal only, and quantify it using Rietveld refinements. We further suggest that measurement of the room temperature lattice parameter is a viable method to ascertain the structural quality of single crystals of $Yb_2Ti_2O_7$ before performing further characterizations, such as low temperature specific heat.

5.1.2 Experimental Method

5.1.2.1 Materials preparation

Two samples of $Yb_2Ti_2O_7$ were studied by neutron powder diffraction. One was prepared by solid state reaction between pressed powders of Yb_2O_3 and TiO_2, sintered at 1200°C for 24 hours with warming and cooling rates of 100°C/h. A pressed powder prepared in this manner was also used as the starting material for the single crystal growth by the OFZ method. The principles of this method are described elsewhere.[4,5,6,44] The growth rate was 6mm/h, with a counter-rotation of the feed and seed rods of 30 rpm which encouraged thorough mixing of the molten zone. After the growth, no evaporated material was visually observed on the quartz tube that encloses the OFZ growth. The growth was performed under 4atm of oxygen pressure. Oxygen overpressure has previously been found to minimize oxygen non-stoichiometry in rare-earth titanates grown by the floating zone method.[7]

Both types of samples were then pulverised using a Pulverisette 2 mortar grinder, for 20 minutes per sample, to obtain loose powder samples. They are henceforth referred to as the "sintered powder" (SP), weighing 12.587g, and "crushed crystal"(CC), weighing 10.294g.

A second single crystal was prepared the same manner as described above, and a single slice of the crystal was annealed in flowing oxygen gas for 10 days, at 1050°C, with warming/cooling rates of 100°C/h. This sample was not pulverised and was used in specific heat measurements. Its lattice spacing was determined using a Huber four-circle x-ray diffractometer with an molybdenum anode. A second slice of of the same crystal was not annealed in order to compare its specific heat to the annealed piece.

5.1.2.2 Neutron powder diffraction

A neutron powder diffraction experiment was performed using the NPDF instrument at the Lujan Neutron Scattering Center at the Los Alamos National Laboratory. This instrument is located on a 32m flight path from the spallation target at the Lujan Center and has four banks of detectors, allowing the collection of high-resolution $S(Q)$ data ($\Delta Q/Q \sim 0.7\%$) over a Q range of 0.8 to 50Å^{-1}. The lowest temperature used in our data collection was 15K, which is well above both the Curie-Weiss temperature, $\Theta_{CW} \sim$ 800mK, and the temperature of the observed magnetic phase transition, $T_c =$ 265mK; hence, all information in the measured $S(Q)$ is expected to arise from nuclear (chemical) structure rather than from magnetic correlations.

5.1.2.3 Specific heat

The specific heat measurements were performed at the University of Waterloo using the quasi-adiabatic method (see Ref. 45 for details) with a 1 kΩ RuO_2 thermometer and 10 kΩ heater mounted directly on the thermally isolated sample. A weak thermal link to the mixing chamber of a dilution refrigerator was made using Pt-W (92% Pt, 8% W) wire for the annealed and non-annealed single crystal pieces (354.1mg and 361mg, respectively) and powder sample (24.37 mg). The time constant of relaxation provided by the weak link was several hours, much longer than the internal relaxation time of the samples, minimizing thermal gradients and ensuring that the sample cooled slowly into an equilibrium state. The addenda contributed less than 0.1% to the specific heat of the system. The data from the powder sample was previously published in Ref. 21.

5.1.3 Results

5.1.3.1 Rietveld refinements

Neutron powder diffraction data were collected over a temperature range from 15 to 250K for the sintered powder and crushed crystal samples. Representative data at T=15K are compared in Figure 5.2, which shows S(Q) as measured by the lowest angle bank of detectors in the NPDF instrument. Rietveld structural refinements were carried out using EXPGUI,[46] a graphical interface for the GSAS software package.[47] Note that in all refinements presented herein, all four banks of detectors are refined simultaneously, but only one is shown in the figures for clarity. All data sets were refined within the Fd$\overline{3}$m space group, which is appropriate for the rare-earth titanate pyrochlore materials. The positions of the ions and their Wyckoff positions are listed in Table 5.1. In the fully stoichiometric compound, both the magnetic Yb^{3+} ions and the Ti^{4+} ions form interpenetrating arrays of corner sharing tetrahedra (Fig. 5.1), which we call sublattices A and B. The Yb^{3+} ions, normally confined to sublattice A, are 8-fold coordinated, with six of the O^{2-} ions at the $48f$ positions and two at the $8b$ positions. The Ti^{4+} ions are 6-fold coordinated

Atom	Wyckoff position	fractional coordinates			Ideal occ.
Yb1	$16d$	0.500	0.500	0.500	1
Yb2	$16c$	0.000	0.000	0.000	0
Ti	$16c$	0.000	0.000	0.000	1
O1	$8b$	0.375	0.375	0.375	1
O2	$48f$	x	0.125	0.125	1

Table 5.1: Crystallographic sites used in the refinements. Their Wyckoff positions and fractional coordinates are given within the 2nd origin choice of the Fd$\overline{3}$m space group.

by O^{2-} ions at the $48f$ positions. The only free positional parameter in this structure belongs to the $48f$ oxygen ions.

In our refinements, the Atomic Displacement Parameters (ADPs) are allowed to take their full anisotropic forms, which are contstrained only by the point symmetry of the site in question. These constraints are laid out in Ref. 48. The ADPs represent the mean-squared displacement of the ions from their average positions. Thus, one expects them to increase as temperature increases, in order to account for thermal motion. The ADPs also include any *static* displacements, such as those due to local distortions from the ideal structure, which are averaged over all unit cells. For a stuffed pyrochlore, we should expect the ADPs for all ions to increase mildly due to local strain caused by the inclusion of the (relatively large) Yb ion at the Ti site, and the resulting oxygen vacancies required to maintain charge neutrality. We do observe increased ADPs for the crushed crystal for all refined models.

For both samples the structure refines quite well within the purely stoichiometric model, with combined R_{wp} (i.e. the "weighted profile R factor", a measure of the goodness of the fit which is ideally zero[49]) values for all detec-

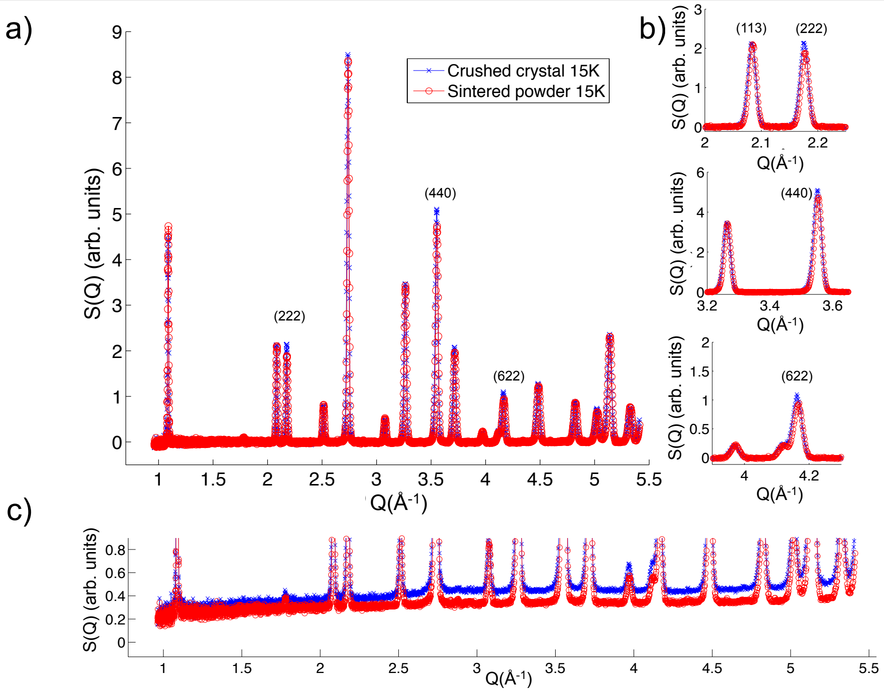

Figure 5.2: a) Powder neutron diffraction patterns at T=15K, obtained from a crushed single crystal and sintered powder. The backgrounds, which were fit to 4th order polynomials, have been subtracted to compare peak heights. Relative increases in $S(Q)$ are evident at the (222), (440) and (622) positions for the crushed crystal. These Bragg peaks are shown in more detail in b). There is an overall shift of the peak centers due to differences in lattice parameters, discussed in the text. c) The raw data at T=15K without a background subtraction, focusing on the diffuse background. The crushed crystal exhibits increased diffuse scattering.

tor banks between 4.0 and 4.8% (see Table 5.2). The crushed crystal refined in the stoichiometric model does give poorer fits, on the 0.4% level, compared to the sintered powder. Examining the raw data reveals subtle differences between the two types of samples, which indicate that the condition for exact stoichiometry in the crushed crystal should be relaxed. Examples of the raw neutron powder diffraction data are shown in Fig. 5.2, which have been normalized to the incident spectrum and have diffuse backgrounds subtracted in panels a) and b). Figure 5.2 a) shows that the relative intensities of some Bragg reflections differ between the two types of samples, most noticeably the (222), (440) and (622) peaks, while b) shows these peaks in more detail. Here, one can also observe that there is a difference in lattice spacing, a, which is found to be on average 0.08% larger for the crushed crystal (see Table 5.2). Though it is not obvious from the figure, the widths of the Bragg peaks are also larger in the crushed crystal, likely indicating some amount of lattice strain. Finally, the diffuse background, shown in Fig. 5.2c), is more appreciable in the crushed crystal. Diffuse scattering, which arises from the inclusion of phonon scattering in the diffraction pattern as well as uncorrelated or extremely short range correlated atomic positions, can be viewed as the complement of larger ADPs; the "missing" intensity characterized by the ADPs goes into this diffuse background.

The higher diffuse background indicates that some amount of structural disorder is present. Meanwhile, the differences in relative intensity at certain Bragg positions, such as (222), (440) and (622), indicate an average difference in an ordered structure, which may be independent of whatever strain or positional disorder is present. The structural difference leading to these changes in relative peak intensities should be quantifiable using Rietveld refinements of well-chosen structural models. This is what we now focus on.

5.1.3.2 Relative peak intensities

Reports have been published on the structure of "stuffed" rare earth titanates, which have shown the evolution of the diffraction pattern as more

Sintered Powder							
	Stuffed Model				Stoichiometric Model		
T(K)	Yb 16*c* occupancy	a(Å)	x (O2)	R_{wp}	a(Å)	x (O2)	R_{wp}
15	0.000(1)	10.00302(3)	0.33146(3)	0.0424	10.00302(3)	0.33147(3)	0.0422
50	0.002(1)	10.00413(3)	0.33141(3)	0.0444	10.00413(3)	0.33143(3)	0.0442
100	0.001(1)	10.00724(3)	0.33133(3)	0.0409	10.00724(3)	0.33134(3)	0.0407
150	0.002(1)	10.01111(3)	0.33121(3)	0.0415	10.01111(3)	0.33122(3)	0.0414
250	0.001(1)	10.02024(3)	0.33103(3)	0.0380	10.02024(3)	0.33104(3)	0.0379

Crushed Crystal							
	Stuffed Model				Stoichiometric Model		
T(K)	Yb 16*c* occupancy	a(Å)	x (O2)	R_{wp}	a(Å)	x (O2)	R_{wp}
15	0.023(2)	10.01247(5)	0.33180(4)	0.0457	10.01247(5)	0.33193(4)	0.0460
50	0.023(2)	10.01353(5)	0.33179(4)	0.0477	10.01353(5)	0.33191(4)	0.0472
100	0.026(2)	10.01648(5)	0.33168(5)	0.0477	10.01648(5)	0.33181(4)	0.0480
150	0.023(2)	10.02020(5)	0.33156(4)	0.0450	10.02020(5)	0.33170(4)	0.0453
250	0.026(2)	10.02910(4)	0.33139(4)	0.0415	10.02910(4)	0.33154(4)	0.0419

Table 5.2: Basic refined parameters for the sintered powder and crushed crystal sample, using the stuffed model and the stoichiometric model

rare-earth is placed on the titanium site.[34] A calculation of these patterns is shown in Fig. 5.3 for $Yb_2(Ti_{2-x}Yb_x)O_{7-x/2}$. The most obvious change at low levels of stuffing is the increase of (222) relative to its immediate neighbor, (113). This is clearly observed in the raw data shown in Fig. 5.2. Other expected changes coincide with differences that are readily observed in our data as well, such as the relative increase of the (440) and (622) peaks. We are thus lead to investigate the role of stuffing in these samples.

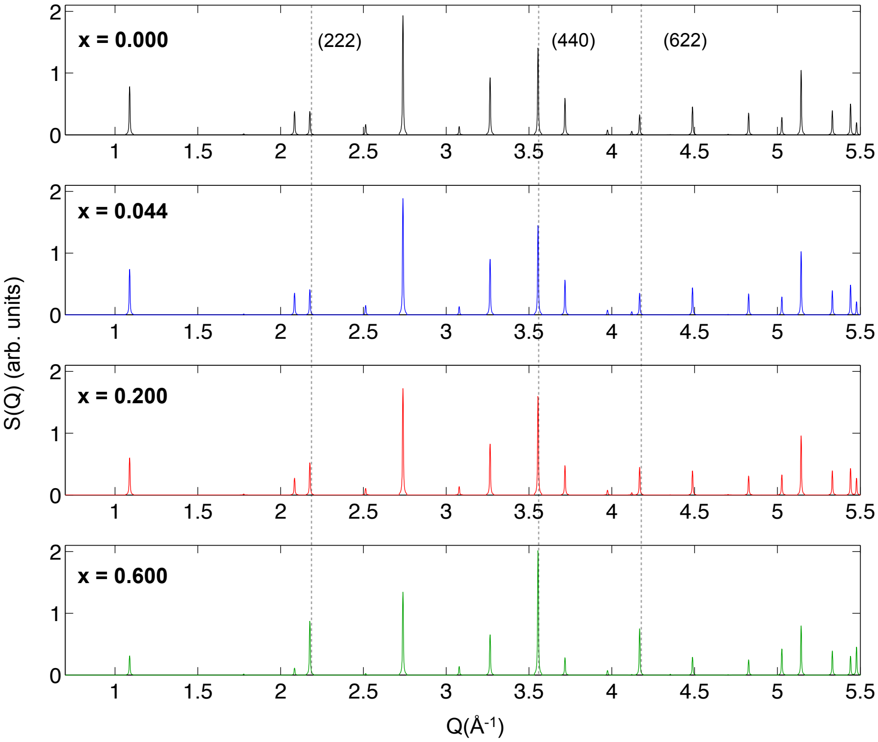

Figure 5.3: Calculated diffraction patterns for increasing levels of stuffing ($x =$ 0.000, 0.044, 0.200, and 0.600 from top to bottom, in $Yb_2(Ti_{2-x}Yb_x)O_{7-x/2}$). The most obvious change, particularly at lower stuffing levels, is the "switching" of relative intensity at (222) and its neighboring peak, (113). Other significant changes are the intensities of (622) and (440), which both increase for increased stuffing levels.

We now present a comparison between the stoichiometric and stuffed model refinements for both samples at each measured temperature. All of the refined parameters for each case are shown in Tables 5.2 and 5.3. Figure 5.4 shows the results of refinements in both models. The curve in the lower left panels for these figures represents the difference between the data and the model (residuals). In the case of the crushed crystal, larger differences are seen at the (222), (440) and (622) positions when the stoichiometric model is used (blue curve), compared to when the stuffed model is used (red curve). These peaks and the difference curves are shown in more detail on the right hand panels of Fig. 5.4, where the difference curves have been shifted up by a constant for clarity. The stuffed model refines to x=0.046, or 2.3% stuffing, for the crushed crystal. Meanwhile, the powder sample refines to x=0.000(1), and no difference is observed in the stoichiometric vs. stuffed patterns (Fig. 5.4a).

5.1.3.3 Lattice spacing

The lattice spacing of the crushed crystal sample is larger than the sintered powder (see Fig. 5.5). This is generally consistent with stuffing in pyrochlores, as shown in Figure 3 of Ref. 33. The increased cell size simply arises to accommodate the larger rare-earth ions in the titanium sites. The work by Lau *et al* in principle allows a correspondence between x and the room temperature lattice spacing of $Yb_2(Ti_{2-x}Yb_x)O_{7-x/2}$. Our maximum measured temperature was 250K, so that we must extrapolate to room temperature to compare to this study. Quadratic fits of a vs T produce a room temperature lattice spacing for the powder sample that is well-below the minimum value reported by Lau

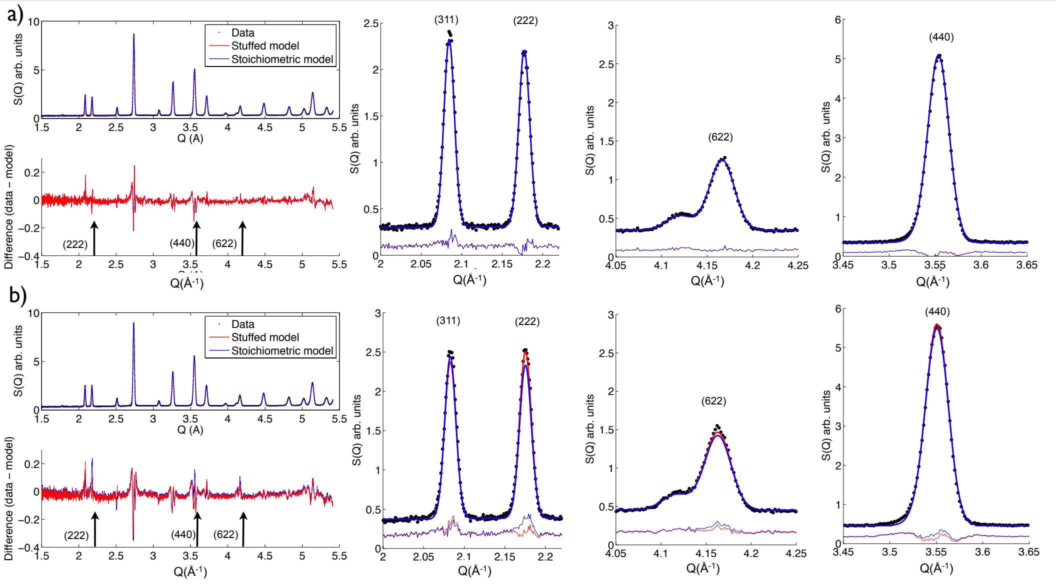

Figure 5.4: A comparison of two models used in the refinement of a) the powder sample and b) crushed crystal sample. This figure shows data at T=15K only, as data at all measured temperatures are similar. The stoichiometric model, corresponding to $Yb_2Ti_2O_7$, describes the powder sample well. For the crushed crystal sample, improvements in modelling several peak heights are obtained using a “stuffed” model corresponding to $Yb_2(Ti_{2-x}Yb_x)O_{7-x/2}$, with $x = 0.046(4)$ (2.3% substitution of Yb^{3+} for Ti^{4+}).

et al, which was 10.032 Å at x=0. We find a_{293K} = 10.025 Å for the powder, and a_{293K} = 10.034 Å for the crushed crystal. It is unclear as to why there is a discrepancy in the stoichiometric lattice spacing. However, we note that if one assumes a systematic error in the lattice spacing determination, perhaps due to instrumental effects, the difference between the lattice spacing of the crushed crystal and the sintered powder (the latter taken to be stoichiometric) would coincide with $x = 0.032$ according to Figure 3 of Ref 33. This is in fairly good agreement with the refined value of x=0.046. We also note that for a nominally stoichiometric $Yb_2Ti_2O_7$ powder sample reported on elsewhere,[50] the room temperature lattice spacing was found to be 10.024(1) Å. This is in better agreement with the values found here for the sintered powder sample.

We checked the lattice spacing of an additional single crystal of $Yb_2Ti_2O_7$, which has been characterized by low temperature specific heat. This single crystal was post-annealed in flowing oxygen for 10 days, at 1050° C. The specific heat curve is are shown in Fig. 5.6, and compared to the powder sample from Ref. 21. Consistent with other crystals of $Yb_2Ti_2O_7$, the specific heat curve of the annealed single crystal shows two relatively broad anomalies. This probably rules out both lattice strain and oxygen deficiency as the causes of the sample dependence, both of which would be expected to be relieved by the heat treatment, since it does not significantly improve the sharpness and homogeniety of the speicifc heat anomaly in the crystals. Furthermore, the lattice parameter for the annealed sample, $a = 10.0310(7)$, is consistent with that found for the CC sample studied here by neutron powder diffraction (Figure 5.5).

5.1.3.4 Atomic Displacement Parameters

Aside from capturing the relative peak intensity changes in the powder diffraction pattern for the crushed crystal, the stuffed model also suppresses the anomalously high ADPs that are refined for the Ti site in the stoichiometric model. The right hand side of Figure 5.5 shows one component of the ADPs on each site as a function of temperature, for both powder and crushed crystal samples. A general increase in ADPs is expected for a more disordered sample, and this is born out by the small increase observed in ADPs at the Yb(16d) and

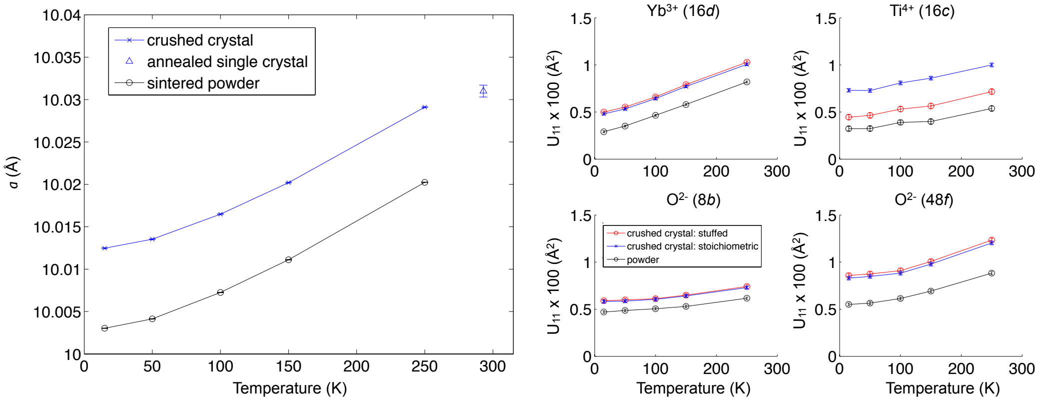

Figure 5.5: Left: Refined cubic lattice parameter, a, for the crushed crystal and sintered powder samples. The crushed crystal shows a larger lattice parameter when compared to the sintered powder, as expected for a stuffed pyrochlore. A non-pulverised single crystal sample post-annealed in oxygen gas shows a lattice parameter consistent with the crushed crystal sample. The specific heat of the annealed crystal is shown in Fig. 5.6. Right: Selected anisotropic displacement parameters (ADPs) for each lattice site, refined in both the stoichiometric and stuffed models for the crushed crystal, and the stoichiometric model for the sintered powder. Overall, the ADPs are found to be larger in the crushed crystal than in the sintered powder. The Ti^{4+} ADPs are the only ones that are affected by choice of model, to within the errorbars. They are significantly reduced in the stuffed model, making the difference in Ti^{4+} ADPs between the crushed crystal and sintered powder consistent with the other sites. The ADPs for the $48f$ O^{2-} sites remain relatively high for both models, indicating the presence of true static displacements of the oxygen ions surrounding the stuffed 16c sites.

O(8b) sites for both structural models refined for the crushed crystal. However, both the O(48f) the Ti(16c) sites see more dramatic increases in ADPs for the crushed crystal when the stoichiometric model is used. In the case of the O(48f) site, this large ADP is consistent with a stuffed pyrochlore, since static displacements of the oxygen environment surrounding the B site are expected to arise from the valency mismatch of the Yb^{3+} and Ti^{4+} ions on the 16c site. We find that the large ADP at the Ti site, however, is alleviated by using the

2.3% stuffed model. In this case, the large ADP value found for the 16c site when refined within the stoichiometric model is likely to be "unphysical", in the sense that it is compensating for problems in the assumed model. In general, the ADP effectively accounts for a "smearing" of scattering weight around a particular position, which changes the effective scattering length at that site. This can occur because of temperature increase or static distortions (both are legitimate structural effects), or because the wrong effective scattering length is used in the model. The latter appears to be the case here for the 16c site. Using the stuffed model instead, which places some ytterbium on the titanium site, brings the 16c ADPs down to approximately the same levels as the other sites. This is a strong indication that the crushed crystal is actually a lightly stuffed pyrochlore.

5.1.3.5 Susceptibility

Inverse susceptibilty as a function of temperature, collected at a constant magnetic field of 0.2T, is plotted for both SP and CC samples in Fig. 5.7. The top inset shows the full temperature range over which data was collected. The inverse susceptibility is clearly non-linear over the full temperature range, 2K to 300K; this has been noted already in the literature (Refs. 50 and 51). Population at the 10% level of the 680K crystal field excitation may be partially responsible for the non-linearity at high temperatures. However, even the lower temperature behavior (below 30K) is slightly non-linear, which is known to be a result of the magnetic anisotropy present in $Yb_2Ti_2O_7$.[51] Fitting the data from 2K to 30K to a Curie-Weiss law without taking these anisotropies

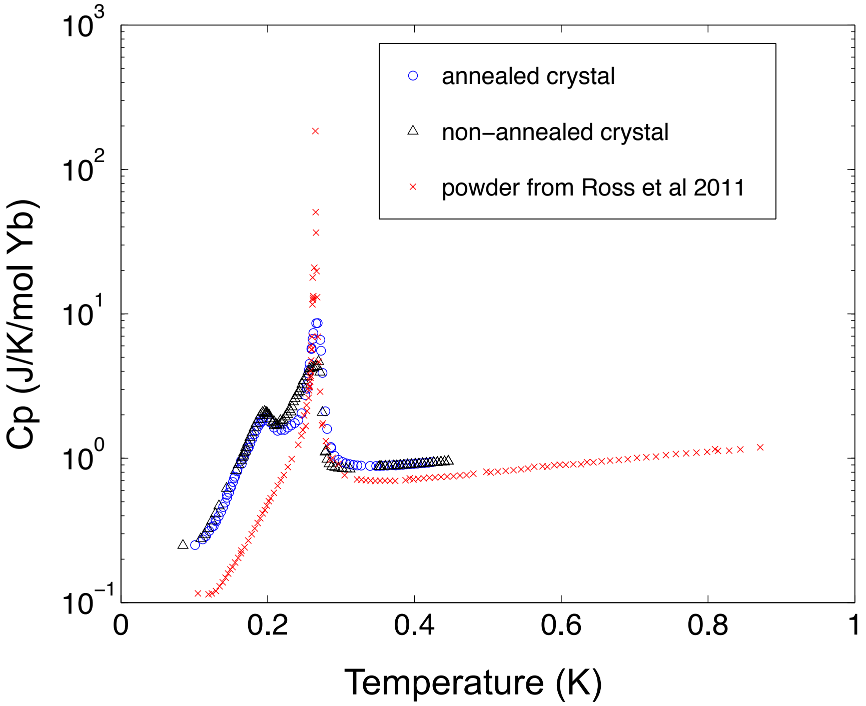

Figure 5.6: Specific heat of a single crystal annealed in oxygen gas for 10 days (blue circles), compared to a non-annealed slice of the same crystal (black triangles), as well as the powder sample from Ref. 21 (red x's).

into account, we extract an effective moment of $3.14\mu_B$ for the SP sample, and $3.43\mu_B$ for the CC, consistent with an increased number of moments in the latter sample. The Curie-Wiess temperatures were $\theta_{CW} = 152$mK for the CC sample, and $\theta_{CW} = 490$mK for the SP sample. Taken at face value, this implies that the CC sample is slightly more anti-ferromagnetic in nature than the SP sample, though the average interaction is still ferromagnetic. We comment that fitting from 2K to 10K, as was done in Refs. 52 and 51, gives $\theta_{CW} = 733$mK for the SP sample, in fair agreement with those studies (which found 800mK and 750mK, respectively). The inverse susceptibility for the CC sample fit over this smaller range gives $\theta_{CW} = 462$mK.

Sintered Powder (stoichiometric model)								
	ADPs in Å^2							
T(K)	Yb (16d) U$_{eff}$		Ti (16c) U$_{eff}$		O1 (8b) U$_{eff}$	O2 (48f) U$_{eff}$		
250	0.0082(1)		0.0057(1)		0.0062(1)	0.0078(2)		
	U11(Yb 16d)	U12(Yb 16d))	U11(Ti 16c)	U12(Ti 16c)	U11(O1 8b)	U11(O2 48f)	U22(O2 48f)	U23(O2 48f)
15	0.0029(1)	-0.00016(6)	0.0033(1)	-0.00104(2)	0.0047(1)	0.0055(2)	0.0051(1)	0.0004(1)
50	0.0035(1)	-0.00038(6)	0.0034(1)	-0.00105(2)	0.0048(1)	0.0056(2)	0.0051(1)	0.0005(1)
100	0.0046(1)	-0.00075(6)	0.0040(1)	-0.00109(2)	0.0050(1)	0.0061(2)	0.0055(1)	0.0006(1)
150	0.0058(1)	-0.00116(6)	0.0043(1)	-0.00120(2)	0.0053(1)	0.0069(2)	0.0059(1)	0.0008(1)
250	0.0082(1)	-0.00192(6)	0.0058(1)	-0.00109(2)	0.0062(1)	0.0088(2)	0.0072(1)	0.0017(1)
Crushed Crystal (stuffed model)								
	ADPs in Å^2							
T(K)	Yb (16d) U$_{eff}$		Ti (16c) U$_{eff}$		O1 (8b) U$_{eff}$	O2 (48f) U$_{eff}$		
250	0.0103(1)		0.0072(2)		0.0074(2)	0.0107(2)		
	U11(Yb 16d)	U12(Yb 16d))	U11(Ti 16c)	U12(Ti 16c)	U11(O1 8b)	U11(O2 48f)	U22(O2 48f)	U23(O2 48f)
15	0.0050(1)	-0.000990(7)	0.0045(3)	-0.0013(3)	0.0059(2)	0.0086(2)	0.0074(2)	0.0007(1)
50	0.0055(1)	-0.00116(7)	0.0046(3)	-0.0015(3)	0.0060(2)	0.0088(2)	0.0075(2)	0.0008(2)
100	0.0066(1)	-0.00155(8)	0.0053(3)	-0.0017(3)	0.0061(2)	0.0091(2)	0.0079(2)	0.0008(2)
150	0.0079(1)	-0.00201(8)	0.0056(3)	-0.0013(3)	0.0065(2)	0.0101(2)	0.0084(2)	0.0013(2)
250	0.0103(1)	-0.00269(6)	0.0072(2)	-0.0015(3)	0.0074(2)	0.0123(2)	0.0099(2)	0.0020(2)
Crushed Crystal (stoichiometric model)								
	ADPs in Å^2							
T(K)	Yb (16d) U$_{eff}$		Ti (16c) U$_{eff}$		O1 (8b) U$_{eff}$	O2 (48f) U$_{eff}$		
250	0.0101(1)		0.0100(2)		0.0073(2)	0.0104(2)		
	U11(Yb 16d)	U12(Yb 16d))	U11(Ti 16c)	U12(Ti 16c)	U11(O1 8b)	U11(O2 48f)	U22(O2 48f)	U23(O2 48f)
15	0.0048(1)	-0.00094(7)	0.0073(2)	-0.0026(3)	0.0058(2)	0.0083(2)	0.0072(2)	0.0008(2)
50	0.0053(1)	-0.00112(8)	0.0073(2)	-0.0027(3)	0.0059(2)	0.0085(2)	0.0073(2)	0.0008(2)
100	0.0064(1)	-0.00151(8)	0.0081(2)	-0.0029(3)	0.0061(2)	0.0088(2)	0.0077(2)	0.0008(2)
150	0.0077(1)	-0.00197(8)	0.0086(2)	-0.0028(3)	0.0064(2)	0.0098(2)	0.0081(2)	0.0013(2)
250	0.0100(1)	-0.00305(6)	0.0100(2)	-0.0028(3)	0.0073(2)	0.0120(2)	0.0096(2)	0.0021(2)

Table 5.3: Anisotropic Displacement Parameters (ADPs) for the sintered powder and crushed crystal. Results from both the stoichiometric and stuffed models are shown for the crushed crystal. The first row of each section shows the effective isotropic ADPs at 250K, for quick comparison between models. Other rows show the full symmetry-allowed ADPs at all measured temperatures.

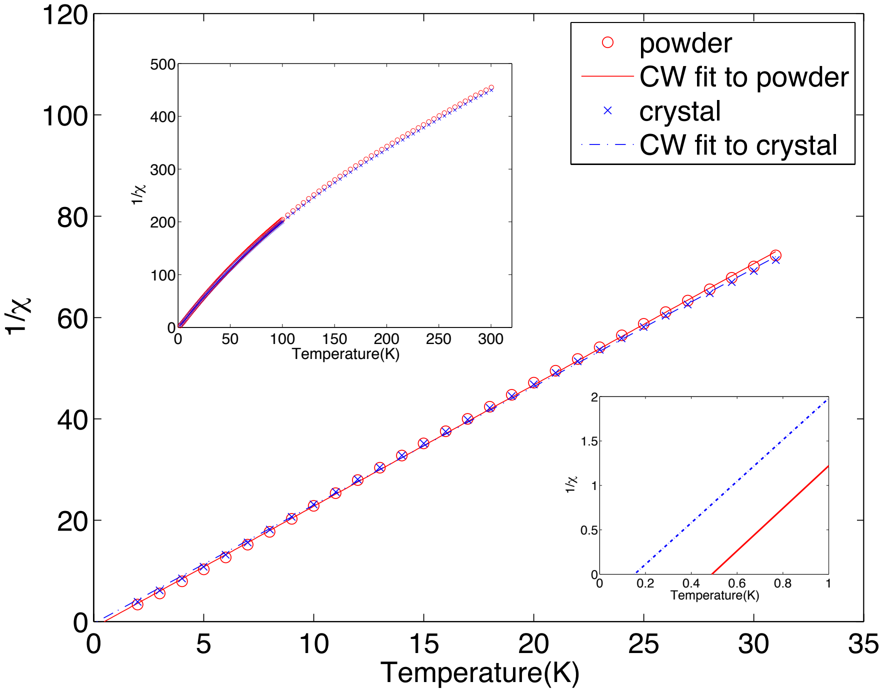

Figure 5.7: Inverse volume susceptibility (dimensionless) for both sintered powder and crushed crystal samples, with fits to a Curie-Weiss (CW) law ($\chi^{-1} = \frac{T-\theta_{CW}}{C}$). Top inset: inverse susceptibility over the full temperature range, 2K to 300K. Bottom inset: extrapolation to $1/\chi$=0 of the CW fits.

5.1.4 Discussion

Naively, the most likely scenario for the disorder in oxides grown by the OFZ method would have seemed to be oxygen non-stoichiometry, a factor that can be restricted to some extent by controlling the pressure and type of gaseous atmosphere during the growth. Oxygen non-stoichiometry has been observed in several oxides grown by the OFZ technique, including the rare-earth titanate series,[7] as well as some high T_c superconductors.[6] In the case of some high T_c superconducting materials, the transition to superconductivity is well-known to be sensitive to oxygen non-stoichiometry.[53,54] In the rare-earth titanates, oxygen deficiency is known to manifest as a change in color and transparency of the crystals.[55] Prabahkaran *et al* have shown that the magnetization of the spin ice $Dy_2Ti_2O_7$ depends on the oxygen content, which was controlled in that study by post-annealing the crystals in various gaseous atmospheres[7]. This treatment also caused a significant change in the color of the crystals in that study. In contrast, we have found evidence that simple oxygen non-stoichiometry in $Yb_2Ti_2O_7$ is *not* responsible for the variance in the magnetic properties; upon annealing a single crystal of $Yb_2Ti_2O_7$ in 1atm of flowing O_2 gas for 10 days, we find no change in color or transparency, and relatively little improvement in the specific heat anomaly, which remains bifurcated and broad (see Fig. 5.6).

Instead of a simple scenario of oxygen non-stoichiometry, the results of the refinements for the two samples of $Yb_2Ti_2O_7$ studied here indicate that the OFZ growth of $Yb_2Ti_2O_7$ is somehow deficient in titanium atoms. This is evidenced by the larger ADPs at the Ti site in the refinements of the CC structure, as well as changes to the relative Bragg peak intensities. We note that, given a titantium deficiency, the substitution of the rare earth for titanium is more likely to occur in $Yb_2Ti_2O_7$ than in the other titanates, since Yb has one of the smallest ionic radii of the series.[33] The reason for the Ti deficiency is unclear, however, since the starting materials are stoichiometric (i.e. prepared identically to the SP sample studied here), and $Yb_2Ti_2O_7$ is nominally congruently melting, so that the molten zone should have the same composition as the starting material. It is possible that there is a slight evaporation of Ti during crystal growth. Evaporation of volatile components of the molten zone can be partially controlled by performing growths in elevated gas pressure.[6] The CC studied here was grown at 4atm of O_2 gas pressure, and so this effect should be somewhat suppressed. For appreciable evaporation it is possible to observe the buildup of excess material on the quartz tube that encloses the growth. This was not visually observed in the growth of $Yb_2Ti_2O_7$, although we note that a 2.3% evaporation of Ti would amount to only 34.6mg of material on the quartz tube for a ∼10g growth. This may be difficult to see or measure by weighing the quartz tube, especially since nothing prevents the vapourized material from condensing in the upper components of the OFZ furnace away from the quartz tube.

We note that Chang *et al*[17] have had success in producing a single crystal of $Yb_2Ti_2O_7$ via the OFZ method that displays an improvement in the sharpness of the specific heat anomaly. Their growth procedure differed from ours in the following ways: they sintered their starting oxides at 1050°C (we used 1200°C), performed the growth in 1atm of air (we used 4atm of O_2), and used a much slower growth speed (1.5mm/h instead of our 6mm/h). Of these changes, one may suspect that the growth atmosphere would be the only one to affect the titanium deficiency if evaporation is indeed the cause, but it is not immediately clear why growing in air and at a lower pressure would improve this. The lower growth speed represents a much more dramatic difference in the growth process, but also does not seem to be directly related to titanium stoichiometry. We suggest that further investigations of crystals grown in different gaseous atmospheres and with different growth speeds should be carried out to find the ideal conditions for this growth.

We have found that the stuffed model more accurately accounts for the observed $S(Q)$ in the CC than does the stoichiometric model. However, there are other possibilities involving disorder on the Ti site which should also be considered, namely anti-site disorder and Ti vacancies.

- **Anti-site disorder:** Switching Yb and Ti ions would seem to be a more natural type of disorder, since it does not require the loss of titanium through the growth process. However, refining the CC within this model produces essentially an ideal structure with -0.4% anti-site mixing (the negative sign indicates an unphysical *over*-occupation of the sites with the original ions), and thus no change from the stoichiometric model in any other parameter.
- **Titanium vacancies:** This model (charge-balanced by oxygen vacancies) gives to a 6% titanium deficiency with an improved $R_{wp} = 4.09\%$, compared to the stuffed model which gives $R_{wp} = 4.19\%$. Despite this apparently better fit, this would seem to be an unlikely scenario since it requires the loss of even more titanium, which is already difficult to understand at the 2% level. Furthermore, vacancies would create *positive* chemical pressure and tend to reduce the lattice spacing. We observe the opposite effect in the CC sample.

It should also be noted that the type of structural disorder here does not account for the observed presence of some forbidden Bragg peaks in single crystal measurements of many rare-earth titanates.[56,57,58] The (002) and (006) peaks, forbidden within the Fd$\bar{3}$m space group, have been observed using time-of-flight neutron scattering. This technique is not susceptible to contamination from the higher order neutron wavelengths that otherwise could "artificially" produce a small amount of scattering at systematically absent positions. The presence of these unexpected reflections indicates either a breaking of the translational symmetry of the space group[59] or another measurement effect such as multiple-scattering. We note that the translational symmetry of the space group is not expected to be broken in the model we consider here, since we have assumed that the stuffing occurs at random titanium sites. These reflections in $Tb_2Ti_2O_7$ are seen to vanish in high magnetic fields,[60] and therefore may be related to another (magnetoelastic) distortion that has so far escaped direct detection.

At this point, it is difficult to make definitive statements about the effect of stuffing on the magnetism in $Yb_2Ti_2O_7$. Our susceptibility measurements show a tendency for the Curie-Weiss constant to decrease with stuffing, indicative of increased anti-ferromagnetic coupling. This is consistent with the observation of anti-ferromagnetic correlations in highly-stuffed spin ices. One could expect the introduction of additional nearest neighbor bonds between Yb ions to dramatically effect the ground state if geometric frustration is key to its selection. The determination of the exchange Hamiltonian for $Yb_2Ti_2O_7$ via high field inelastic neutron scattering has shown that spin-ice type exchange (ferromagnetic exchange along the local $\langle 111 \rangle$ directions on the magnetic pyrochlore sublattice) exists in $Yb_2Ti_2O_7$ and thus creates geometric frustration. This, combined with quantum fluctuations, suppresses the transition to long range order by at least 1 order of magnitude.[27] Thus, one could expect that introducing randomly located exchange bonds (with different strengths, and possibly even signs) which do not conform to the pyrochlore lattice connectivity, could significantly alter such a frustrated and delicate ground state. We therefore expect differences to exist in the magnetic specific heat, and ultimately the observed magnetic ground state.

5.1.5 Conclusions

We have shown, using neutron powder diffraction, that a single crystal of $Yb_2Ti_2O_7$ prepared by the floating zone mehod using *purely stoichiometric* starting material can be most accurately described by a 2.3% stuffed pyrochlore model. This model is an improvement over the purely stoichiometric model in three ways: it accounts for discrepancies in relative intensities of several Bragg peaks, it naturally explains the observation of an increased lattice spacing in the crystal compared to the sintered powder, and it produces a small decrease in R_{wp}, indicating a better fit in the Rietveld refinements. Other models, such as titanium vacancies with no ytterbium substitution or an anti-site disorder model, do not meet all of these criteria.

This study was motivated by the known variability of the specific heat anomaly near 200mK in single crystal samples of $Yb_2Ti_2O_7$. Our results indicate that excess moments are present in at least one single crystal prepared by the standard method. The excess moments appear to create an overall increase of anti-ferromagnetic interactions in the system, consistent with other studies of stuffed rare earth titanates. The spatially random variation of stuffed moments is likely to give rise to spin-glass like behavior in this frustrated system, which could explain the observation of broadened specific heat features in place of a sharp specific heat anomaly that is observed in the sintered powder samples. The room temperature lattice parameter could, in principle, be used to estimate the level of stuffing before performing more time-intensive experiments such as low-temeprature specific heat measurements. We hope this work will encourage more detailed characterizations of both single crystal and powder samples of $Yb_2Ti_2O_7$. In particular, it would be of interest to investigate the role of *intentional* (controlled) stuffing on the low temperature magnetic properties of the crystals.

The authors would like to acknowledge support from P. Dube at McMaster University and K. Page at LANSCE. K.A.R. and B.D.G. were partially supported by NSERC of Canada. K.A.R. acknowledges T.M. McQueen and J.E.Greedan for very helpful discussions.

5.2 * References

[1] C. Lacroix, P. Mendels, and F. Mila, *Introduction to Frustrated Magnetism* (Springer Series in Solid-State Sciences, Heidelberg, 2011).

[2] M. A. Subramanian, G. Aravamudan, and G. V. Subba Rao, Progress in Solid State Chemistry **15**, 55 (1983).

[3] J. S. Gardner, M. J. P. Gingras, and J. E. Greedan, Reviews of Modern Physics **82**, 53 (2010).

[4] H. A. Dabkowska and A. B. Dabkowski, Springer Handbook of Crystal Growth 367 (2010).

[5] G. Balakrishnan, D. M. Paul, M. R. Lees, and A. T. Boothroyd, Physica C: Superconductivity **206**, 148 (1993).

[6] S. M. Koohpayeh, D. Fort, and J. S. Abell, Progress in Crystal Growth and Characterization of Materials **54**, 121 (2008).

[7] D. Prabhakaran and A. T. Boothroyd, Journal of Crystal Growth **318**, 1053 (2011).

[8] H. Takatsu, H. Kadowaki, T. J. Sato, J. W. Lynn, Y. Tabata, T. Yamazaki, and K. Matsuhira, Journal of Physics: Condensed Matter **24**, 052201 (2012).

[9] A. Yaouanc, P. Dalmas de Réotier, Y. Chapuis, C. Marin, S. Vanishri, D. Aoki, B. Fåk, L.-P. Regnault, C. Buisson, A. Amato, C. Baines, and A. D. Hillier, Phys. Rev. B **84**, 184403 (2011).

[10] Y. Chapuis, Ph.D. thesis, Université Joseph Fourier (2009).

[11] J. S. Gardner, S. R. Dunsiger, B. D. Gaulin, M. J. P. Gingras, J. E. Greedan, R. F. Kiefl, M. D. Lumsden, W. A. MacFarlane, N. P. Raju, J. E. Sonier, I. Swainson, and Z. Tun, Phys. Rev. Lett. **82**, 1012 (1999).

[12] J. S. Gardner, A. Keren, G. Ehlers, C. Stock, E. Segal, J. M. Roper, B. Fåk, M. B. Stone, P. R. Hammar, D. H. Reich, and B. D. Gaulin, Physical Review B **68**, 180401(R) (2003).

[13] G. Luo, S. T. Hess, and L. R. Corruccini, Physics Letters A **291**, 306 (2001).

[14] E. Lhotel, C. Paulsen, P. D. de Réotier, A. Yaouanc, C. Marin, and S. Vanishri, Phys. Rev. B **86**, 020410 (2012).

[15] S. W. Han, J. S. Gardner, and C. H. Booth, Physical Review B **76**, 024416 (2003).

[16] Y. Yasui, M. Soda, S. Iikubo, M. Ito, M. Sato, N. Hamaguchi, T. Matsushita, N. Wada, T. Takeuchi, N. Aso, and K. Kakurai, Journal of the Physical Society of Japan **72**, 3014 (2003).

[17] L. Chang, S. Onoda, Y. Su, Y. Kao, K. Tsuei, Y. Yasui, K. Kakurai, and M. Lees, Nature Communications **3**, 992 (2012).

[18] J. S. Gardner, G. Ehlers, N. Rosov, R. W. Erwin, and C. Petrovic, Phys. Rev. B **70**, 180404 (2004).

[19] J. A. Hodges, P. Bonville, A. Forget, A. Yaouanc, P. Dalmas de Réotier, G. André, M. Rams, K. Królas, C. Ritter, P. C. M. Gubbens, C. T. Kaiser, P. J. C. King, and C. Baines, Phys. Rev. Lett. **88**, 077204 (2002).

[20] K. A. Ross, J. P. C. Ruff, C. P. Adams, J. S. Gardner, H. A. Dabkowska, Y. Qiu, J. R. D. Copley, and B. D. Gaulin, Phys. Rev. Lett. **103**, 227202 (2009).

[21] K. A. Ross, L. R. Yaraskavitch, M. Laver, J. S. Gardner, J. A. Quilliam, S. Meng, J. B. Kycia, D. K. Singh, T. Proffen, H. A. Dabkowska, and B. D. Gaulin, Phys. Rev. B **84**, 174442 (2011).

[22] P. Dalmas de Réotier, V. Glazkov, C. Marin, A. Yaouanc, P. C. M. Gubbens, S. Sakarya, P. Bonville, A. Amato, C. Baines, and P. J. C. King, Physica B: Condensed Matter **374**, 145 (2006).

[23] A. Yaouanc, P. Dalmas de Réotier, C. Marin, and V. Glazkov, Phys. Rev. B **84**, 172408 (2011).

[24] H. Blöte, R. Wielinga, and W. Huiskamp, Physica **43**, p.549 (1969).

[25] J. Thompson, P. McClarty, H. Rønnow, L. Regnault, A. Sorge, and M. Gingras, Physical Review Letters **106**, 187202 (2011).

[26] J. D. Thompson, P. A. McClarty, and M. J. P. Gingras, J. Phys.: Condens. Matter **23**, 164219 (2011).

[27] K. A. Ross, L. Savary, B. D. Gaulin, and L. Balents, Phys. Rev. X **1**, 021002 (2011).

[28] B. C. den Hertog and M. J. P. Gingras, Physical Review Letters **84**, 3430 (2000).

[29] N. Shannon, O. Sikora, F. Pollmann, K. Penc, and P. Fulde, Phys. Rev. Lett. **108**, 067204 (2012).

[30] R. Applegate, N. R. Hayre, R. R. P. Singh, T. Lin, A. G. R. Day, and M. J. P. Gingras, Physical Review Letters **109**, 097205 (2012).

[31] O. Benton, O. Sikora, and N. Shannon, Phys. Rev. B **86**, 075154 (2012).

[32] L. Savary and L. Balents, Phys. Rev. Lett. **108**, 037202 (2012).

[33] G. C. Lau, B. D. Muegge, T. M. McQueen, *et al.*, Journal of Solid State Chemistry **179**, 3126 (2006).

[34] G. C. Lau, T. M. McQueen, Q. Huang, H. W. Zandbergen, and R. J. Cava, Journal of Solid State Chemistry **181**, 45 (2008).

[35] P. Schiffer, A. P. Ramirez, D. A. Huse, P. L. Gammel, U. Yaron, D. J. Bishop, and A. J. Valentino, Physical review letters **74**, 2379 (1995).

[36] J. A. Quilliam, S. Meng, H. A. Craig, L. R. Corruccini, G. Balakrishnan, O. A. Petrenko, M. J. P. Gingras, and J. B. Kycia, Arxiv preprint arXiv:1006.2969 (2010).

[37] J. Gardner, G. Ehlers, P. Fouquet, B. Farago, and J. Stewart, Journal of Physics: Condensed Matter **23**, 164220 (2011).

[38] G. Ehlers, J. S. Gardner, Y. Qiu, P. Fouquet, C. R. Wiebe, L. Balicas, and H. D. Zhou, Phys. Rev. B **77**, 052404 (2008).

[39] H. Zhou, C. Wiebe, Y. Jo, L. Balicas, Y. Qiu, J. Copley, G. Ehlers, P. Fouquet, and J. Gardner, Journal of Physics: Condensed Matter **19**, 342201 (2007).

[40] K. C. Rule, G. Ehlers, J. R. Stewart, A. L. Cornelius, P. P. Deen, Y. Qiu, C. R. Wiebe, J. A. Janik, H. D. Zhou, D. Antonio, B. W. Woytko, J. P. Ruff, H. A. Dabkowska, B. D. Gaulin, and J. S. Gardner, Phys. Rev. B **76**, 212405 (2007).

[41] I. Mirebeau, A. Apetrei, J. Rodriguez-Carvajal, P. Bonville, A. Forget, D. Colson, V. Glazkov, J. P. Sanchez, O. Isnard, and E. Suard, Phys. Rev. Lett. **94**, 246402 (2005).

[42] K. Rule, G. Ehlers, J. Gardner, Y. Qiu, E. Moskvin, K. Kiefer, and S. Gerischer, Journal of Physics: Condensed Matter **21**, 486005 (2009).

[43] M. Dahlberg, M. Matthews, P. Jiramongkolchai, R. Cava, and P. Schiffer, Physical Review B **83**, 140410 (2011).

[44] J. S. Gardner, B. D. Gaulin, and D. M. Paul, Journal of Crystal Growth **191**, 740 (1998).

[45] J. A. Quilliam, C. G. A. Mugford, A. Gomez, S. W. Kycia, and J. B. Kycia, Phys. Rev. Lett. **98**, 037203 (2007).

[46] B. Toby, Journal of Applied Crystallography **34**, 210 (2001).

[47] A. Larson and R. Von Dreele, Technical report, LAUR-86-748 (unpublished).

[48] J. Greedan, D. Gout, A. Lozano-Gorrin, S. Derahkshan, T. Proffen, H. Kim, E. Božin, and S. Billinge, Phys. Rev. B **79**, 014427 (2009).

[49] B. Toby, Powder Diffraction **21**, 67 (2006).

[50] S. T. Bramwell, M. N. Field, M. J. Harris, and I. P. Parkin, Journal of Physics: Condensed Matter **12**, 483 (2000).

[51] H. B. Cao, A. Gukasov, I. Mirebeau, and P. Bonville, J. Phys.: Condens. Matter **21**, 492202 (2009).

[52] J. Hodges, P. Bonville, A. Forget, M. Rams, K. Królas, and G. Dhalenne, Journal of Physics: Condensed Matter **13**, 9301 (2001).

[53] Y. Tokura, J. B. Torrance, T. C. Huang, and A. I. Nazzal, Phys. Rev. B **38**, 7156 (1988).

[54] A. Pham, M. Hervieu, A. Maignan, C. Michel, J. Provost, and B. Raveau, Physica C: Superconductivity **194**, 243 (1992).

[55] G. Balakrishnan, O. A. Petrenko, M. R. Lees, and D. M. Paul, Journal of Physics: Condensed Matter **10**, L723 (1998).

[56] K. C. Rule, J. P. C. Ruff, B. D. Gaulin, *et al.*, Phys. Rev. Lett. **96**, 177201 (2006).

[57] J. P. Clancy, J. P. C. Ruff, S. R. Dunsiger, Y. Zhao, H. A. Dabkowska, J. S. Gardner, Y. Qiu, J. R. D. Copley, T. Jenkins, and B. D. Gaulin, Phys. Rev. B **79**, 014408 (2009).

[58] J. P. C. Ruff, J. P. Clancy, A. Bourque, M. A. White, M. Ramazanoglu, J. S. Gardner, Y. Qiu, J. R. D. Copley, M. B. Johnson, H. A. Dabkowska, and B. D. Gaulin, Phys. Rev. Lett. **101**, 147205 (2008).

[59] S. H. Curnoe, Phys. Rev. B **78**, 094418 (2008).

[60] J. P. C. Ruff, Z. Islam, J. P. Clancy, K. A. Ross, H. Nojiri, Y. H. Matsuda, H. A. Dabkowska, A. D. Dabkowski, and B. D. Gaulin, Physical Review Letters **105**, 077203 (2010).

Chapter 6

Conclusions

6.1 Contributions

Chapters 2 through 5 of this thesis comprise a substantial advancement of the understanding of $Yb_2Ti_2O_7$, a compound that was, at the start of this thesis project, a somewhat mysterious and controversial member of the rare-earth pyrochlore materials. Because of the work presented in this thesis, $Yb_2Ti_2O_7$ is now understood in terms of its fascinating "quantum spin ice" character, a concept that has paved the way for exciting predictions of emergent phenomena, as I will describe in these concluding paragraphs. The real (as opposed to idealized) $Yb_2Ti_2O_7$ material has also become better understood through a sobering, but ultimately necessary, awareness of structural imperfections that exist in the single crystals. It is now incumbent on us to understand how these imperfections can be reduced, and ultimately how they are associated with the controversy surrounding $Yb_2Ti_2O_7$'s magnetic ground state.

The contributions to the understanding of $Yb_2Ti_2O_7$ come in the form of a comprehensive survey, via neutron scattering experiments, of the dynamic and static spin correlations in its field-vs-temperature phase diagram (Chapters 2 and 3). This careful work has revealed two major features. First, the two-dimensional kagome correlations, evidenced by rods of diffuse scattering, begin to go through a dimensional crossover at a temperature above the specific heat anomaly, 400mK. The crossover is completed near 265mK, the temperature of the first specific heat anomaly in the single crystal we studied. The low temperature state consists of short-range three-dimensionally correlated spins instead of a long range ordered state. The absence of a true long range ordered state below 265mK is likely related to sample dependence of the specific heat anomaly, which we first reported, and which has now also been observed in both powder samples and single crystals of $Yb_2Ti_2O_7$ produced in different labs around the world [1, 2]. Recently Chang *et al* [2] have shown that a single crystal with a solitary and relatively sharp specific heat anomaly (though not of comparable sharpness to the best powder sample, and with a lower transition temperature), eventually shows some signs of a magnetically long range ordered state below the transition temperature after a long relaxation time.

The origin of the two-dimensional correlations observed above the transition is still unclear. These are unexpected when considering the cubic symmetry of the pyrochlore lattice. However, two recent studies have shown that using an anisotropic exchange Hamiltonian, albeit with inaccurate exchange parameters (we find the correct parameters in Chapter 4, as confirmed by Ref. [3]), the rods of diffuse scattering can be reproduced [4, 2]. Thus, the diffuse scattering itself is not beyond explanation in terms of an anisotropic exchange model. However, a study of the real-space spin correlations based on the exchange parameters found in Chapter 4 is needed in order to understand the two-dimensional nature of the high temperature state.

Another major contribution to the body of work on $Yb_2Ti_2O_7$ is the inference of a quantum critical point that separates the low temperature three-dimensionally correlated state from a field-polarized phase in applied fields greater than 0.5T. The field-polarized phase contains long-lived spin wave excitations. We measured the dynamic structure factor associated with the spin wave dispersions throughout the whole (HHL) scattering plane for several applied field values up to 5T. This set of high-field measurements has paved the way for the work described in Chapter 4.

The work presented in Chapters 4 and 5 contribute to the greater subject areas of rare-earth titanate pyrochlores, and magnetic pyrochlores in general, as well as to the specific case of $Yb_2Ti_2O_7$. The contribution to the study of rare-earth titanates is the first detailed characterization of subtle structural defects in optical floating zone growths of such compounds (Chapter 5). This growth technique is the primary method for sythesizing the whole series of the frustrated rare-earth titanates. Chapter 5 shows that the single crystals may suffer from titantium vacancies that are filled in by rare-earth cations, creating very lightly "stuffed" pyrochlores. We expect that $Yb_2Ti_2O_7$ represents a sort of upper limit on the amount of this type of disorder that could be present in nominally stoichiometric growths, since other rare-earths have larger ionic radii than Yb^{3+} and so would be more resistant to filling the smaller Ti^{4+} site. However, I note that there is already evidence in the literature of sample-dependence of the magnetic properties of $Tb_2Ti_2O_7$ [5], which may be related to a low level of stuffing such as this.

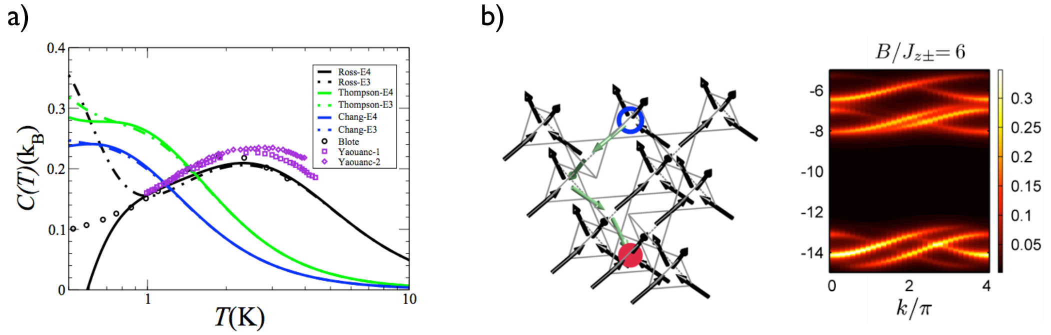

Figure 6.1: a) Figure reprinted from Ref. 3 with permission. This panel shows results of a numerical calculation of the magnetic specific heat of $Yb_2Ti_2O_7$, based on the anisotropic exchange Hamiltonian presented in Chapter 4. Data points are from two measurements, one by Blote *et al* and the other by Yaouanc *et al* [6, 1]. Solid lines correspond to the calculated specific heat for three sets of exchange parameters. The black line corresponds to the parameters determined in Chapter 4. Excellent agreement is obtained for only this set of exchange parameters. b) Figure reproduced from Ref. 7 with permission. The left panel shows the concept of a "quantum string" of flipped spins connecting two magnetic monopole excitations in the a [100] polarized spin ice state. The right hand side shows the predicted inelastic neutron scattering spectrum from such excitations.

Our contribution to the study of magnetic pyrochlores in general is the development of a strategy for accurately determining microscopic Hamiltonians for pseudo-spin 1/2 pyrochlores, in the case where spin-orbit coupling introduces singificant anisotropic exchange (Chapter 4). The strategy relies on our ability to access high-field, low-temperature states of single crystals of such compounds using time-of-flight neutron scattering. The high-field phases will invariably contain spin wave excitations, either from field-induced ordering (as we speculated in Chapter 2 for $Yb_2Ti_2O_7$) or from the field-polarization of moments (as became clear in Chapter 4). Indeed, these spin wave excitations will exist even in the absence of an ordered zero-field state. We have shown that the determination of the microscopic Hamiltonian in this manner paves the way to the resolution of long-standing puzzles. For example, our very recent application of this strategy to $Er_2Ti_2O_7$ has allowed us to conclusively show the role of quantum-order-by-disorder in its ground state selection [8], the mechanism for which had been perplexing in the absence of the full Hamiltonian.

In the case of $Yb_2Ti_2O_7$, our determination of the anisotropic exchange Hamiltonian has piqued the interest of the frustrated magnetism community and has inspired studies by other groups. One of these has confirmed our exchange parameters via comparison to thermodynamic quantities such as the specific heat (see Figure 6.1 a)) [3]. Most intriguing are the predictions for emergent behaviour in quantum spin ice systems such as $Yb_2Ti_2O_7$. Wan and Tchernyshyov [7] have predicted that the application of a magnetic field along the [100] direction of a disordered quantum spin ice material would reveal that the fundamental excitations in such systems are so-called "quantum strings". These are extended objects that can be thought of as strings which connect the topological defect excitations known as magnetic monopoles in the spin ice ground state, and they have specific signatures in the dynamic structure factor as measured by inelastic neutron scattering (Figure 6.1 b)). Intriguingly, both Wan *et al* and Applegate *et al* predict that in the case that $Yb_2Ti_2O_7$ orders in a collinear [100] configuration, as indeed has been demonstrated for one single crystal sample [9, 2], the fundamental excitations of this ground state would still be quantum strings instead of conventional magnons [7, 3]. Thus,

$Yb_2Ti_2O_7$ is expected to support unusual emergent phenomena even in the case that it orders into a seemingly conventional ground state.

6.2 Future Work

From the experimental point of view, future work should be focussed on the synthesis of crystals of $Yb_2Ti_2O_7$ with minimal structural disorder. The study presented in Chapter 5 has suggested a path forward in that regard, which is to try to minimize the effect of titanium evaporation in the optical floating zone growths. Once a very high quality crystal is obtained, time-of-flight neutron scattering should be employed to reveal the true nature of the ground state and, most importantly, its fundamental excitations.

6.3 * References

[1] A. Yaouanc, P. Dalmas de Réotier, C. Marin, and V. Glazkov, Phys. Rev. B **84**, 172408 (2011).

[2] L. J. Chang, S. Onoda, Y. Su, Y. J. Kao, K. D. Tsuei, Y. Yasui, K. Kakurai, and M. R. Lees, Arxiv preprint arXiv:1111. 5406 (2011).

[3] R. Applegate, N. Hayre, R. Singh, T. Lin, A. Day, and M. Gingras, Arxiv preprint arXiv:1203. 4569 (2012).

[4] J. D. Thompson, P. A. McClarty, H. M. Rønnow, L. P. Regnault, A. Sorge, and M. J. P. Gingras, Physical Review Letters **106**, 187202 (2011).

[5] H. Takatsu, H. Kadowaki, T. J. Sato, J. W. Lynn, Y. Tabata, T. Yamazaki, and K. Matsuhira, Journal of Physics: Condensed Matter **24**, 052201 (2012).

[6] H. Blöte, R. Wielinga, and W. Huiskamp, Physica **43**, p. 549 (1969).

[7] Y. Wan and O. Tchernyshyov, Phys. Rev. Lett. **108**, 247210 (2012).

[8] L. Savary, K. A. Ross, B. D. Gaulin, J. P. C. Ruff, and L. Balents, Arxiv preprint arXiv:1204. 1320 (2012).

[9] Y. Yasui, M. Soda, S. Iikubo, M. Ito, M. Sato, N. Hamaguchi, T. Matsushita, N. Wada, T. Takeuchi, N. Aso, and K. Kakurai, Journal of the Physical Society of Japan **72**, 3014 (2003).